

ABSTRACT

Title of dissertation: SIMULATION-BASED DESIGN,
OPTIMIZATION, AND CONTROL OF
SILICON CARBIDE AND GALLIUM
NITRIDE THIN FILM CHEMICAL VAPOR
DEPOSITION REACTOR SYSTEMS

Rinku P. Parikh, Doctor of Philosophy, 2006

Dissertation directed by: Professor Raymond A. Adomaitis
Department of Chemical and
Biomolecular Engineering

Computer models are routinely used for the design and analysis of chemical vapor deposition reactors. Accurate prediction of epitaxial thin film properties requires complete knowledge of the chemical reaction kinetics that occurs in the gas phase and at the deposition surface. The choice of reactor operating conditions and physical designs has a significant influence on the selectivity among different reaction pathways. The extent to which each pathway participates in the total deposition scheme is a function of reactor geometry, operating parameters, and the degree of precursor mixing as determined by the design of gas delivery systems.

The first part of this thesis research aims to validate gallium nitride growth kinetics. A detailed chemistry model is developed to study the interplay between the transport of reactants, adduct formation chemistry, and deposition kinetics within a MOVPE reactor showerhead system. Furthermore, the role of reactor geometry in controlling the selectivity among competing reaction pathways is explored in the

context of a planetary gallium nitride radial-flow CVD system.

The second part of this thesis research is to demonstrate the use of a novel approach to film uniformity control in planetary reactor systems based purely on the geometry of radial flow reactors with the mode of wafer rotation. In this multi-wafer reactor system, individual wafers rotate on a rotating susceptor in a planetary motion to reduce the effects of reactant depletion on deposition uniformity. The uniformity criterion developed for this system gives an unambiguous criterion for minimizing non-uniformity of any film property and gives physical insight into the reactor operating conditions that most influence uniformity. This technique is applied to a theoretical gallium nitride reactor system and a real industrial silicon carbide reactor system.

SIMULATION-BASED DESIGN, OPTIMIZATION, AND
CONTROL OF SILICON CARBIDE AND GALLIUM
NITRIDE THIN FILM CHEMICAL VAPOR
DEPOSITION REACTOR SYSTEMS

by

Rinku P. Parikh

Dissertation submitted to the Faculty of the Graduate School of the
University of Maryland, College Park in partial fulfillment
of the requirements for the degree of
Doctor of Philosophy
2006

Advisory Committee:
Professor Raymond A. Adomaitis, Chair
Professor Panagiotis Dimitrakopoulos
Dr. Deborah P. Partlow
Professor Gary W. Rubloff
Professor Evangelos Zafiriou

© Copyright by
Rinku P. Parikh
2006

DEDICATION

To my father Pankaj, mother Bindu, brother Sherin, and fiance Aruna.

ACKNOWLEDGEMENTS

This work would not be possible without the help of many people. First and foremost, I would like to thank my research advisor, Dr. Raymond A. Adomaitis. It has been a privilege to work alongside him throughout my graduate career. From the very beginning, he has been nothing but supportive, encouraging, and most of all patient. Not only is he a brilliant researcher, but an outstanding teacher. I will always remember the many times we spend in the CACSE lab deriving reactor models, running matlab simulations, and debugging code.

I would like to thank Dr. Gary W. Rubloff for his guidance, education and insight into the many aspects of my research. Also, I would like to thank Dr. Evangelhos Zafiriou and Dr. Panagiotis Dimitrakopoulos for serving on both my proposal and defense committees. Moreover, I learned transport phenomena from Dr. Dimitrakopoulos and chemical process optimization from Dr. Zafiriou - both topics that I have significantly applied to my research.

This research effort would not be possible without our collaborators at the Northrop Grumman Corporation. I would like to thank Dr. Deborah Partlow for her confidence in my research and for also serving on my defense committee. Also, I would like to thank Dr. Michael Aumer, Dr. Darren Thomson, Dr. James Oliver, Dr. Samuel Ponczak, and Brian Ponczak for their insight and the many hours they spent generating all the experimental data discussed in this thesis.

I will never forget the friends I have made at the University of Maryland. In no particular order: Rama, Vivek, Jing, Jae, Soon, Joanne, Wei, Erin, Ernie, Susan, Jin, Bryan, Sebastian, Laurent, Izzy, Bhaskar, Harin, Angela, and Chong. Thank you for all your support - year after year!

Finally, I want to thank my family (Pankaj, Bindu, Sherin, and Aruna), without whom I would not be where I am today. When all else fails, I can always count on my family for giving me support, motivation, and most of all - putting life into perspective.

Robert Frost once wrote:

*The woods are lovely dark and deep,
but I have promises to keep,
and miles to go before I sleep,
and miles to go before I sleep.*

TABLE OF CONTENTS

| | |
|---|-----------|
| List of Tables | vii |
| List of Figures | viii |
| 1 INTRODUCTION | 1 |
| 1.1 Metalorganic Vapor Phase Epitaxy | 1 |
| 1.2 Reactor Designs Issues | 3 |
| 1.3 Research Motivations and Objectives | 6 |
| 2 PHYSICALLY-BASED MODELING | 11 |
| 2.1 Governing Equations | 11 |
| 2.2 Computational Example: Simple 2D Isothermal Fluid Flow Problem | 13 |
| 3 CHEMICAL REACTION PATHWAYS | 21 |
| 3.1 Overview | 21 |
| 3.2 Gallium Nitride: Gas Phase Pathways | 23 |
| 3.2.1 Ammonia Pyrolysis Pathway | 23 |
| 3.2.2 Trimethylgallium Decomposition Pathway | 25 |
| 3.2.3 Adduct Formation and Oligomerization Pathway | 26 |
| 3.3 Surface Phase Pathways | 32 |
| 4 GaN MOVPE REACTOR SHOWERHEAD SYSTEM | 40 |
| 4.1 Precursor Delivery Showerhead as a Novel Chemical Reactor | 40 |
| 4.2 Heat Transfer and Species Transport Model | 41 |
| 4.2.1 Radial Flow Momentum and Mass Balances | 42 |
| 4.2.2 Flow Through the Showerhead Holes | 45 |
| 4.2.3 Continuity Equations | 46 |
| 4.2.4 Showerhead Temperature Model | 47 |
| 4.3 Kinetic Model | 49 |
| 4.4 Experimental and Model Validation | 52 |
| 4.4.1 Experimental Procedure | 52 |
| 4.4.2 Qualitative Comparison | 53 |
| 4.4.3 Quantitative Comparison | 55 |
| 4.4.4 Discussion of Results | 56 |
| 5 A NEW CRITERION FOR UNIFORMITY CONTROL | 71 |
| 5.1 Uniformity Modes | 71 |
| 5.1.1 Uniformity Producing Profiles in $span\{\hat{p}\}$ | 73 |
| 5.1.2 Defining the Nearest Uniformity Producing Profile (NUPP) . . | 75 |

| | | |
|-------|---|------------|
| 6 | APPLICATION OF "NUPP" FOR FILM UNIFORMITY OPTIMIZATION IN A PLANETARY GaN CVD REACTOR SYSTEM | 80 |
| 6.1 | Planetary GaN CVD Reactor Model Development | 80 |
| 6.2 | Uniformity Optimization | 88 |
| 7 | IMPLEMENTATION OF "NUPP" FOR FILM UNIFORMITY CONTROL IN A PLANETARY SiC CVD REACTOR SYSTEM | 106 |
| 7.1 | Planetary SiC CVD Reactor Model Development | 106 |
| 7.2 | Run-to-run Film Uniformity Control | 111 |
| 7.2.1 | An industrial application | 112 |
| 8 | CONCLUSIONS | 126 |
| 8.1 | Validating Gallium Nitride Growth Chemistry | 126 |
| 8.2 | Application of Novel Geometrically Based Uniformity Criterion | 127 |
| 9 | FUTURE WORK | 129 |
| 9.1 | Gallium Nitride Research | 129 |
| 9.2 | Silicon Carbide Research | 130 |
| | Bibliography | 132 |

LIST OF TABLES

| | | |
|-----|---|-----|
| 3.1 | Representative gas-phase reaction scheme for thermal decomposition of TMG, methane generation, and ethane generation. Activation energies are in (kcal/mol) and pre-exponentials are in $(cm^3/mol)^{\alpha-1}sec^{-1}$, where α is the order of reaction. Rate constants are given by $k = k_0T^nexp(-Ea/RT)$ | 35 |
| 3.2 | Representative gas-phase reaction scheme for adduct formation and oligomerization starting from TMG and NH_3 . Activation energies are in (kcal/mol) and pre-exponentials are in $(cm^3/mol)^{\alpha-1}sec^{-1}$, where α is the order of reaction. Rate constants are given by $k = k_0T^nexp(-Ea/RT)$ | 36 |
| 3.3 | Representative surface-phase reaction scheme for gallium nitride growth. S represents a free surface site. $s = 1$ corresponds to a sticking probability of unity. | 37 |
| 4.1 | Representative gas-phase reaction scheme of gallium nitride growth from trimethylgallium and ammonia included in the model for the single wafer MOVPE reactor showerhead system. Activation energies are in (kcal/mol) and pre-exponentials are in $(cm^3/mol)^{\alpha-1}sec^{-1}$, where α is the order of reaction. Rate constants are given by $k = k_0T^nexp(-Ea/RT)$ | 59 |
| 4.2 | Representative surface-phase reaction scheme for gallium nitride growth included in the model for the single wafer MOVPE reactor showerhead system. S represents a free surface site. | 60 |
| 7.1 | Representative gas-phase reaction scheme for decomposition of SiH_4 and C_3H_8 . Rate coefficients are in the form $k = aT^bexp(-c/T)$ | 115 |
| 7.2 | Sticking probabilities of the reacting species included in the silicon carbide surface model. | 116 |
| 7.3 | Uniformity criterion for run-to-run control in SiC reactor. | 117 |

LIST OF FIGURES

| | | |
|-----|---|----|
| 1.1 | Basic steps involved in a chemical vapor deposition process. | 9 |
| 1.2 | Examples of reactor designs that make use of wafer rotation: cross-flow reactor (top); cylindrical reactor (middle); planetary reactor (bottom). | 10 |
| 2.1 | Iterative simulation-based structure for solving problems in our research group. Example of this methodology for the case of thickness non-uniformity. | 17 |
| 2.2 | Cylindrical reactor chamber used for 2D simulation for an isothermal fluid flow problem. | 18 |
| 2.3 | Computational grid used for 2D simulation for an isothermal fluid flow problem. | 19 |
| 2.4 | Two-dimensional simulation results for an isothermal fluid flow problem: v_z component (upper left); v_r component (upper right); velocity vector field (bottom). | 20 |
| 3.1 | Gallium nitride chemical reaction pathway consisting of upper (adduct) and lower (decomposition) routes. | 38 |
| 3.2 | Simulation results for thermal decomposition of TMG in a flow tube reactor: $P_T = 76$ Torr; $x_{TMG}^0 = 0.05$; $\tau = 1$ sec. | 39 |
| 4.1 | Single wafer MOVPE reactor showerhead system. | 61 |
| 4.2 | Showerhead deposition pattern: before growth run (top) and after growth run (bottom). | 62 |
| 4.3 | A cross-sectional view of the showerhead configuration and notation for the design parameters and simulation variables. | 63 |
| 4.4 | A cross sectional view of a showerhead annular segment, showing all relevant heat transfer terms. | 64 |
| 4.5 | Showerhead gas temperature along with top and bottom plate temperatures (upper left); gas density (upper right); gas velocity (lower left); and pressure (lower right) for nominal set of operating conditions: pressure = 200 Torr; susceptor temperature = 1308 K; total flow($\text{NH}_3 + \text{H}_2$) = 20 slm. | 65 |

| | | |
|------|--|----|
| 4.6 | Chemical species mole fraction distributions within the showerhead. | 66 |
| 4.7 | Qualitative comparison between model predictions and observed showerhead deposition patterns: $T_{sus} = 1123$ K (top); $T_{sus} = 1308$ K (middle); $T_{sus} = 1523$ K (bottom). The colors for each plot are normalized with respect to the maximum deposition rate calculated for that particular showerhead. | 67 |
| 4.8 | Qualitative comparison between model predictions and observed showerhead deposition patterns using MATLAB image processing toolbox. $T_{sus} = 1123$ K (top); $T_{sus} = 1308$ K (middle); $T_{sus} = 1523$ K (bottom) | 68 |
| 4.9 | Quantitative comparison between model predictions and showerhead deposition experiments: total Ga-containing species deposition. | 69 |
| 4.10 | Spatial distribution of adduct molecule for three susceptor temperatures. Showerhead hole rings are marked by the red circles | 70 |
| 5.1 | Quadrature grids over the deposition (larger/blue; $\Omega(x, y)$) and wafer domains (smaller/red; $\omega(r, \theta)$). | 77 |
| 5.2 | Projection of a complete set of basis function over the deposition domain onto the wafer domain ($p_{i,j}$). | 78 |
| 5.3 | First four β_n modes spanning the space of all deposition profiles that produce perfectly uniform films under rotation for Δ | 79 |
| 6.1 | A vertical cross-sectional view of gallium nitride radial-flow planetary reactor with a 2-flow gas inlet design (top); and the physical domain (bottom). | 92 |
| 6.2 | Computational grid used for 2D simulation for a gallium nitride radial-flow planetary reactor. | 93 |
| 6.3 | 2-dimensional simulation results for gas temperature and velocity. | 94 |
| 6.4 | 2-dimensional simulation results for individual chemical species. | 95 |
| 6.5 | Simulation results for gas temperature distribution inside radial-flow planetary reactor: $T_S = 1373$ K; $T_0 = 300$ K. Location of wafer: $0.06m \leq R \leq 0.14m$ | 96 |
| 6.6 | Simulation results for individual chemical species (normalized): $T_S = 1373$ K; $x_{TMG}^0 = 1.0$; Location of wafer: $0.06m \leq R \leq 0.14m$ | 97 |

| | | |
|------|--|-----|
| 6.7 | Wafer deposition profile Δ , the resulting profile upon rotation $\bar{\delta}$ and the nearest uniformity generating profile f and its profile upon rotation \bar{f} for $T_S = 1373$ K and total flowrate = 6.5 slm. Wafers are located in non-shaded region. | 98 |
| 6.8 | Uniformity criterion C_d value as a function of susceptor temperature (total flowrate = 6.5 slm). | 99 |
| 6.9 | Results for optimal susceptor temperature of $T_S = 1312$ K (total flowrate = 6.5 slm). | 100 |
| 6.10 | Measure of nonuniformity, χ , at the $C_d = 0$ condition as a function of total flowrate. | 101 |
| 6.11 | Uniformity criterion C_d value as a function of susceptor temperature (total flowrate = 3.5 slm). | 102 |
| 6.12 | Results for optimal susceptor temperature of $T_S = 1200$ K (total flowrate = 3.5 slm). | 103 |
| 6.13 | Wafer deposition profiles for three sets of operating conditions computed by the detailed 2D transport and reaction-kinetic model. | 104 |
| 6.14 | Rotated full wafer plots for three sets of operating conditions. | 105 |
| 7.1 | A vertical cross-sectional view of silicon carbide radial-flow planetary reactor with a 2-flow gas inlet design (top); and the physical domain (bottom). | 118 |
| 7.2 | Computational grid used for 2D simulation for a silicon carbide radial-flow planetary reactor. | 119 |
| 7.3 | 2-dimensional simulation results for gas temperature and velocity. | 120 |
| 7.4 | 2-dimensional simulation results for individual chemical species. | 121 |
| 7.5 | Comparison of growth rate for simulation and experiments where the only operating parameter changing is flowrate. | 122 |
| 7.6 | Calculation of the NUPP from a stalled wafer experiment for SiC CVD: Flowrate = 35 slm; susceptor temperature = 1600 °C; Pressure = 125 mbar; SiH ₄ = 170 sccm; C ₃ H ₈ = 70 sccm. | 123 |

| | | |
|-----|--|-----|
| 7.7 | Calculation of the NUPP from stalled wafer experiments for SiC CVD: Flowrate = 40 slm (top); Flowrate = 50 slm (bottom). All other operating conditions remain constant: susceptor temperature = 1600 °C; Pressure = 125 mbar; SiH ₄ = 170 sccm; C ₃ H ₈ = 70 sccm. | 124 |
| 7.8 | Uniformity criterion (U_{CR}) as a function of flowrate from model and experiment. | 125 |

Chapter 1

INTRODUCTION

1.1 Metalorganic Vapor Phase Epitaxy

Development of advanced electronic and optoelectronic devices, such as computer chips, light emitting diodes (LEDs), communication technology, and radar systems, are achieved by growing thin films of materials above a common substrate. An established method of choice for thin film growth is chemical vapor deposition (CVD). In CVD, a gas delivery system is used to supply reactant precursors to a deposition chamber which undergo reactions and produce a desired film on a substrate or wafer. High temperatures are typically employed to promote chemical reactions which can occur in both the gas phase and on the surface.

The basic steps involved in a CVD process, depicted in Figure 1.1, are

1. Mass transport of reactants towards wafer
2. Gas phase chemical reactions to form deposition reactants
3. Adsorption of reactants on wafer surface
4. Surface phase chemical reactions on wafer
5. Desorption of volatile product species from wafer surface
6. Mass transport of product species away from wafer

Metalorganic vapor phase epitaxy (MOVPE) is a special type of CVD process where one or more of the gaseous precursors is a metalorganic compound. In the literature, alternative names for this process include metalorganic chemical vapor deposition (MOCVD), organometallic chemical vapor deposition (OMCVD), and organometallic vapor phase epitaxy (OMVPE). All the derivatives denotes the same process, where the word epitaxy is used to signify the deposition of a thin layer of single crystal material over a single crystal substrate. An example of this is silicon (Si) deposition on a silicon wafer. Metalorganic compounds are normally transported into the reactor with a carrier gas such as hydrogen (H_2). Some commonly used metalorganic compounds are those that have methyl and ethyl groups linked to group III metal atoms. These include trimethylgallium (TMG), trimethylaluminium (TMA), trimethylindium (TMI), triethylgallium (TEG), triethylaluminium (TEA), and triethylindium (TEI) [1].

Advantages of MOVPE include better film uniformity (e.g. across wafer and wafer-to-wafer), improved material quality (e.g. composition, contamination, defect density, electrical and mechanical properties), and enhanced conformality. Moreover, utilization of this growth technique has enabled fabrication of a wide variety of material systems, for example, III-V and II-VI semiconductors and most of their alloys. Two material systems successfully grown using MOVPE are gallium nitride (GaN) and silicon carbide (SiC).

Gallium nitride is a compound semiconductor material that has shown tremendous potential in electronic and optoelectronic devices over the past few years due to its wide-bandgap and high breakdown field properties [2]. GaN has a direct bandgap

of 3.4 eV making it suitable for manufacturing light emitting diodes (LEDs) capable of emitting light of any wavelength between blue and ultraviolet (UV) when alloyed with indium (In) and aluminum (Al). In addition, GaN-based devices are used for high-frequency and/or high-power applications including aircraft radar electronics [3].

Silicon carbide is a wide bandgap semiconducting material that has shown great potential for developing advanced electronic devices. SiC possesses superior physical properties, such as, large bandgap, high thermal conductivity, and high breakdown voltage. These properties and others have enabled fabrication of new and more efficient communication and radar systems technology [4].

1.2 Reactor Designs Issues

Metalorganic vapor phase epitaxy (MOVPE) is the principal method used to grow single-crystalline layers of GaN and SiC [5]. Currently, manufacturers of gallium nitride and silicon carbide devices use both commercial and custom-built reactor designs. The wide range of reactor designs indicates a lack of a coherent framework on how to design reactors for optimal single wafer and multiple-wafer production. As a result, significant research from both academic and industrial levels has enhanced manufacturing technology considerably within the past decade.

Furthermore, the rapid evolution of material systems and continued tightening of quality control constraints for thin-film manufacturing processes in semiconductor and other (e.g., optical coating) industries pose a number of challenges to equipment

design, giving rise to a wide range of reactor systems designed to reduce spatial nonuniformity of deposition thickness, composition, and microstructure. In some manufacturing processes, the use of substrate (wafer) rotation is integral to achieving acceptable film properties across the substrate. In CVD systems commonly used for semiconductor processing numerous reactor designs make use of wafer rotation (Figure 1.2), such as

- **cylindrical reactors**, in which gas flows from a shower head over a wafer and exhausts out the bottom, where wafer rotation is used to eliminate any residual angular non-uniformities in the reactor design;
- in **cross-flow reactor** designs, where gas flows through a tube or duct-shaped reactor chamber over a wafer and exhausts opposite the gas inlet, in which wafer rotation is used to reduce cross-flow deposition non-uniformities and depletion effects in the direction of flow; and
- in **planetary reactors**, where gas flows radially outward from a central feed point over the susceptor containing multiple wafers, each of which rotates on its individual axis. This design has the effect of eliminating reactor-induced angular non-uniformity generators through susceptor rotation, and wafer rotation is used to reduce the intrinsic (and completely unavoidable) effect of gas phase reactant decomposition and precursor depletion in the gas phase.

Despite ongoing research in this area, an unambiguous understanding of the physical and chemical mechanisms governing the deposition process does not yet

exist. The difficulties in achieving this understanding to a certain extent can be linked to the complex intrinsic chemistry of the deposition process, the knowledge of which currently is incomplete. A large number of gas phase and surface phase reactions resulting from the extreme conditions necessary for gallium nitride and silicon carbide growth have been extensively studied by many researchers. As a result, a number of chemical mechanisms describing important gas phase and surface phase reactions during GaN and SiC growth have been reported in the literature. Though most of these mechanisms present similar reaction pathways, the distinguishing factors are the individual rate parameters. In addition, some research groups assume significant gas phase reactions [6, 7, 8, 9], whereas others assume gas phase reactions play no role in film deposition kinetics [10, 11]. Despite the range of assumptions made regarding growth chemistry, most models are able to match experimental data when predicting growth rate and uniformity [5, 6, 7, 12, 13]. This, in fact, may be due to differences in chamber pressure, susceptor temperature, precursor flow rates, residence time in heated zones, and reactor geometry. Nonetheless, a consensus on a definitive kinetic model describing gallium nitride and silicon carbide growth has yet to be reached.

Moreover, numerous research groups have spent a considerable amount of time designing gas delivery systems for MOVPE reactors with the intent to minimize precursor interactions. The most common approach is to use separate injectors to reduce any premature mixing of the precursors [5, 6, 7]. Reactor systems of this type have been developed by SUNY/Sandia/Thomas Swann/Aixtron researchers to illustrate a connection between gas phase reactions and film-thickness uniformity. It

should be noted that while these designs can suppress reactions in the gas delivery system, complete mixing of the precursors must take place close to the wafer surface to achieve uniform film thickness [5]. Hence, these studies and others reinforce the critical role chemistry holds in designing efficient MOVPE reactors.

In conjunction with reactor design, numerous studies have focused on developing simulation tools aimed towards optimizing film-thickness uniformity. Fluid flow models that take into account heat, momentum, and mass transfer effects within both horizontal and vertical MOVPE reactors have been detailed in several papers. Many of these models incorporate large sets of chemical reactions and the model predictions ultimately are tied to the specific reactions chosen by the research group. Such models are routinely used to optimize the design and operating parameters to produce thin films with a spatially uniform thickness.

1.3 Research Motivations and Objectives

The use of advanced growth techniques such as MOVPE enables production of thin, high-quality epitaxial films. However, similar to other semiconductor technologies, MOVPE is controlled by a natural factor-ever increasing size of the wafers used for growth. As a result, research and development in the area of MOVPE is very expensive due to the high cost of equipment, individual growth runs, and experimental errors. In addition, fabrication of electronic and optoelectronic devices require growth of successive epitaxial layers with a tight control of epilayer characteristics including thickness, uniformity, composition, and crystal quality. In

an effort to reduce the number of experiments necessary for optimization of reactor design and growth conditions, computational modeling is routinely implemented. Reactor models can provide insight into many of the fundamental growth-related problems that can occur during the deposition process.

The first objective of this work was to apply simulation and advance modeling techniques to gain a deeper understanding for the physical and chemical mechanisms governing gallium nitride and silicon carbide epitaxial growth. Detailed physically-based reaction-transport models were developed for a variety of reactor designs and material systems. These models were used to study deposition pathways, improve reactor deposition uniformity, reduce run-to-run variability, and increase reactor efficiency.

The second major objective of this work was to demonstrate the use of a novel approach to film uniformity control in planetary reactor systems proposed by [14] based purely on the geometry of radial flow reactors with the mode of wafer rotation. In this approach, a sequence of stalled-wafer (non-rotating) deposition profiles are identified that, when rotated, produce perfectly uniform films. Then, a deposition profile, produced either by simulation or by an actual CVD process is projected onto this sequence of uniformity-producing profiles to compute the "Nearest Uniformity Producing Profile" (NUPP), which under rotation would produce a uniform film. Thus, it becomes clear that one would want to drive the current profile to the "nearest" optimal profile, NUPP, giving an unambiguous optimization criterion. Most importantly, the NUPP provides the process engineer with physical insight on how reactor operating conditions should be modified to drive the current profile

towards the NUPP to improve uniformity. This technique is extremely powerful because it can be applied to not only film thickness but any distributed film quality for either process development or in a run-to-run control system.

This work is organized in the following fashion. A short discussion of physically-based modeling using the quadrature-based weighted residual method techniques of Adomaitis [15] is presented in Chapter 2. An overview of the current literature on gas phase and surface phase gallium nitride chemistry is presented in Chapter 3. In Chapter 4, a detailed chemistry model is developed to study the interplay between the transport of reactants, adduct formation chemistry, and deposition kinetics within a GaN MOVPE reactor showerhead system. Derivation of the NUPP technique is presented in Chapter 5. In chapter 6, the NUPP approach is applied to a GaN radial-flow chemical vapor deposition system with planetary wafer rotation. In Chapter 7, the uniformity criterion is applied to an industrial SiC radial-flow deposition system to demonstrate NUPP-based run-to-run control capabilities. Finally, this work is concluded in Chapter 8 and future work is discussed.

Figure 1.1: Basic steps involved in a chemical vapor deposition process.

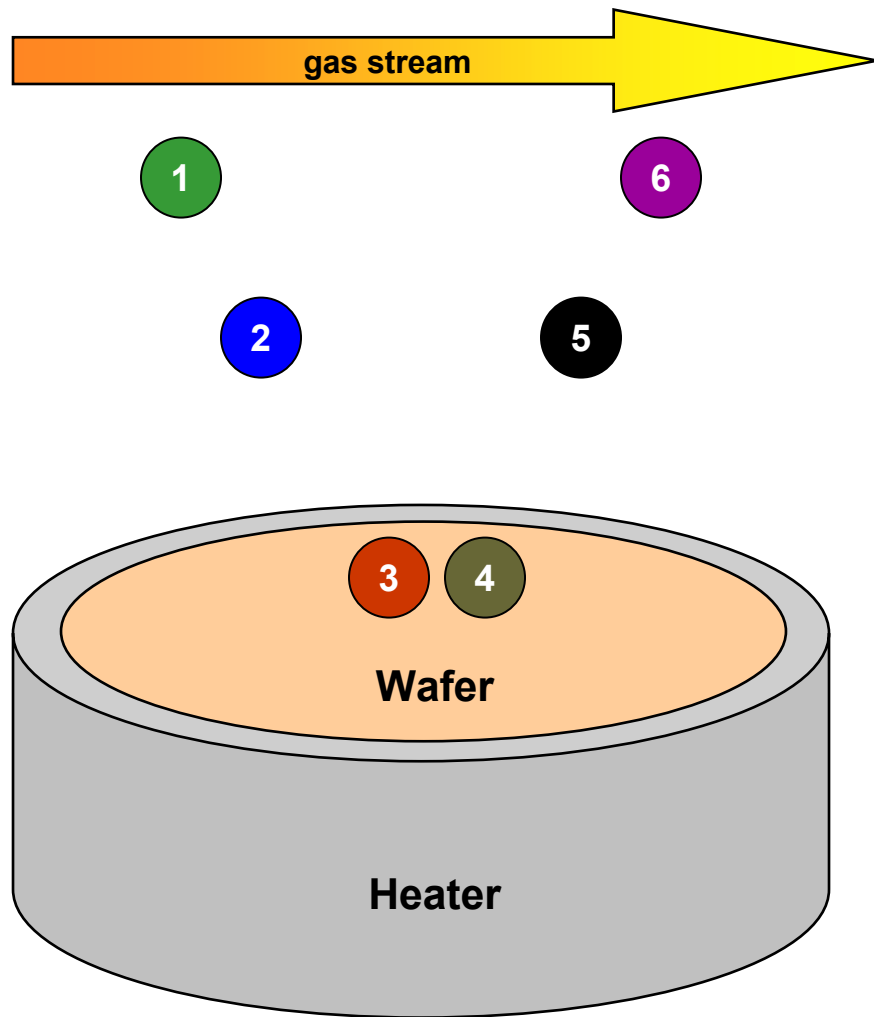
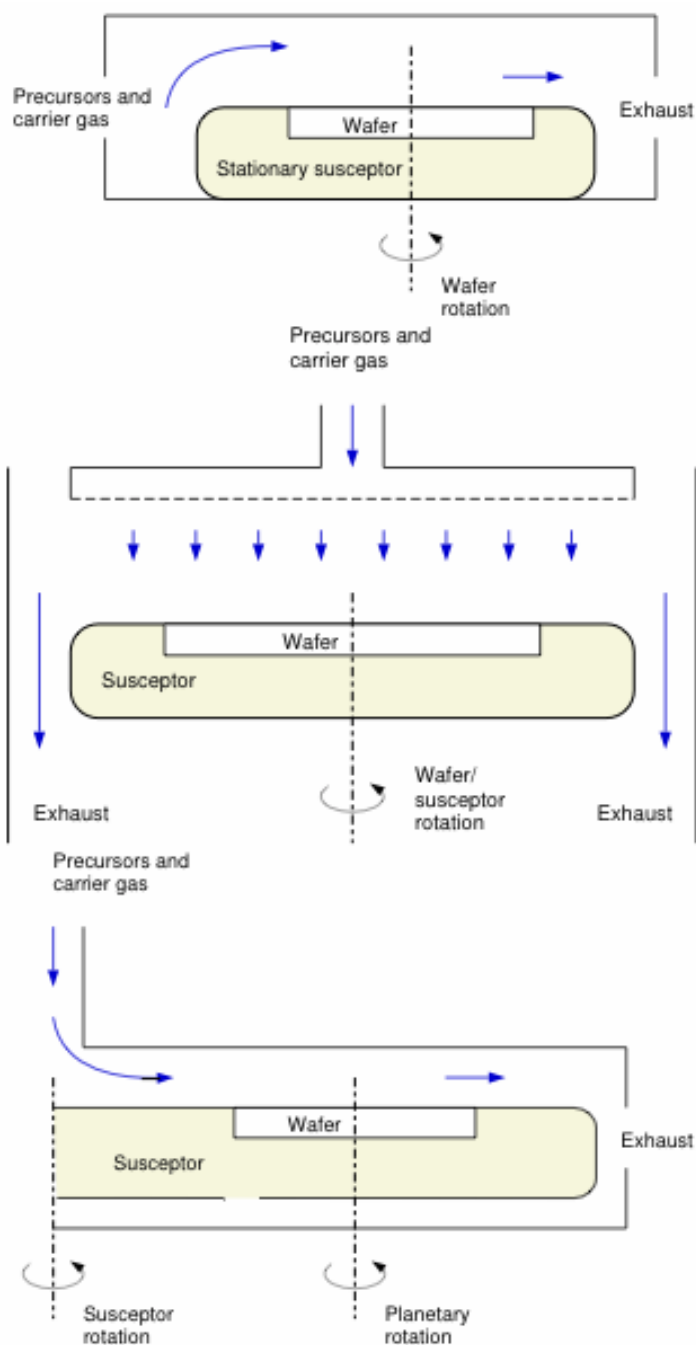


Figure 1.2: Examples of reactor designs that make use of wafer rotation: cross-flow reactor (top); cylindrical reactor (middle); planetary reactor (bottom).



Chapter 2

PHYSICALLY-BASED MODELING

2.1 Governing Equations

Our methodology for solving problems is through an iterative simulation-based structure demonstrated in Figure 2.1. In this approach, we use object-oriented simulation tools to construct physical models that help assess design and operation alternatives minimizing costly experimental runs. The mathematical models presented in this work describe interactions between fluid flow dynamics, energy transfer, and individual species transport within several different MOVPE reactor systems. The fundamental equations used to describe these phenomena consist of a set of non-linear partial differential equations and their appropriate boundary conditions. Boundary conditions define the physics that occur at the inlet, outlet, and all other solid surfaces of the system. The solution of these equations generates velocity (v), pressure (P), temperature (T), and species mole fraction (x_i) distributions within the system.

Transport and reaction-kinetic models developed in this thesis are based on fundamental equations accounting for momentum, heat, and mass-transfer within a compressible gas with temperature-dependent physical properties. Because the mixture of reactants and products in the carrier gas (H_2) is dilute, it is valid to neglect the heat of reaction along with any expansion or contraction of the mixture

due to chemical reactions. Moreover, the precursor species and all products formed from subsequent reactions between the precursors exist in low concentration relative to the carrier gas. Therefore, multicomponent diffusion need not be considered and binary diffusion coefficients of the reactants and products in the carrier gas (H_2) are utilized. Furthermore, the flow and heat transfer equations are decoupled from the mass transfer problem and were solved first to compute the gas temperature and velocity distributions. The mass transfer and kinetic problem was subsequently solved on the same grid to compute the species distribution. The continuity equation, equation of motion, equation of energy, and mass balances of each chemical species for temperature-dependent density (ρ), viscosity (μ), heat capacity (C_p), and thermal conductivity (k) are expressed as the following

Mass Continuity:

$$\nabla \cdot (\rho v) = 0 \quad (2.1)$$

Momentum Balance:

$$\rho \frac{Dv}{Dt} = -\nabla P - \nabla \cdot \tau + \rho g \quad (2.2)$$

Energy Balance:

$$\rho C_p (v \cdot \nabla T) = \nabla \cdot (k \nabla T) \quad (2.3)$$

Mass Balances:

$$\nabla \cdot (c x_i v) = \nabla \cdot [c D_i (\nabla x_i)] - R_i^G \quad (2.4)$$

The term $\left(\frac{Dv}{Dt}\right)$ in equation 2.2 represents the substantial time derivative.

2.2 Computational Example: Simple 2D Isothermal Fluid Flow Problem

Consider the problem of computing the velocity field of a gas entering a cylindrical reactor chamber (depicted in Figure 2.2). The dimensions of the physical domain extend from: $0 \leq z \leq 1.0$ and $0 \leq r \leq 2.5$. The continuity equation, equation of motion for the r-direction, and equation of motion for the z-direction of a Newtonian fluid assuming constant density and viscosity are expressed as

$$\frac{1}{r} \frac{\partial}{\partial r}(rv_r) + \frac{\partial v_z}{\partial z} = 0 \quad (2.5)$$

$$\rho(v_r \frac{\partial v_r}{\partial r} + v_z \frac{\partial v_r}{\partial z}) = -\frac{\partial p}{\partial r} + \mu[\frac{\partial}{\partial r}(\frac{1}{r} \frac{\partial}{\partial r}(rv_r)) + \frac{\partial^2 v_r}{\partial z^2}] \quad (2.6)$$

$$\rho(v_r \frac{\partial v_z}{\partial r} + v_z \frac{\partial v_z}{\partial z}) = -\frac{\partial p}{\partial z} + \mu[\frac{1}{r} \frac{\partial}{\partial r}(r \frac{\partial v_z}{\partial r}) + \frac{\partial^2 v_z}{\partial z^2}] \quad (2.7)$$

where $\rho = [kg/m^3]$ and $\mu = [kg/s/m]$. The boundary conditions for this system are defined as:

$$\text{@ } \mathbf{r} = \text{'min'}: \quad v_r = 0 \quad \frac{\partial v_z}{\partial r} = 0 \quad \frac{\partial p}{\partial r} = 0$$

$$\text{@ } \mathbf{r} = \text{'max'}: \quad \frac{1}{r} \frac{\partial}{\partial r}(rv_r) = 0 \quad v_z = 0 \quad p = 0$$

$$\text{@ } \mathbf{z} = \text{'min'}: \quad v_r = 0 \quad v_z = 0 \quad \frac{\partial p}{\partial z} = 0$$

$$\text{@ } \mathbf{z} = \text{'max'}: \quad v_r = 0 \quad v_z = f(r) = r^2 - 2.5^2 \quad \frac{\partial p}{\partial z} = 0$$

Solving this simple 2D isothermal fluid flow problem using the object oriented computational framework is discussed next. The system of non-linear partial

differential equations are discretized by collocation and subsequently solved by implementing the Newton-Raphson method. The typical mesh consisted of 30 x 30 grid points (as shown in Figure 2.3). All simulations are done using the quadrature-based weighted residual method techniques of Adomaitis [15]. The nature of this object oriented computational framework is to simplify the implementation of the quadrature-based weighted residual methods for the solution of boundary value problems (BVP) in geometrically simple domains. For example, objects of class *scalarfield* are defined to represent each of the models distributed states (e.g. gas velocity $v_z(r,z)$, pressure $p(r,z)$, etc.) along with objects of class *linearoperator* which define discretized equivalents to the differential operators in the modeling equations. Overloaded operators, such as multiplication, then allow the model developer to write discretized representations of each BVP and their boundary conditions in a way that is very similar in form to the modeling equations as represented in (2.5 - 2.7). The modeling equations are arranged into a modular simulator framework and a Newton-Raphson based equation solver is called to solve the discretized system of equations by minimizing the discretized residuals.

The physical domain (quadgrid object) is set up and the discrete differentiation operation (linearoperator) objects are defined in the **constructor file** using the methods:

```
% Define 30-point quadrature grid from  $0 \leq r \leq 2.5$ 
R = quadgrid('cyln',30,'r',[0.0 2.5]);

% Define 30-point quadrature grid from  $0 \leq r \leq 1.0$ 
Z = quadgrid('slab',30,'z',[0.0 1.0]);
```

% Define complete physical domain

S = R*Z;

% Define discretized equivalents to the differential operators

Dr = linearoperator(S,'d', 'r');

DDr = linearoperator(S,'dd','r');

Dz = linearoperator(S,'d', 'z');

DDz = linearoperator(S,'dd','z');

Dr2 = linearoperator(S,'d2', 'r');

DDr2= linearoperator(S,'dd2','r');

Initial guesses for the model distributed states are specified using the methods:

% Define model distributed states

vz = scalarfield(S,-1.0);

vr = scalarfield(S,-1.0);

p = scalarfield(S,rand(nr,nz));

The modeling equations and corresponding boundary conditions are defined

and stored in the **residual file** as follows:

% Equation of motion in z-direction and BC's

Rvz = rho*(vz*(Dz*vz) + vr*(Dr*vz)) + ...

Dz*p - visc*(DDz*vz + DDr*vz);

Rvz = setbval(Rvz,vz,'r','max');

Rvz = setbval(Rvz,Dr*vz,'r','min');

Rvz = setbval(Rvz,vz,'z','min');

Rvz = setbval(Rvz, getbval(vz,'z','max') - f, 'z','max');

% Equation of motion in r-direction and BC's

$$R_{vr} = \rho * (v_z * (D_z * v_r) + v_r * (D_r * v_r)) + \dots$$

$$D_r * p - \text{visc} * (D D_z * v_r + D D_r^2 * v_r);$$

$$R_{vr} = \text{setbval}(R_{vr}, D_r^2 * (v_r), 'r', 'max');$$

$$R_{vr} = \text{setbval}(R_{vr}, v_r, 'r', 'min');$$

$$R_{vr} = \text{setbval}(R_{vr}, v_r, 'z', 'max');$$

$$R_{vr} = \text{setbval}(R_{vr}, v_r, 'z', 'min');$$

% Continuity Equation and BC's

$$R_p = D_z * v_z + D_r^2 * (v_r);$$

$$R_p = \text{setbval}(R_p, p, 'r', 'max');$$

$$R_p = \text{setbval}(R_p, D_r * p, 'r', 'min');$$

$$R_p = \text{setbval}(R_p, D_z * p, 'z', 'max');$$

$$R_p = \text{setbval}(R_p, D_z * p, 'z', 'min');$$

Results for v_z , v_r , and the velocity vector field are shown in Figure 2.4.

Figure 2.1: Iterative simulation-based structure for solving problems in our research group. Example of this methodology for the case of thickness non-uniformity.

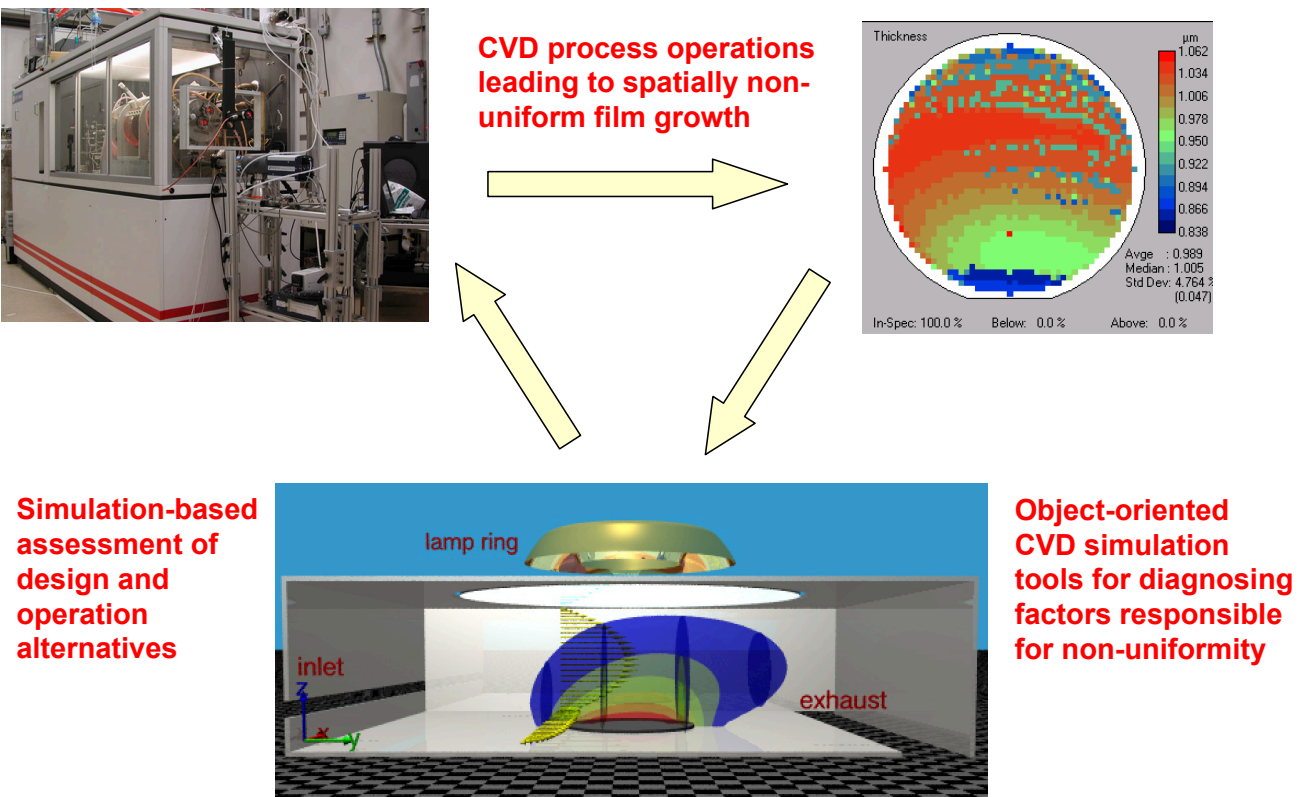


Figure 2.2: Cylindrical reactor chamber used for 2D simulation for an isothermal fluid flow problem.

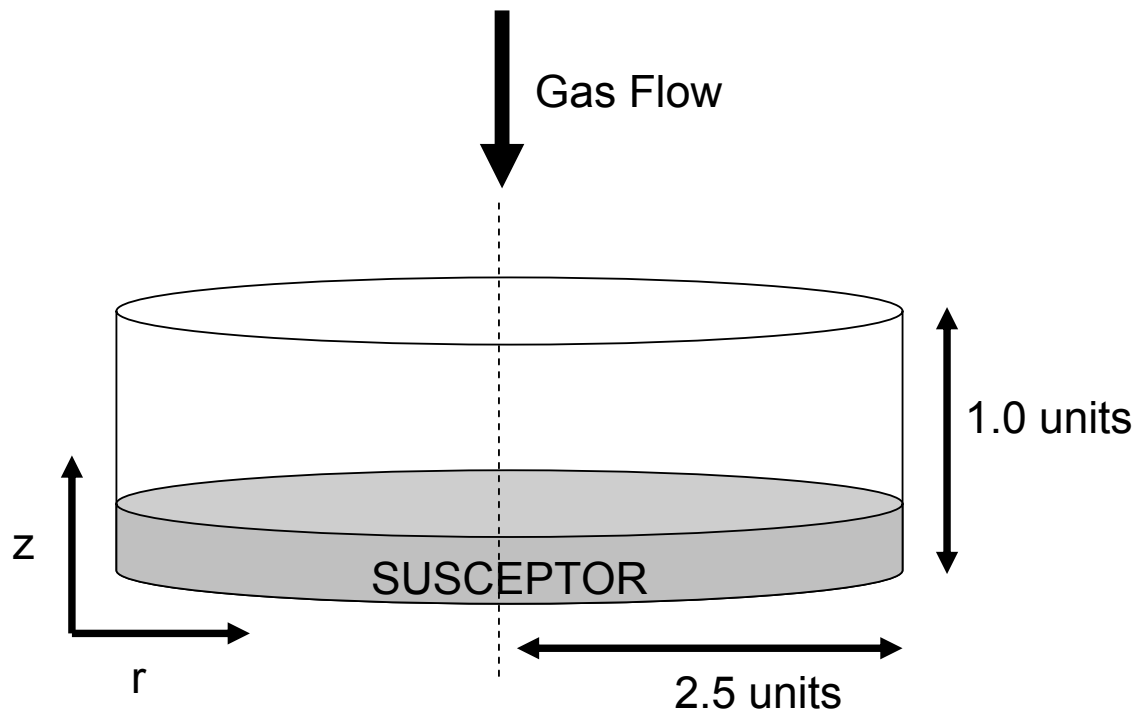


Figure 2.3: Computational grid used for 2D simulation for an isothermal fluid flow problem.

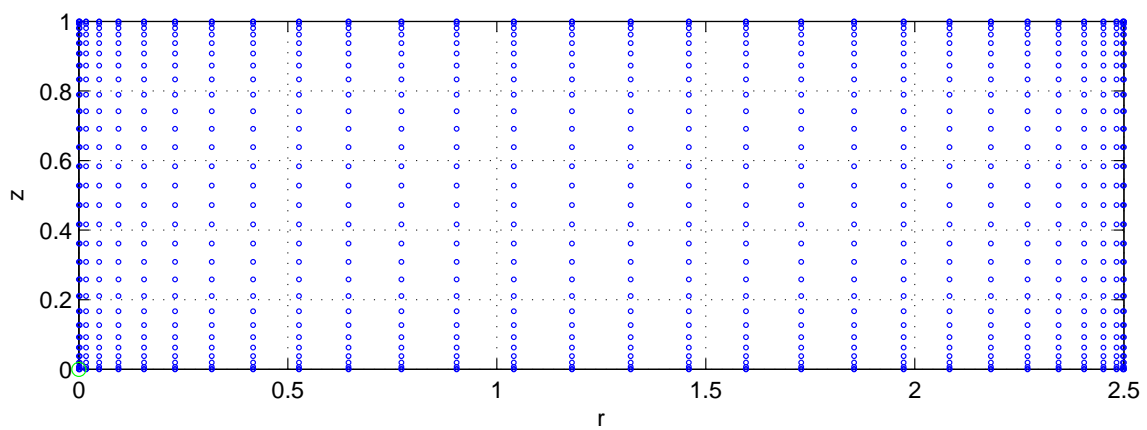
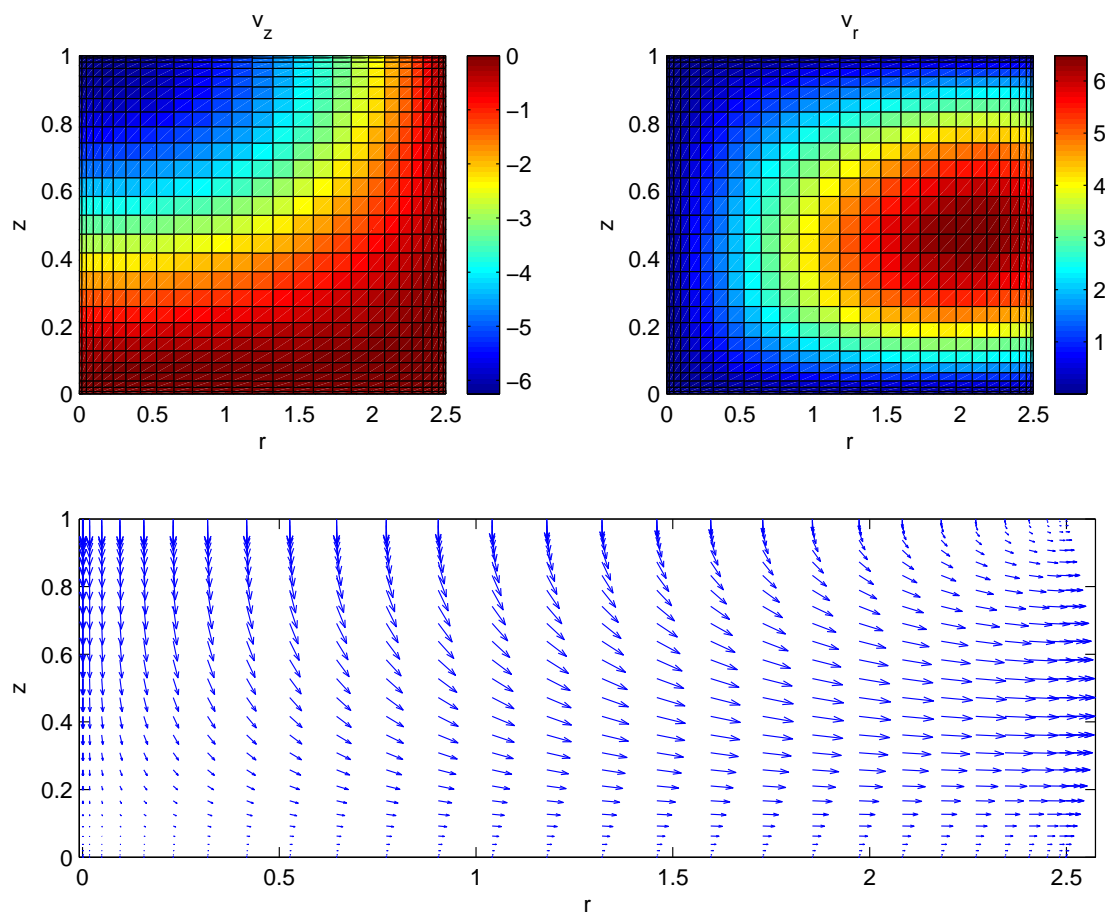


Figure 2.4: Two-dimensional simulation results for an isothermal fluid flow problem: v_z component (upper left); v_r component (upper right); velocity vector field (bottom).



Chapter 3

CHEMICAL REACTION PATHWAYS

3.1 Overview

Detailed models describing gallium nitride chemistry have been presented in the literature, and in all cases, the accuracy of the kinetic models depends on the accuracy of the rate parameters. The traditional approach to obtaining these parameters is to conduct chemical kinetic experiments which produce data on individual reaction steps. Over the years, experimental studies aimed at understanding gallium nitride chemistry have generated valuable information on a number of these elementary reaction steps. However, due to the vast number of possible gas phase and surface phase reactions involved during epitaxial growth, many of these experimental studies were unable to extract a complete set of reaction rate parameters. Recently, theoretical methods such as quantum chemistry techniques, which use first principle calculations of molecular structure and energetics combined with transition state theory (TST), have been utilized to calculate these missing rate constants [16, 17]. These theoretical methods are well documented [16, 17] and a detailed discussion on the subject is beyond the scope of this thesis. Despite the use of experimental and computational techniques, many of these rate constants remain unknown, and are often fitted to available experimental data taken from a specific reactor. This latter approach generates a model that can only be applied to a lim-

ited range of growth conditions and fails to produce a valid set of rate parameters which can be used in other reactor systems.

Hence, an overview of the major underlying chemical pathways taking place under typical growth conditions and their associated reaction rate parameters is presented in the following chapter. Section 3.2 discusses GaN gas phase pathways. Gas phase gallium nitride chemistry can be visualized as consisting of two competing routes (Figure 3.1): an a) upper route and b) lower route. The upper route is more commonly referred to as the adduct formation pathway, whereas, the lower route refers to the thermal decomposition pathway of TMG. Each pathway is responsible for producing an array of chemical species that may eventually participate in GaN deposition. The primary gas phase reaction is the spontaneous interaction between commonly used precursors, trimethylgallium ($(\text{CH}_3)_3\text{Ga}$) and ammonia (NH_3), to form stable Lewis acid-Lewis base adducts [18, 19]. Adduct formation is a ubiquitous problem during MOVPE of GaN and has been widely studied. Upon formation, these adducts may condense on cold surfaces inside the reactor system [20]. For this reason, the formation of these adducts is believed to degrade film quality, uniformity, and consume the feed stream of organometallic sources [21]. Surface phase pathways are finally discussed in Section 3.3 of this chapter.

For the case of GaN growth, adduct formation and the subsequent oligomerization is a matter widely discussed in the literature, yet open questions remain. On the other hand, decomposition chemistries of ammonia and trimethylgallium are relatively well understood, and so, offers a reasonable starting point for this discussion.

3.2 Gallium Nitride: Gas Phase Pathways

3.2.1 Ammonia Pyrolysis Pathway

NH_3 is the most widely used nitrogen precursor during MOVPE of gallium nitride. The use of NH_3 as a nitrogen source has produced high quality epitaxial films. The extent of NH_3 decomposition during epitaxial film growth is important because it will ultimately determine the amount of active species at the growth front. Davidson et al. [22] studied high-temperature NH_3 pyrolysis from a series of experiments at a temperature range of 2000-3200 K, a pressure range of 0.8-1.1 atm and a NH_3 concentration range of 0.1-1.0 %. At these conditions, substantial ammonia decomposition producing N_2 and H_2 as the major products was reported for a residence time of 1 ms. It should be noted that N_2 is far too stable and can not produce sufficient active N species for growth of gallium nitride [23]. Based on the work done by [22], a detailed reaction mechanism for NH_3 pyrolysis was proposed, comprising 9 species partaking in 21 reactions. Studies such as these can give an indication of trends for important reactive intermediates such as N, NH, and NH_2 .

In a recent study by Monnery et al. [24], pyrolysis experiments were performed under a temperature range of 1123-1473 K, pressures close to atmospheric, NH_3 concentration from 0.5-2.0 %, and residence times ranging from 50 - 800ms. It was found that the conversion of NH_3 was less than 25 % between 1123 and 1323 K. At 1423 K and residence times lower than 300ms, less than 20 % conversion of NH_3 was observed. At lower pressures, the degree of NH_3 conversion will be much lower. Other experimental studies on NH_3 pyrolysis within a quartz flow tube have been

performed by Ban [25] and Lui and Stevenson [26]. Both studies revealed minimal NH_3 decomposition under conventional MOVPE growth temperatures.

These studies indicate that high V/III ratios along with high growth temperatures are required in order to yield sufficient amounts of active nitrogen species (N , NH , NH_2) for gallium nitride growth. It is believed that high growth temperatures not only allow for NH_3 cracking, but also encourage transport of atomic N to proper lattice sites [27, 28]. Irrespective of the fact that NH_3 pyrolysis is an integral step during gallium nitride growth, it is generally not considered to be a major competing pathway due to the large amount of NH_3 that is normally used, and so, the NH_3 cracking reaction are often excluded from reactor models.

Though NH_3 is the most commonly employed nitrogen source, it has the disadvantage of being extremely corrosive and does not readily decompose at temperatures ≤ 1073 K. High growth temperatures may increase thermal stresses in the film, and intensify impurity diffusion. Hence, several alternative nitrogen sources have been considered, such as, hydrazine (N_2H_4), 1,1-dimethylhydrazine ($(\text{CH}_3)_2\text{NNH}_2$), and hydrogen azide (HN_3) [29]. Hydrazine and 1,1-dimethylhydrazine have been suggested as alternatives to NH_3 because the $\text{NH}_2\text{-NH}_2$ bond strength (71 kcal/mol) [30] in these molecules is much lower than the N-H bond strength (110 kcal/mol) in NH_3 [31]. However, both hydrazine and 1,1-dimethylhydrazine are toxic and flammable which deters utilization. Hydrogen azide decomposes at temperature ≤ 573 K into stable N_2 molecule and a metastable HN radical [29]. This radical can supply sufficient amounts of active N which can readily be incorporated into the GaN film. The drawback to using hydrogen azide is that it is highly toxic and is

potentially explosive at high pressures. For a more comprehensive review on alternative nitrogen precursors refer to work done by Neumayer et al. [29] and Beaumont et al. [23].

3.2.2 Trimethylgallium Decomposition Pathway

Analogous to NH_3 pyrolysis, the gas phase thermal decomposition of TMG ($(\text{CH}_3)_3\text{Ga}$) is also well understood. Jacko and Price [32] were the first to study TMG decomposition using a flow tube reactor with toluene as the carrier gas. From their experiments, it was determined that the decomposition pathway is characterized by three sequential, first-order reactions (Table 3.1). Reaction G1 describes the breakdown of TMG to dimethyl-gallium (DMG) with the subsequent loss of a methyl radical. In the same fashion, two more methyl radicals are formed as DMG decomposes to monomethyl-gallium (MMG) (reaction G2) which eventually gives elemental gallium (Ga) (reaction G3). These reactions produce a total of three methyl radicals per TMG molecule; the kinetic data associated with this decomposition pathway is routinely included in kinetic models describing growth of GaN by numerous research groups [5, 7, 8]. It should be noted that during the experiments done by Jacko and Price [32], the third methyl radical was not removed; however, the activation energy for reaction G3 was calculated from the strength of the last Ga-C bond to be 77.5 kcal/mol. This is valid assuming the activation energies for reactions G1 and G2 are equal to the strengths of the respective bonds. In an independent study, DenBaars et al. [33] reported similar activation energies for TMG

decomposition when H_2 was used as the carrier gas instead of toluene.

To check the validity of the TMG decomposition pathway, a kinetic model including reactions G1 through G6 (Table 3.1) was developed and simulated in this work. The results from our simulation were compared to experimental studies done by Thon and Kuech [34] in a flow tube reactor. Results from Ref. [34] were consistent with studies done by Larsen et al. [35] and DenBaars et al. [33]. Methane (CH_4) and ethane (C_2H_6) are known to form as final gas-phase products of TMG decomposition [36, 37, 38] and therefore rate expressions describing the formation of these species also have been included in the model (G4-G6). The gas-phase reactions comprising of reactions G1-G6 were simulated in an isothermal plug flow reactor (PFR) with a residence time of one second. The mole fraction of each chemical species at the end of the time span was recorded and this model was implemented over the temperature range of $473 \leq T(\text{K}) \leq 1073$. Our simulation results for TMG, CH_4 , and C_2H_6 are shown in Figure 3.2. The partial pressure profiles for these species are in good agreement with the published results [34] within a temperature range of 473-1073 K. The results reveal that thermal decomposition of TMG begins at approximately 723 K. The key reaction product is methane with ethane being formed at higher reactor temperatures.

3.2.3 Adduct Formation and Oligomerization Pathway

The immediate coordination of group III organometallic precursors with group V hydride molecules has been extensively studied. TMG is an electron-deficient

(Lewis acid) compound because the central metal atom has an empty p-orbital, and can readily accept an electron pair from a donor molecule such as NH_3 (Lewis base), to form a Lewis acid-Lewis base adduct as indicated by (1) [39].



Based on the current understanding of GaN chemistry, the above step leads to all further gas phase reactions via the upper route (Figure 3.1). The rate of (1) is assumed to be collision limited and is derived from the kinetic theory of gases [40].

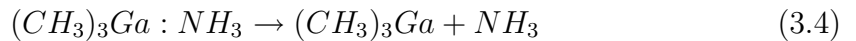
The bimolecular collision rate expression is given by

$$k = \pi\sigma_{AB}^2 \left(\frac{8k_B T}{\pi\mu} \right)^{0.5} \quad (3.2)$$

where μ is the reduced mass, T the absolute temperature in the gas phase, k_B the Boltzmann's constant and σ_{AB} is the mean collision diameter of molecule A and B given by

$$\sigma_{AB} = \frac{1}{2}(\sigma_A + \sigma_B) \quad (3.3)$$

In this case, σ_A and σ_B represent the individual collision diameters of TMG and NH_3 having values of 5.47 Å [37] and 2.92 Å [41], respectively. The activation energy for the forward reaction is 0 kcal/mol indicating adduct formation is, in fact, spontaneous. The adduct molecule can easily revert back into TMG and NH_3 as suggested by mass spectrometry and electron diffraction studies [18] and is represented by (4).



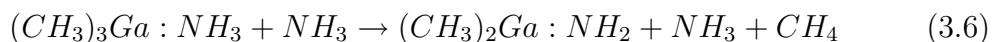
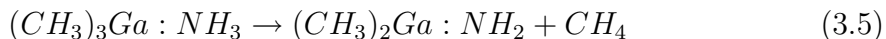
The rate of this reaction has a significant impact on nitride growth and determining the rate expression has been the focus of numerous studies. The dissociation en-

ergy of the adduct molecule is directly related to the Ga-N bond strength and has been estimated using both experimental and computation approaches. Recently, Watwe et al. [42] calculated the value of the dissociation energy to be 18 kcal/mol using quantum chemical calculations employing density functional theory (DFT) methods. In similar theoretical studies, values of 20.6 kcal/mol, 20.5 kcal/mol, and 16.8 kcal/mol have been reported by Tachibana et al. [43], Simka et al. [16] and Pelekh and Carr [44] respectively. These values are consistent with experimental work done by Leib et al. [45]. They reported the strength of the Ga-N bond to be 18.5 kcal/mol. As a result, a value of 18.5 kcal/mol is used as the activation energy for this reaction in the simulation studies to be performed later in this thesis.

Sywe et al. [46] used Fourier transform infrared (FTIR) spectrometry to study low temperature gas phase reactions between TMG and NH_3 within a gas cell. At room temperature, two experiments were conducted interchanging TMG and NH_3 as the limiting reactant. Under both sets of conditions, the coordination reaction between TMG and NH_3 occurred immediately and proceeded to completion within 0.2 seconds of mixing. Conversely, at 423 K, peaks for both TMG:NH_3 and TMG were detected and a chemical equilibrium between the adduct and the reactants in the gas phase was reached.

Further investigation of high temperature gas phase reactions between TMG and NH_3 was performed by Thon and Kuech [34] in an isothermal flow tube reactor with a residence time of 1 second by means of in situ mass spectrometry. The pressure was held constant at a value of 76 torr and data was acquired as a function of temperature through the continuous ramping of the overall reactor temperature.

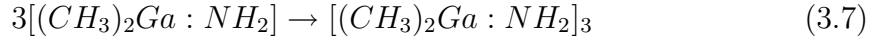
For $473 \leq T \leq 773$ C an instantaneous reaction between TMG and NH_3 was observed resulting in the release of a single methane molecule. Unfortunately, the experimental system was not able to ascertain the exact nature of the product from this reaction. At high temperatures, complete decomposition accounted for all three methane molecules. In an effort at understanding possible reactions mechanisms, the same experiment was performed using ND_3 instead of NH_3 . In this case, only CH_3D , as opposed to CH_4 , was detected by the residual gas analyzer. As a result, these studies suggest two possible pathways which lead to methane production and are shown by (5) and (6).



The reaction indicated by (5) is the intramolecular reaction describing H transfer from NH_3 to one of the methyl groups. The activation barrier for this reaction was calculated by Simka et al. [16] and Tachibana et al. [43] to be 32 kcal/mol. A value of 49 kcal/mol was determined by Zaouk et al. [21]. The second methane elimination pathway (6) corresponds to a bimolecular collision reaction involving an adduct molecule with a second NH_3 molecule. Simka et al. [16] reported an activation energy of 15 kcal/mol for this reaction making it a potential completing pathway for low temperature methane production. Other methane elimination pathways involving interactions between TMG and $\text{TMG}:\text{NH}_3$, or two $\text{TMG}:\text{NH}_3$ molecules, have been proposed in the literature [42].

What happens after methane elimination is not fully understood. Oligomer-

ization of the dimethylgallium amide, $(\text{CH}_3)_2\text{Ga}:\text{NH}_2$, to form a six member ring compound, $[(\text{CH}_3)_2\text{Ga}:\text{NH}_2]_3$, is frequently included as a major pathway in the mechanisms proposed in the literature [5, 6, 7, 8, 12, 13].



In a study done by Almond et al. [47], the trimeric species was found to exist in both the gas and solid phase at 393 K. In their experiments, the solid crystal was evaporated and traces of the ring compound were detected in the vapor. Though their results revealed evidence of a trimer species, the experiments can not verify trimer formation during conventional MOVPE growth conditions. In an earlier study, Coates [48] postulated that dimethylgallium amide should produce dimers, $[(\text{CH}_3)_2\text{Ga}:\text{NH}_2]_2$, rather than trimers. Recently, Bergmann et al. [49] used in situ mass spectrometry to study reactions between TMG and NH_3 in a flow tube reactor operating at 20 torr and a residence time of 0.2 seconds to determine important high molecular weight gallium-and-nitrogen containing compounds. Their results revealed that the concentration of the trimer is negligible particularly at high temperatures (above 1000 K) typically encountered during GaN growth. Moreover, compounds containing two gallium atoms per molecule were detected at higher temperatures, and it was concluded that these species may reach the hot wafer surface during MOVPE and participate in deposition.

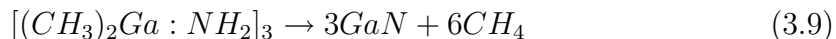
Rate parameters for the trimer formation step have been estimated by either quantum chemistry calculations or available experimental data. However, a clear consensus on this subject is missing. Therefore, similar to (2), the rate of trimer

formation is expressed as being collision limited and is governed by the probability of a three-body collision between three dimethylgallium amide molecules. The termolecular collision rate is given by

$$k = \pi \sigma_A^5 \left(\frac{8k_B T}{\pi m_A} \right)^{0.5} \quad (3.8)$$

where the collision diameter, σ_A , of $(\text{CH}_3)_2\text{Ga:NH}_2$ is calculated to be 5.39 Å based on group contribution methods [41] and m_A is the mass of $(\text{CH}_3)_2\text{Ga:NH}_2$.

The final step in the upper route is unidentified, but generally represented by the breakdown of the trimer species into low molecular weight products and large amounts of methane. Due to a limited amount of information on these low molecular weight products, their physical properties are taken to be that of GaN, and the decomposition reaction is assumed to be



The activation energy for this reaction is reported by Mihopoulos [8] to be 60.0 kcal/mol.

In summary, the upper route is characterized by four fundamental steps: (i) reversible adduct formation, (ii) methane elimination, (iii) trimer formation, and (iv) trimer dissociation. The reactions associated with these steps and their rate parameters are presented in Table 3.2. Together, Tables 3.1 and 3.2 provides a complete picture on the current understanding of gas-phase GaN chemistry.

3.3 Surface Phase Pathways

An overview of possible gas-phase reactions occurring during crystal growth of GaN has been the focus thus far. However, a complete surface reaction mechanism describing chemisorption of reactive species from the gas-phase, decomposition and recombination reactions on the surface, and epitaxial GaN film growth reactions is also absent from the literature. This is partly due to the large number of gas-phase species which can adsorb onto the surface in conjunction with limited surface science studies which are crucial for assembling reliable surface reaction networks.

Growth of high-quality GaN films requires adequate amounts of gallium and active nitrogen species near the substrate. Because high V/III ratios are typically used in MOVPE systems, it is generally assumed that the excess NH_3 and its decomposition products (N , NH , and NH_2), discussed in section 3.2.1, must also exist in large quantities relative to gallium-containing species close to the hot substrate. Hence, the growth rate will not depend on the amount of NH_3 , but instead, be dominated by the arrival rate of gallium-containing species at the growth front. For this reason, surface reaction involving NH_3 with free surface sites (S) is not critical, but is included in the surface reaction mechanism (Table 3.3) for completeness.

The surface reaction mechanism is shown in Table 3.3. The rate of all adsorption reactions is assumed to be controlled by two factors; the rate of collision of gas-phase species with the surface and the fraction of incident molecules which become adsorbed. Therefore, the adsorption rate of the i th species, R_i^S , can be

expressed as the product of the flux of species i , F_i , and its sticking probability, S .

$$R_i^S = F_i \cdot S \quad (3.10)$$

The sticking probability lies in the range $0 \leq S \leq 1$, where the two extremes correspond to no molecules being adsorbed or complete adsorption by all incident molecules, respectively. The flux, F_i , is derived from the kinetic theory of gases and governed by the Hertz-Knudsen equation [40].

$$F_i = \frac{P}{(2\pi M_i R_{gas} T)^{0.5}} \cdot x_i \quad (3.11)$$

Here F_i represents the flux of species i (mol/area/time), P the total pressure, M_i is the molecular weight of species i , R_{gas} is the ideal gas constant, T is the temperature, and x_i corresponds to the mole fraction of species i in the gas phase above the surface. Sticking probabilities of unity and activation energies of 0 kcal/mol are assumed for all surface reactions for simulations performed in this study. The use of (11) to describe surface rates implies the process is operating under mass transport limited regime. This is a reasonable assumption for high growth temperatures (1000-1300 K) typically used in MOVPE reactor designs. Reactions S1-S4 describes gallium incorporation from TMG and its subsequent decomposition products. The adduct, dimethylgallium amide, trimer, and GaN molecules deposit stoichiometric amounts of Ga and N into the film and are represented by reactions S5-S8. Finally, reaction S9 describes N incorporation from NH₃. The surface mechanism detailed in Table 3 gives no insight into whether film growth is dominated by adduct-derived species (upper route) or sub-alkyls (lower route) because a unity sticking probability is

assumed for all surface reactions. Collectively, Tables 3.1, 3.2, and 3.3 describe the overall kinetic network for GaN film growth.

Table 3.1: Representative gas-phase reaction scheme for thermal decomposition of TMG, methane generation, and ethane generation. Activation energies are in (kcal/mol) and pre-exponentials are in $(cm^3/mol)^{\alpha-1}sec^{-1}$, where α is the order of reaction. Rate constants are given by $k = k_0T^nexp(-Ea/RT)$.

| <i>Rxn. No</i> | <i>Reactions</i> | k_0 | E_a | n | <i>Ref.</i> |
|----------------|--|----------------------|-------|------|-------------|
| G1 | $(CH_3)_3Ga \rightarrow (CH_3)_2Ga + CH_3$ | 3.5×10^{15} | 59.5 | 0.0 | [32] |
| G2 | $(CH_3)_2Ga \rightarrow (CH_3)Ga + CH_3$ | 8.7×10^7 | 35.4 | 0.0 | [32] |
| G3 | $(CH_3)Ga \rightarrow Ga + CH_3$ | 1.0×10^{16} | 77.5 | 0.0 | [32] |
| G4 | $CH_3 + H_2 \rightarrow CH_4 + H$ | 2.9×10^2 | 8.6 | 3.1 | [38] |
| G5 | $CH_3 + CH_3 \rightarrow C_2H_6$ | 2.0×10^{13} | 0.0 | 0.0 | [38] |
| G6 | $CH_3 + H \rightarrow CH_4$ | 2.4×10^{22} | 0.0 | -1.0 | [38] |

Table 3.2: Representative gas-phase reaction scheme for adduct formation and oligomerization starting from TMG and NH_3 . Activation energies are in (kcal/mol) and pre-exponentials are in $(\text{cm}^3/\text{mol})^{\alpha-1}\text{sec}^{-1}$, where α is the order of reaction. Rate constants are given by $k = k_0 T^n \exp(-E_a/RT)$.

| <i>Rxn. No</i> | <i>Reactions</i> | k_0 | E_a | n | <i>Ref.</i> |
|----------------|---|----------------------|-----------|-----|-------------|
| G7 | $(\text{CH}_3)_3\text{Ga} + \text{NH}_3 \rightarrow (\text{CH}_3)_3\text{Ga} : \text{NH}_3$ | coll.(Eq.2) | 0.0 | 0.0 | [5] |
| G8 | $(\text{CH}_3)_3\text{Ga} : \text{NH}_3 \rightarrow (\text{CH}_3)_3\text{Ga} + \text{NH}_3$ | 1.0×10^{14} | 18.5 | 0.0 | [5] |
| G9 | $(\text{CH}_3)_3\text{Ga} : \text{NH}_3 \rightarrow (\text{CH}_3)_2\text{Ga} : \text{NH}_2 + \text{CH}_4$ | $10^{13}/10^{14}$ | 32.0/49.0 | 0.0 | [8, 5] |
| G10 | $(\text{CH}_3)_3\text{Ga} : \text{NH}_3 + \text{NH}_3 \rightarrow (\text{CH}_3)_2\text{Ga} : \text{NH}_2 + \text{NH}_3 + \text{CH}_4$ | 1.0×10^{12} | 15.0 | 0.0 | [16] |
| G11 | $3[(\text{CH}_3)_2\text{Ga} : \text{NH}_2] \rightarrow [(\text{CH}_3)_2\text{Ga} : \text{NH}_2]_3$ | coll.(Eq.8) | 0.0 | 0.0 | [5] |
| G12 | $[(\text{CH}_3)_2\text{Ga} : \text{NH}_2]_3 \rightarrow 3\text{GaN} + 6\text{CH}_4$ | 4.0×10^{15} | 60.0 | 0.0 | [8] |

Table 3.3: Representative surface-phase reaction scheme for gallium nitride growth.

S represents a free surface site. $s = 1$ corresponds to a sticking probability of unity.

| <i>Rxn. No</i> | <i>Reactions</i> | k_0 | E_a |
|----------------|--|-------|-------|
| S1 | $(CH_3)_3Ga + S \rightarrow Ga(s) + 3CH_3$ | s=1 | 0.0 |
| S2 | $(CH_3)_2Ga + S \rightarrow Ga(s) + 2CH_3$ | s=1 | 0.0 |
| S3 | $(CH_3)Ga + S \rightarrow Ga(s) + CH_3$ | s=1 | 0.0 |
| S4 | $Ga + S \rightarrow Ga(s)$ | s=1 | 0.0 |
| S5 | $(CH_3)_3Ga : NH_3 + 2S \rightarrow GaN(s) + 3CH_4$ | s=1 | 0.0 |
| S6 | $(CH_3)_2Ga : NH_2 + 2S \rightarrow GaN(s) + 2CH_4$ | s=1 | 0.0 |
| S7 | $[(CH_3)_2Ga : NH_2]_3 + 6S \rightarrow 3GaN(s) + 6CH_4$ | s=1 | 0.0 |
| S8 | $GaN + S \rightarrow GaN(s)$ | s=1 | 0.0 |
| S9 | $NH_3 + S \rightarrow N(s) + 1.5H_2$ | s=1 | 0.0 |

Figure 3.1: Gallium nitride chemical reaction pathway consisting of upper (adduct) and lower (decomposition) routes.

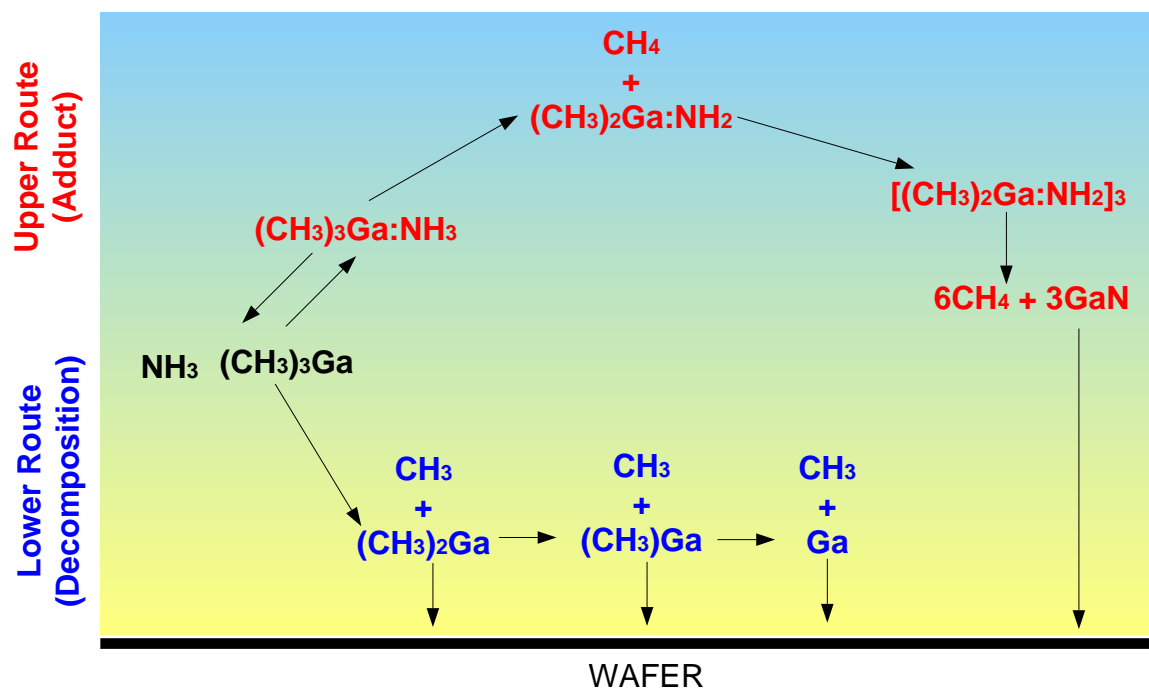
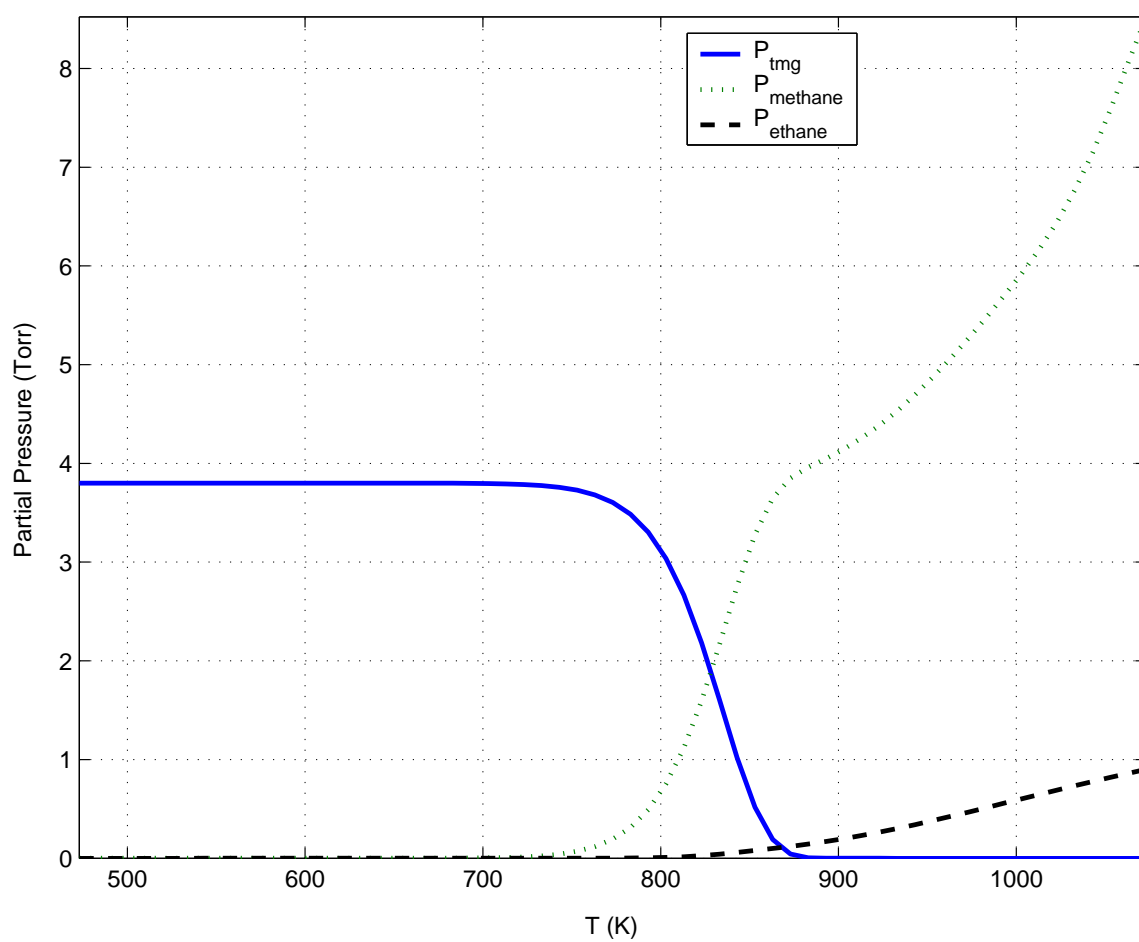


Figure 3.2: Simulation results for thermal decomposition of TMG in a flow tube reactor: $P_T = 76$ Torr; $x_{TMG}^0 = 0.05$; $\tau = 1$ sec.



Chapter 4

GaN MOVPE REACTOR SHOWERHEAD SYSTEM

4.1 Precursor Delivery Showerhead as a Novel Chemical Reactor

The extent of gas-phase reactions can be controlled through the design of gas delivery systems which range from those resulting in complete mixing to minimal or no mixing of the precursors before being fed to the reactor chamber. It should be noted that for designs that suppress reactions in the gas delivery system, complete mixing of the precursors must take place close to the wafer surface to facilitate uniform film thickness [5]. A detailed chemistry model is developed in this chapter to study the interplay between the transport of reactants, adduct formation chemistry, and deposition kinetics within a MOVPE reactor showerhead system. The reactor consists of a cooled-wall horizontal chamber with a showerhead above a single wafer resting on a heated susceptor (Figure 4.1). In this design, reactant precursors are completely mixed before being fed to the showerhead allowing us to study one extreme case for the range of gas delivery system designs discussed above. Holes are arranged in a series of concentric rings in the showerhead and are drilled through the lower quartz plate. The transparency of the showerhead provides a unique design feature which enables us to make the connection between reactor design and

chemical kinetics as concrete as possible: after each growth run, the showerhead is removed from the reactor and significant deposition is observed (Figure 4.2). More importantly, the deposition pattern is distinct in that there exists two physically different regions: a central region with little or no deposits and an annular region containing large amounts of deposits.

A detailed transport-reaction model is developed in this chapter and applied to the showerhead portion of this reactor configuration. The model attempts to capture the deposition process inside the showerhead in both a qualitative (spatial distribution of deposition pattern) and quantitative (weight measurements) fashion. The chapter is organized in the following manner - a brief overview of the heat and transport model, and a discussion of the kinetic model are presented in Sections 4.2 and 4.3, respectively. In Section 4.4, comparison between experimental results and model predictions is presented.

4.2 Heat Transfer and Species Transport Model

Expanding on some of the ideas for showerhead modeling presented in [50], a physically based model describing heat transfer and gas transport through the showerhead was developed by Hoffman and Adomaitis [51]. Their model was constructed from simplified descriptions of gas flow and heating through each component in the showerhead. The model predicts gas velocity (v), gas density (ρ), gas temperature (T_{gas}), and pressure (P) at radial positions inside the showerhead. A complete description of the showerhead heat and transport model is found in the cited work

[51]. However, because results obtained from their model are subsequently used as inputs into the kinetic model developed in this thesis, key aspects of the showerhead heat and transport model are presented in this section.

A cross-sectional view of the showerhead configuration is shown in Figure 4.3. Notation for some showerhead design parameters and simulation variables are denoted as

hole ring radii : R_1, \dots, R_M

gas radial velocity inside showerhead : u_1, \dots, u_{2M-1}

reactant gas velocity through holes : v_1, \dots, v_M

and showerhead gas pressure : P_1, \dots, P_{2M-1} .

where $m = 1, 2, \dots, M$ ($m = 1$ always refers to the showerhead center, whether or not a center hole is used).

4.2.1 Radial Flow Momentum and Mass Balances

A momentum balance for the radial component of the inter-plate gas velocity field can be written as

$$\frac{\rho}{2} \frac{\partial v_r^2}{\partial r} = -\frac{\partial P}{\partial r} + \mu \frac{\partial}{\partial r} \frac{1}{r} \frac{\partial}{\partial r} r v_r + \mu \frac{\partial^2 v_r}{\partial z^2} \quad (4.1)$$

assuming ρ and μ are constant within each segment region¹. Under the assumption of fully developed laminar gas flow in the showerhead², the radial component of gas velocity v_r can be written as

$$v_r = v_r^{max} \left[\left(\frac{\Delta Z}{2} \right)^2 - z^2 \right] \left(\frac{4}{\Delta Z^2} \right). \quad (4.2)$$

Defining u to be the mean over z , we find

$$u(r) = \frac{2}{3} v_r^{max}. \quad (4.3)$$

In between the rings of holes³, the continuity equation gives

$$\frac{d}{dr} r u = 0. \quad (4.4)$$

Therefore, if the velocity profile at the entrance to each inter-ring segment is $v_{r,m}^{in}(z)$, the velocity profile within this segment can be written as

$$v_r(r, z) = \frac{v_{r,m}^{in}(z) R_{m-1}}{r}. \quad (4.5)$$

Constant gas density in between the rings of holes is assumed in the derivation of the continuity equation for the model developed in this section. However, it should be noted that a small modification to the constant density continuity equation (4.4) is used for the kinetic model developed in Section 4.3 in order to maintain accurate species material balances. Substituting (4.3) into (4.2) and comparing the result to

¹Note that the physical properties will vary from segment region to segment region depending on the region's temperature and mean pressure.

²Calculation of the Reynolds number for the gas flow between two parallel plates for nominal operating condition shows this is a valid assumption.

³We assume $R_m - R_{m-1} \gg R_h$ in the derivation of all modeling equations.

(4.5), we see that

$$v_r = \frac{3}{2}u_{2m-3} \left[\left(\frac{\Delta_Z}{2} \right)^2 - z^2 \right] \left(\frac{4}{\Delta_Z^2} \right) \left(\frac{R_{m-1}}{r} \right). \quad (4.6)$$

Equation (4.6) now is differentiated twice with respect to z and the result is substituted into the last term of (4.1); the continuity equation (4.4) eliminates the second-to-last term of (4.1) giving

$$\frac{\rho}{2} \frac{dv_r^2}{dr} = -\frac{dP}{dr} - \frac{12\mu u_{2m-3}}{\Delta_Z^2} \left(\frac{R_{m-1}}{r} \right) + g(u_{2m-3}) \quad (4.7)$$

where the nonlinear term $g(u)$ accounts for deviations in the true contribution of frictional losses due to non-fully developed flow and other effects. Because $g(u) \rightarrow 0$ as $u \rightarrow 0$, linearizing this unknown function and incorporating it in (4.7) gives

$$\frac{\rho}{2} \frac{dv_r^2}{dr} = -\frac{dP}{dr} - \frac{12\mu k_f u_{2m-3}}{\Delta_Z^2} \left(\frac{R_{m-1}}{r} \right) \quad (4.8)$$

where the friction factor $k_f > 0$ will be determined from across-wafer uniformity measurements [51]. Averaging (4.8) over z and assuming the pressure P is a weak function of z gives

$$\frac{3\rho}{5} \frac{du^2}{dr} = -\frac{dP}{dr} - \frac{12\mu k_f u_{2m-3}}{\Delta_Z^2} \left(\frac{R_{m-1}}{r} \right). \quad (4.9)$$

Integrating (4.9) over one of the regions between consecutive hole rings gives

$$\frac{3\rho}{5} (u_{2m-2}^2 - u_{2m-3}^2) = -P_{2m-2} + P_{2m-3} - \frac{12k_f \mu u_{2m-3} R_{m-1}}{\Delta_Z^2} \ln \frac{R_m}{R_{m-1}} \quad m = 3, 4, \dots, M. \quad (4.10)$$

A momentum balance (after [52]) at each hole ring junction point gives

$$P_{2m-2} - P_{2m-1} = k_p \rho (u_{2m-1}^2 - u_{2m-2}^2) \quad m = 2, 3, \dots, M \quad (4.11)$$

where a (positive) pressure jump occurs at each hole ring due to the drop in radial velocity resulting from gas flowing out of the ring of showerhead holes. The correction factor $0 \leq k_p \leq 1$ is discussed in [52] and accounts for any radial velocity component of the flow leaving the control volume through the showerhead holes.

4.2.2 Flow Through the Showerhead Holes

Each hole in the lower showerhead plate forms a cylinder with radius R_h and length Δ_L . The coordinate system for each hole consists of the local radial position r' (i.e., $r' = 0$ at each hole centerline) and global axial direction z . A momentum balance for the reactant gas passing through a showerhead hole gives

$$\frac{\rho}{2} \frac{\partial v_z^2}{\partial z} = -\frac{\partial P}{\partial z} - \mu \frac{1}{r'} \frac{\partial}{\partial r'} \left(r' \frac{\partial v_z}{\partial r'} \right).$$

If v_m is the mean velocity of the gas passing through each showerhead hole and accounting for any deviations from fully-developed flow in the same manner as (4.7), the momentum balance equation can be reduced to the following simplified form:

$$\frac{2\rho}{3} v_m^2 + \frac{8k_s \mu v_m \Delta_L}{R_h^2} = \frac{P_{2m-2} + P_{2m-1}}{2} - P_c \quad m = 2, 3, \dots, M \quad (4.12)$$

(compare this to equation (7) of [50]). We note this equation uses the mean of the pressure difference across each hole row (4.11); the equation describing the gas velocity through the center hole (v_1) is

$$\frac{2\rho}{3} v_1^2 + \frac{8k_s \mu v_1 \Delta_L}{R_h^2} = \frac{P_1 + 2P_{ft}}{3} - P_c \quad (4.13)$$

with

$$P_{ft} = P_1 - \frac{3\rho}{5} u_{ft}^2, \quad u_{ft} = u_2 \frac{r_2}{R_{ft}}. \quad (4.14)$$

In these equations, P_{ft} , u_{ft} , and R_{ft} represent the feed tube pressure, velocity, and radius, respectively.

4.2.3 Continuity Equations

A material balance over the center-most region of the showerhead gives:

$$Q\rho_1 - 2\pi R_2\Delta_Z u_2\rho_1 = \pi N_1 R_h^2 v_1\rho_1 \quad (4.15)$$

and a material balance at each showerhead ring junction gives:

$$2R_m\Delta_z(u_{2m-2}\rho_{m-1} - u_{2m-1}\rho_m) = N_m R_h^2 v_m\rho_m \quad m = 2, 3, \dots, M. \quad (4.16)$$

Here, Q represents the total volumetric flow into the showerhead and N_m the number of holes in each ring. Finally, the continuity equation between each ring relates the radial velocity value at the downstream edge of one hole ring to the velocity at the leading edge of the next ring:

$$R_m u_{2m-2} = R_{m-1} u_{2m-3} \quad m = 3, 4, \dots, M. \quad (4.17)$$

Symmetry at $r = 0$ and no radial flow at $r = R_{sh}$ (R_{sh} corresponds to the radius of the showerhead) require

$$u_1 = 0, \quad u_{2M-1} = 0 \quad (4.18)$$

and the centerline pressure P_1 is approximated as the sum of the pressure drop required to accelerate the gas to the radial velocity u_{ft} and the pressure difference found using (4.10) evaluated over $R_{ft} \leq r \leq R_2$:

$$\frac{3\rho}{5}u_2^2 = -P_2 + P_1 - \frac{12k_f\mu u_{ft}R_{ft}}{\Delta_Z^2} \ln \frac{R_2}{R_{ft}} \quad (4.19)$$

where u_{ft} was defined in (4.14). Recall that the pressure P_1 includes the influence of the $(3\rho/5)u_{ft}^2$ term contained in its definition (4.14).

4.2.4 Showerhead Temperature Model

The temperature distribution for the top showerhead plate $T_{top}(r)$, the bottom showerhead plate $T_{bot}(r)$, and the reactant gas flowing in between them $T_{gas}(r)$ is computed from an energy balance that takes into account three modes of heat transfer: radiation, conduction, and sensible heat changes due to flow and heating of the reactants inside the showerhead (Figure 4.4). Radiative heat transfer occurs between the following reactor elements: heated susceptor (wafer) and showerhead bottom and top plates; showerhead top and the reactor liner walls; and top and bottom plates themselves. Conduction of heat occurs between the following reactor elements: showerhead and susceptor; showerhead top and liner walls; and reactant gas and showerhead top and bottom plates. Based on simulation studies of the heat transfer model, an accurate representation of the radiative heat transfer between the showerhead top plate and the susceptor as a result of reflection off the liner tube reflective gold coating (q_{rrw} in Figure 4.4) is essential in predicting accurate temperature distributions. An important parameter in this energy balance is γ , which represents the percentage of the liner surface that is covered with a gold coating. The value of γ is set between the 0 and 1, where $\gamma = 1$ corresponds to a fully coated (highly reflective) liner.

The temperature distribution of the showerhead plates and reactant gas is

approximated by a piece-wise continuous and locally constant function. The modeling equations to be solved consist of a large set of nonlinear algebraic equations: the equations describe the spatially discretized showerhead gas energy balance, the showerhead top and bottom plate energy balances, and the showerhead gas momentum balances and continuity equations.

Results for gas velocity, pressure, gas temperature, and top and bottom showerhead plate temperatures are shown in Figure 4.5 for a nominal set of operating conditions: pressure = 200 Torr; susceptor temperature = 1308 K; total flow($\text{NH}_3 + \text{H}_2$) = 20 slm. It is apparent in Figure 4.5 that the temperature of both the top and bottom showerhead plates are hot relative to the gas temperature in the central region of the showerhead. This is a result of the cool gas feed and radiative heating of the showerhead. As the gas flows outward, the gas temperature increases and reaches a level somewhere between the two plate temperatures. The result for gas velocity and internal showerhead pressure are also shown in Figure 4.5. A decrease in gas velocity is observed due to the cylindrical geometry of the inter-plate showerhead space. The circles denote hole ring locations that give rise to jumps in velocity and pressure observed in the figure. Note that the jump in velocity is a function of the change in gas temperature and flow out the hole ring, and so maybe positive or negative. The following section combines these results with a detailed kinetic model to provide spatial chemical species distributions within the showerhead.

4.3 Kinetic Model

A detailed one-dimensional showerhead reaction model is developed in this section. Rate parameters for all gas phase reactions included in the model are given in Table 4.1. The rate of G4 is assumed to be collision limited and is derived from the kinetic theory of gases [40]. The bimolecular collision rate expression is given by

$$k = \pi\sigma_{AB}^2 \left(\frac{8k_B T}{\pi\mu} \right)^{0.5} \quad (4.20)$$

where μ is the reduced mass, T the absolute temperature in the gas phase, k_B the Boltzmann's constant and σ_{AB} is the mean collision diameter of molecule A and B given by

$$\sigma_{AB} = \frac{1}{2}(\sigma_A + \sigma_B) \quad (4.21)$$

In this case, σ_A and σ_B represent the individual collision diameters of TMG and NH_3 having values of 5.47 Å [37] and 2.92 Å [41], respectively. The activation energy for the forward reaction is 0 kcal/mol indicating adduct formation is spontaneous. Similarly, the rate of trimer formation represented by reaction G7 also is expressed as being collision limited and is governed by the probability of a three-body collision between three dimethylgallium amide molecules. The termolecular collision rate is given by

$$k = \pi\sigma_A^5 \left(\frac{8k_B T}{\pi m_A} \right)^{0.5} \quad (4.22)$$

where the collision diameter, σ_A , of $(\text{CH}_3)_2\text{Ga}:\text{NH}_2$ is calculated to be 5.39 Å based on group contribution methods [41] and m_A is the mass of $(\text{CH}_3)_2\text{Ga}:\text{NH}_2$.

Up to this point, we have only discussed gas phase reactions that can occur

between TMG and ammonia. Gas surface reactions which describe the interaction of gas phase species with a reactive surface also are included in this model and are shown in Table 4.2. The rate of all adsorption reactions is assumed to be controlled by two factors: the rate of collision of gas-phase species with the surface and the fraction of incident molecules which become adsorbed. Therefore, the adsorption rate of the i th species, R_i^S , can be expressed as the product of the flux of species i , F_i , and its sticking probability, S_i .

$$R_i^S = F_i \cdot S_i \quad (4.23)$$

The sticking probability lies in the range $0 \leq S_i \leq 1$, where the two extremes correspond to no molecules being adsorbed or complete adsorption of all incident molecules, respectively. The flux, F_i , is derived from the kinetic theory of gases and governed by the Hertz-Knudsen equation [40]:

$$F_i = \frac{P}{(2\pi m_i R_{gas} T)^{0.5}} \cdot x_i \quad (4.24)$$

Here F_i represents the flux of species i (mol/area/time), P the total pressure, m_i is the molecular weight of species i , R_{gas} is the ideal gas constant, T is the temperature, and x_i corresponds to the mole fraction of species i in the gas phase above the surface.

In our model, we assume that the activation energies are all set to 0 kcal/mol. The sum of the fluxes of TMG, DMG, MMG, Ga, DMG:NH₂, and GaN are assumed to govern the growth rate, and accordingly, sticking probabilities for those species are set equal to unity while sticking probabilities for the remaining species are set to zero.

A material balance is written for each chemical species

$$\frac{1}{R} \frac{d}{dR}(cx_i u R) = R_i^G + \frac{2R_i^S}{\Delta Z/2} \quad (4.25)$$

Here c is the total concentration of the gas ($c = P/R_{gas}/T$ for an ideal gas, P is the total reactor pressure, and R_{gas} corresponds to the ideal gas constant), x_i is the mole fraction of the i th species, ΔZ the distance between the top and bottom showerhead plates, R_i^G the rate of generation of species i per unit volume due to gas phase reactions and R_i^S the rate of generation of species i per unit area due to surface phase reactions. The quantity $2R_i^S$ results from the assumption that deposition occurs on both the bottom and top showerhead plates.

Equation 4.25 is written for each annular segment in the showerhead (region between hole rings). The temperature profile within each annular segment is assumed to be a linear fit between the trailing and leading segment gas temperatures, derived from the stair-like function shown in Figure 4.5. The velocity profile within each annular segment then is computed through the equation of continuity

$$\frac{d}{dR}(u\rho R) = 0 \quad (4.26)$$

It should be noted that the equation of continuity used for the transport-reaction model developed in this section is slightly different than the one used in (4.4) in order to maintain accurate chemical species material balances. In addition, inlet mole fractions for all chemical species are set equal to the corresponding outlet mole fractions from the previous segment.

Species mole fraction distributions of each chemical species are shown in Figure 4.6 based on the nominal set of operating conditions: pressure = 200 Torr; susceptor

temperature = 1308 K; total flow (NH₃ + H₂) = 20 slm. The results indicate that the adduct molecule, TMG:NH₃, is the major gallium-containing species present until a radial position of 2 cm. Thereafter, as the gas temperature increases, other reactions become significant producing an array of gallium-containing species.

The deposition rate profile is a function of the gas phase mole fraction of TMG, DMG, MMG, Ga, DMG:NH₂, and GaN and is represented by

$$\Delta(R) = \sum_{i=1}^N R_i^S \cdot x_i \quad (4.27)$$

The deposition pattern predicted from the model corresponding to nominal reactor operating conditions is compared to experimental observations in Figure 4.7. The model accurately captures the deposition pattern left in the showerhead after one run and now will be used to explore the interaction between the transport of reactants, adduct formation chemistry, and deposition kinetics. All simulations were done using the quadrature-based weighted residual method techniques of Adomaitis [15].

4.4 Experimental and Model Validation

4.4.1 Experimental Procedure

The experimental procedure was conducted in such a way to allow for both qualitative and quantitative model validation. Before starting each growth run, the showerhead was placed onto a scale to record its *pre-growth* weight. Typical growth times for GaN were 45-60 minutes. Upon completion of the growth run, the showerhead was removed from the reactor and again placed on the scale to record

its *post-growth* weight to determine the change in showerhead weight attributable to deposition incurred during the growth run. Additionally, a picture of the showerhead deposition pattern was taken. Finally, the showerhead was placed in HF cleaning solution to remove as much of the deposits as possible. It should be noted that the normal lifetime of a showerhead is typically six or seven growth runs.

4.4.2 Qualitative Comparison

To test the validity of the reaction-transport model it seemed most reasonable to study the effect susceptor temperature has on showerhead deposition; any change in susceptor temperature will directly influence gas temperature inside the showerhead, effectively changing the intrinsic showerhead kinetics and the corresponding deposition pattern. Experiments were performed for three different susceptor temperatures while keeping all other growth parameters constant (reactor pressure, precursor flow rates, showerhead hole pattern, showerhead to susceptor gap, etc.). The temperature range was expanded as much as possible (within reasonable reactor limitations) in order to elucidate its effect on the observed showerhead deposition patterns. Experiments were performed for susceptor temperatures of 1123 K, 1308 K, and 1523 K. Qualitative comparison between model predictions and observed showerhead deposition patterns are shown in Figure 4.7 for the three cases. The colors for each plot are normalized with respect to the maximum deposition rate calculated for that particular showerhead.

The experiments reveal significant differences in showerhead deposition pat-

terns as susceptor temperature is changed. The area of the central region of the showerhead where little or no deposition occurs is significantly different in the three cases. The central region of the showerhead corresponding to $T_{sus} = 1123$ K is much larger in comparison to $T_{sus} = 1308$ K. Moreover, most of the deposition for the low temperature case occurs towards the outer edge. It should be noted that the black residue are deposits on the outside of the showerhead and should be ignored in the comparison. The exact opposite is observed in the case where the $T_{sus} = 1523$ K. In this case more deposition is seen towards the showerhead center and less towards the outer edges.

In addition to the visual comparison illustrated in Figure 4.7, MATLAB's image processing toolbox [53] was utilized to correlate the color pattern of the showerhead deposits in the experimental photographs to film thickness. In this approach, the showerhead images were (1) imported into MATLAB; (2) converted into a grey scale format; (3) placed onto a quadrature-grid to enable accurate interpolation [15]; and (4) rotated for the purpose of averaging. Cross-sectional slices of the rotationally averaged showerhead deposits for the three susceptor temperatures are shown in Figure 4.8.

The results reveal several key points about this system. For the nominal ($T_{sus} = 1308$ K) and low temperature ($T_{sus} = 1123$ K) cases, the qualitative study results indicate that the showerhead reaction-transport model is valid. The inward movement of the deposition zone with increasing temperature is clearly seen in these results and for normal operating conditions the model does a good job of predicting experimental deposition patterns in the showerhead.

However, for the high temperature ($T_{sus} = 1523$ K) run, the results indicate that unmodeled phenomena may be at work in this system. It is reasonable to believe that at high growth temperatures, greater heating of the feed tube may take place resulting in significant gas phase reactions occurring upstream of the showerhead. To capture these phenomena, more detailed modeling of the gas delivery system upstream of the showerhead is required together with experiments to validate the heat transfer characteristics of the system upstream of the showerhead. Likewise, it is possible that additional experimental runs between the nominal temperature and high temperature regime may shed more light on the differences seen here. However, equipment availability and other resource limitations prevent such a study at this time.

4.4.3 Quantitative Comparison

In addition to model validation based solely on qualitative means, quantitative measurements also were performed, providing further evidence on the consistency of the reaction-transport model developed in this thesis. Our approach is to calculate from the model how much of the entering TMG is lost due to showerhead deposition and compare that to showerhead weight experiments. Using the model predictions, the calculation involves integration of the deposition rate profile and dividing the result by the total amount of TMG fed to the showerhead:

$$\epsilon_M = \frac{1}{\phi} \int_{R_{ft}}^{R_{sh}} \Delta(R) r dr \quad (4.28)$$

Here ϕ represents the total inlet feed of TMG into the showerhead (mol/s). Based on experiments, the amount of showerhead deposition is computed by

$$\epsilon_E = \frac{(W_{post} - W_{pre})}{\chi} \quad (4.29)$$

Here χ denotes the total inlet feed of TMG into the showerhead (grams) and W_{post} and W_{pre} refer to post-growth and pre-growth weights of the showerhead (grams). Figure 4.9 compares results between model predictions and experiments. Once again, model predictions are in good agreement to the experimental data for susceptor temperatures between 1123 K and 1523 K. It should be noted that no adjustable parameters have been included in the kinetic model, and minimal parameter fitting was done with respect to the thermal model. The only heat transfer model parameter that was fitted to the data was the liner gold coat fraction (γ). A value of $\gamma = 0.77$ was found to be the best fit to the data, a reasonable value based on the physical design of the reactor system.

4.4.4 Discussion of Results

Both the showerhead design and the reactor operating conditions have a significant influence on the selectivity of reaction pathways and on the observed showerhead deposition patterns. We begin a discussion of the showerhead deposit patterns by analyzing the deposition process from a modeling perspective. Figure 4.10 shows the spatial distribution of the adduct molecule, TMG:NH₃, for all three susceptor temperatures. Taking a closer look at the TMG:NH₃ profile for $T_{sus} = 1308$ K, as the precursors enter the showerhead, the temperature of the gas is cool, and the only

gas-phase reaction that occurs is the spontaneous formation of the adduct species. As the adduct molecules flow radially through the showerhead they can do either of two things: exit the showerhead through the hole rings or remain in the showerhead and begin to participate in further gas phase reactions downstream. It is important to note that the adduct molecule has a sticking probability equal to zero in our model and so the adduct species does not contribute to the deposition pattern. For $T_{sus} = 1308$ K, the adduct is the major gallium-containing species until the third hole ring junction (approximately $R = 2$ cm) and, therefore, little or no deposition will occur until this location.

After the third hole ring junction, the temperature of the gas in the showerhead is sufficiently high to promote further gas phase reactions, in particular, adduct dissociation to produce TMG and NH_3 (the lower route in Figure 3.1) or methane elimination to form DMG:NH_2 (upper route). This is reflected by the decrease in adduct concentration starting at the third hole ring location shown in Figure 4.10. Both reaction pathways are believed to occur based on our modeling work. The upper pathway leads to DMG:NH_2 which can either deposit inside the showerhead, exit the showerhead, or undergo a three-body collision to form the trimer molecule. The lower pathway of Figure 3.1 produces an array of sub-alkyls, each having the potential to deposit inside the showerhead.

We believe that the direct sticking of these molecules (TMG, DMG, MMG, Ga, GaN, and DMG:NH_2) is what is responsible for the deposition observed in the showerhead. Contrary to typical epitaxial growth involving adsorption, desorption, surface migration, and surface reactions, we hypothesize that the deposition in the

showerhead is a result of these molecules merely sticking to the surface. Thus, the combination of carbon, nitrogen, hydrogen, and gallium atoms present in many of the depositing species may be the basis for the dark brownish deposits seen in the showerhead.

Returning to Figure 4.10, let us explain what happens to the TMG:NH₃ profiles for when the T_{sus} is reduced to 1123 K or increased to 1523 K. When the susceptor temperature is decreased to 1123 K, the gas temperature profile within the showerhead decreases. Accordingly, gas phase reactions stemming off from the initial adduct formation do not become significant until further downstream. Therefore, in this case, showerhead deposition will not occur until about the fifth hole ring junction. Furthermore, a smaller fraction of the total inlet TMG will deposit as more of the adduct has an opportunity to exit the showerhead.

On the other hand, raising the susceptor temperature will have the opposite effect on showerhead deposition. An increase in susceptor temperature causes the gas temperature profile within the showerhead to increase. Adduct dissociation and methane elimination begin to occur much earlier causing deposition to occur closer to the showerhead center.

Table 4.1: Representative gas-phase reaction scheme of gallium nitride growth from trimethylgallium and ammonia included in the model for the single wafer MOVPE reactor showerhead system. Activation energies are in (kcal/mol) and pre-exponentials are in $(cm^3/mol)^{\alpha-1}sec^{-1}$, where α is the order of reaction. Rate constants are given by $k = k_0 T^n exp(-E_a/RT)$.

| <i>Rxn. No</i> | <i>Reactions</i> | k_0 | E_a | n | <i>Ref.</i> |
|----------------|--|----------------------|-------|-----|-------------|
| G1 | $(CH_3)_3Ga \rightarrow (CH_3)_2Ga + CH_3$ | 3.5×10^{15} | 59.5 | 0.0 | [32] |
| G2 | $(CH_3)_2Ga \rightarrow (CH_3)Ga + CH_3$ | 8.7×10^7 | 35.4 | 0.0 | [32] |
| G3 | $(CH_3)Ga \rightarrow Ga + CH_3$ | 1.0×10^{16} | 77.5 | 0.0 | [32] |
| G4 | $(CH_3)_3Ga + NH_3 \rightarrow (CH_3)_3Ga : NH_3$ | coll.(4.20) | 0.0 | 0.0 | [5] |
| G5 | $(CH_3)_3Ga : NH_3 \rightarrow (CH_3)_3Ga + NH_3$ | 9.5×10^9 | 18.5 | 0.0 | [8] |
| G6 | $(CH_3)_3Ga : NH_3 \rightarrow (CH_3)_2Ga : NH_2 + CH_4$ | 1.0×10^{14} | 49.0 | 0.0 | [5] |
| G7 | $3[(CH_3)_2Ga : NH_2] \rightarrow [(CH_3)_2Ga : NH_2]_3$ | coll.(4.22) | 0.0 | 0.0 | [5] |
| G8 | $[(CH_3)_2Ga : NH_2]_3 \rightarrow 3GaN + 6CH_4$ | 4.0×10^{15} | 60.0 | 0.0 | [8] |

Table 4.2: Representative surface-phase reaction scheme for gallium nitride growth included in the model for the single wafer MOVPE reactor showerhead system. S represents a free surface site.

| <i>Rxn. No</i> | <i>Reactions</i> | k_0 | E_a |
|----------------|--|---------|-------|
| S1 | $(CH_3)_3Ga + S \rightarrow Ga(s) + 3CH_3$ | $S_1=1$ | 0.0 |
| S2 | $(CH_3)_2Ga + S \rightarrow Ga(s) + 2CH_3$ | $S_2=1$ | 0.0 |
| S3 | $(CH_3)Ga + S \rightarrow Ga(s) + CH_3$ | $S_3=1$ | 0.0 |
| S4 | $Ga + S \rightarrow Ga(s)$ | $S_4=1$ | 0.0 |
| S5 | $(CH_3)_3Ga : NH_3 + 2S \rightarrow GaN(s) + 3CH_4$ | $S_5=0$ | 0.0 |
| S6 | $(CH_3)_2Ga : NH_2 + 2S \rightarrow GaN(s) + 2CH_4$ | $S_6=1$ | 0.0 |
| S7 | $[(CH_3)_2Ga : NH_2]_3 + 6S \rightarrow 3GaN(s) + 6CH_4$ | $S_7=0$ | 0.0 |
| S8 | $GaN + S \rightarrow GaN(s)$ | $S_8=1$ | 0.0 |

Figure 4.1: Single wafer MOVPE reactor showerhead system.

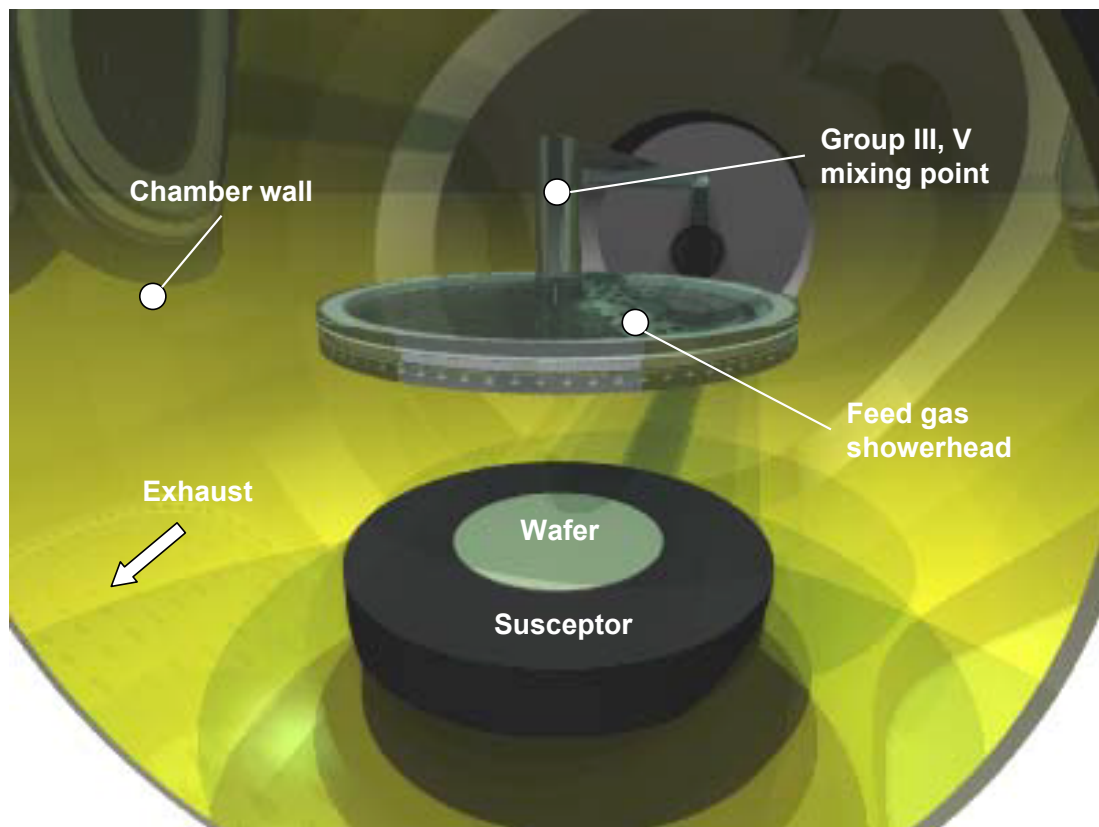


Figure 4.2: Showerhead deposition pattern: before growth run (top) and after growth run (bottom).



Figure 4.3: A cross-sectional view of the showerhead configuration and notation for the design parameters and simulation variables.

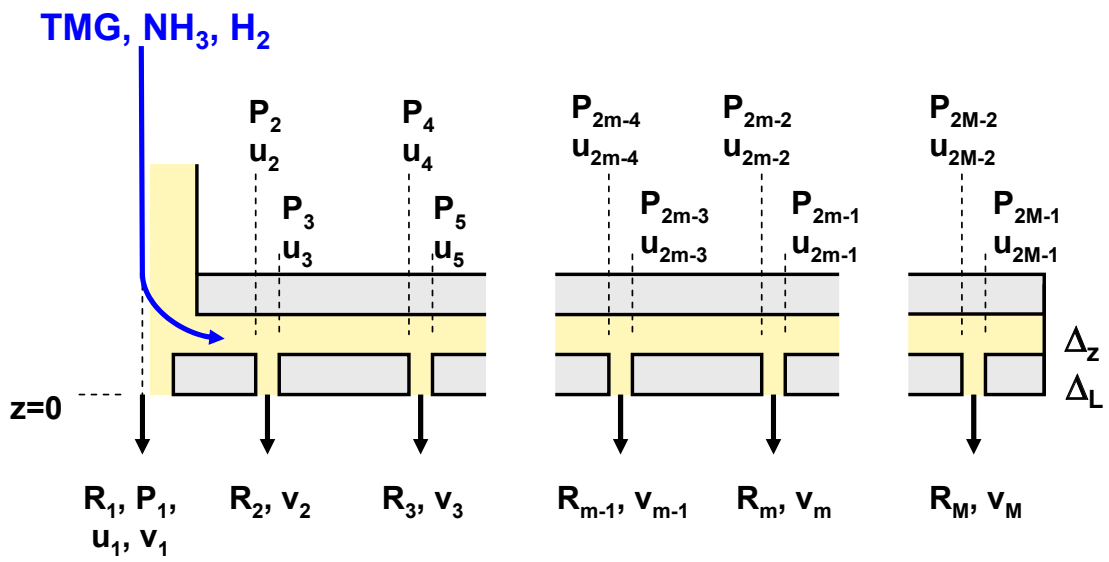


Figure 4.4: A cross sectional view of a showerhead annular segment, showing all relevant heat transfer terms.

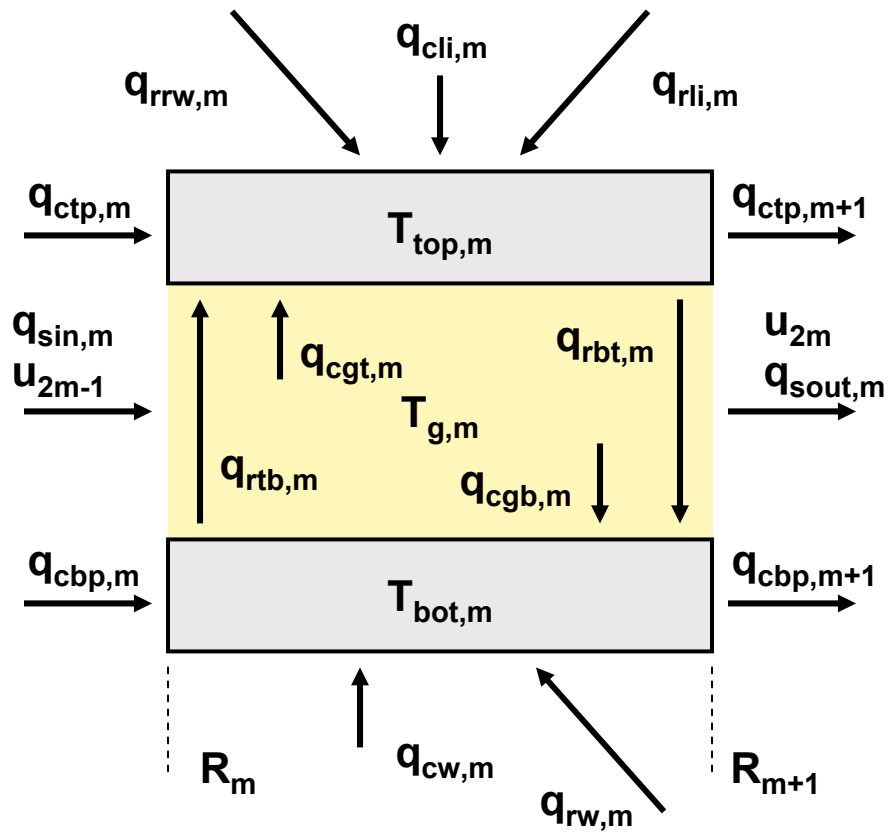


Figure 4.5: Showerhead gas temperature along with top and bottom plate temperatures (upper left); gas density (upper right); gas velocity (lower left); and pressure (lower right) for nominal set of operating conditions: pressure = 200 Torr; susceptor temperature = 1308 K; total flow($\text{NH}_3 + \text{H}_2$) = 20 slm.

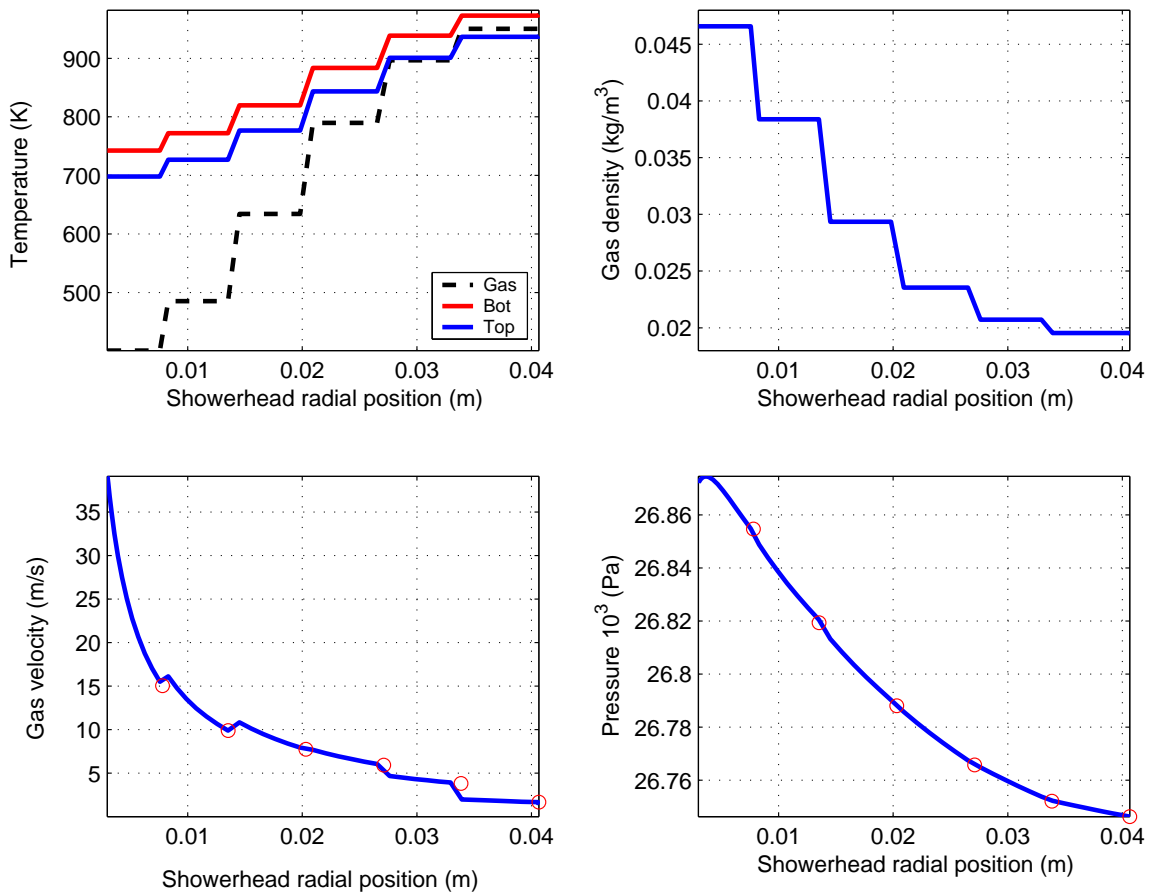


Figure 4.6: Chemical species mole fraction distributions within the showerhead.

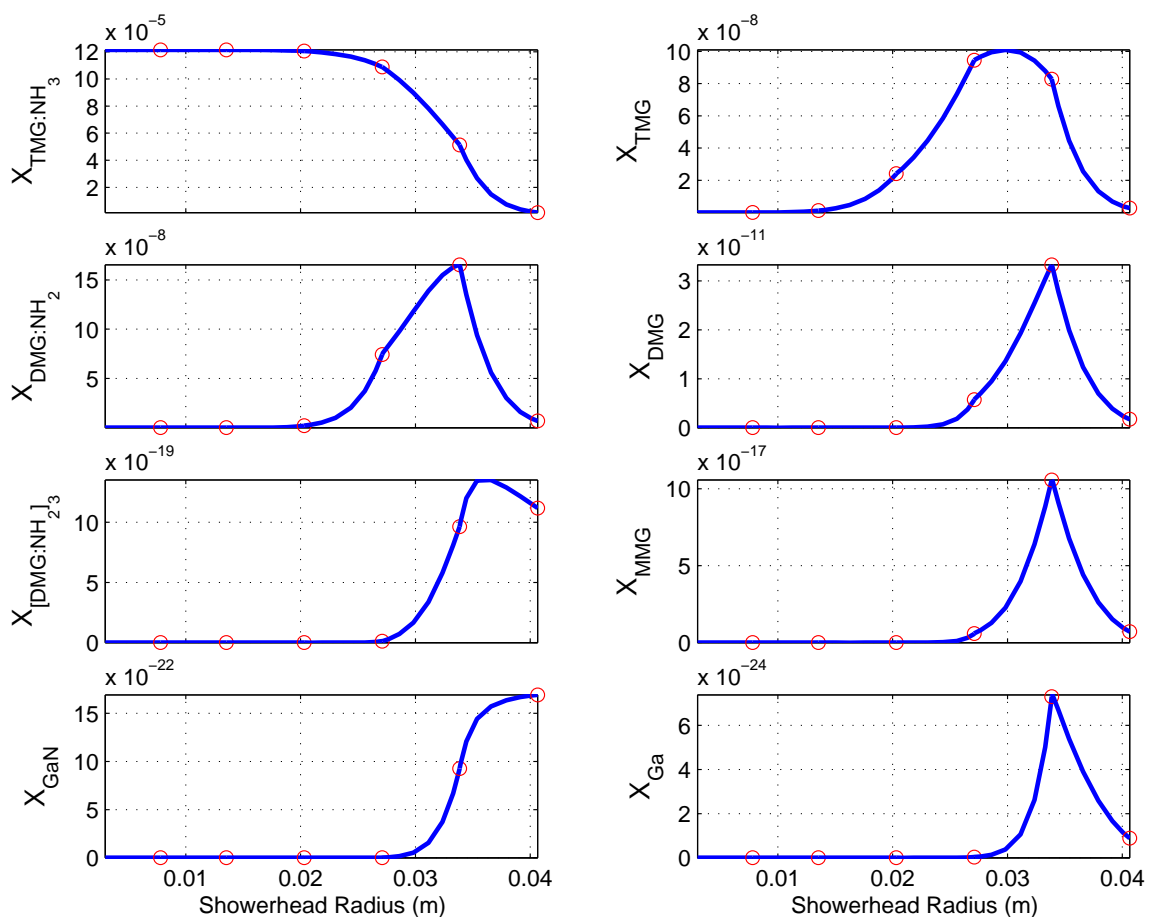


Figure 4.7: Qualitative comparison between model predictions and observed showerhead deposition patterns: $T_{sus} = 1123$ K (top); $T_{sus} = 1308$ K (middle); $T_{sus} = 1523$ K (bottom). The colors for each plot are normalized with respect to the maximum deposition rate calculated for that particular showerhead.

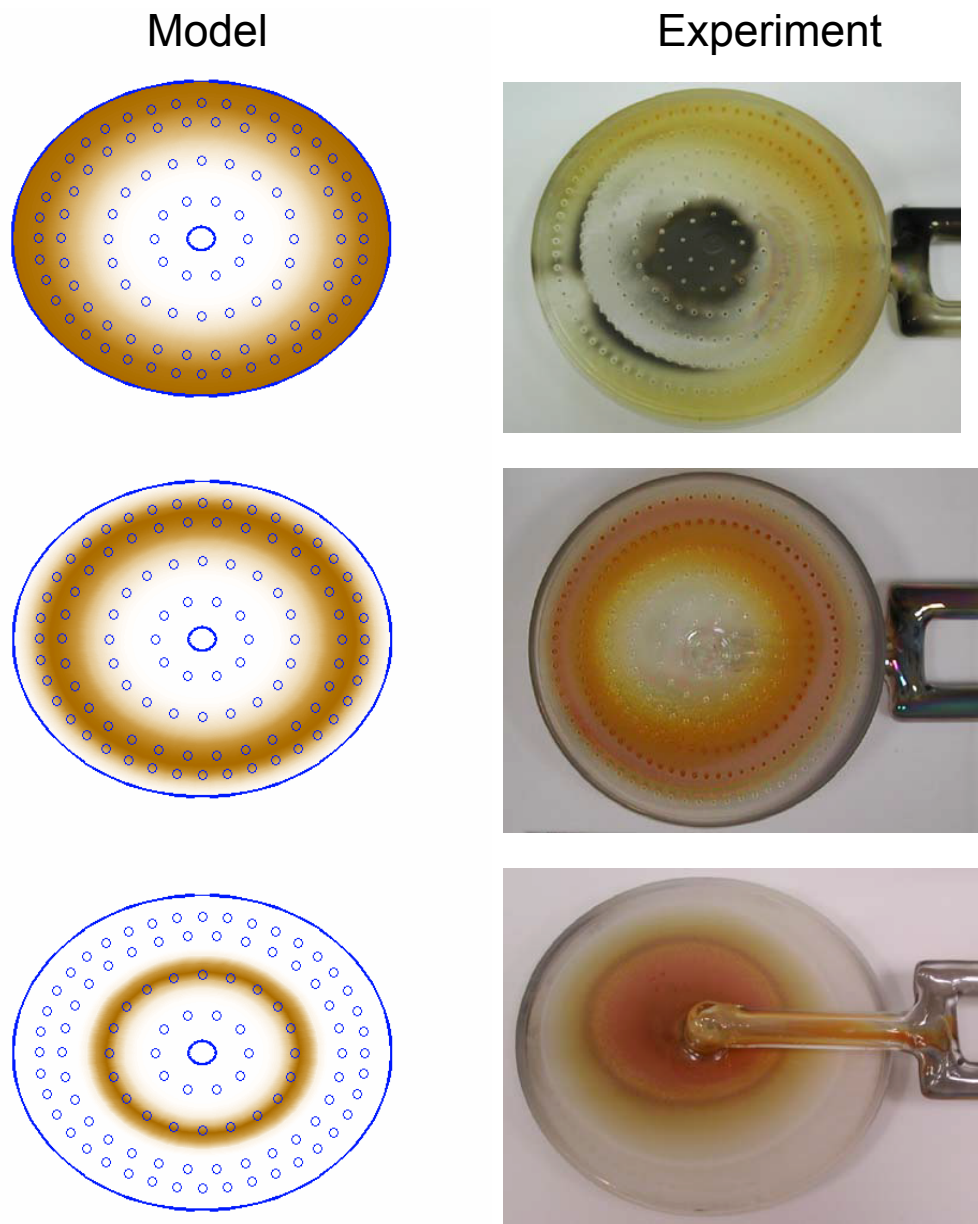


Figure 4.8: Qualitative comparison between model predictions and observed showerhead deposition patterns using MATLAB image processing toolbox. $T_{sus} = 1123$ K (top); $T_{sus} = 1308$ K (middle); $T_{sus} = 1523$ K (bottom)

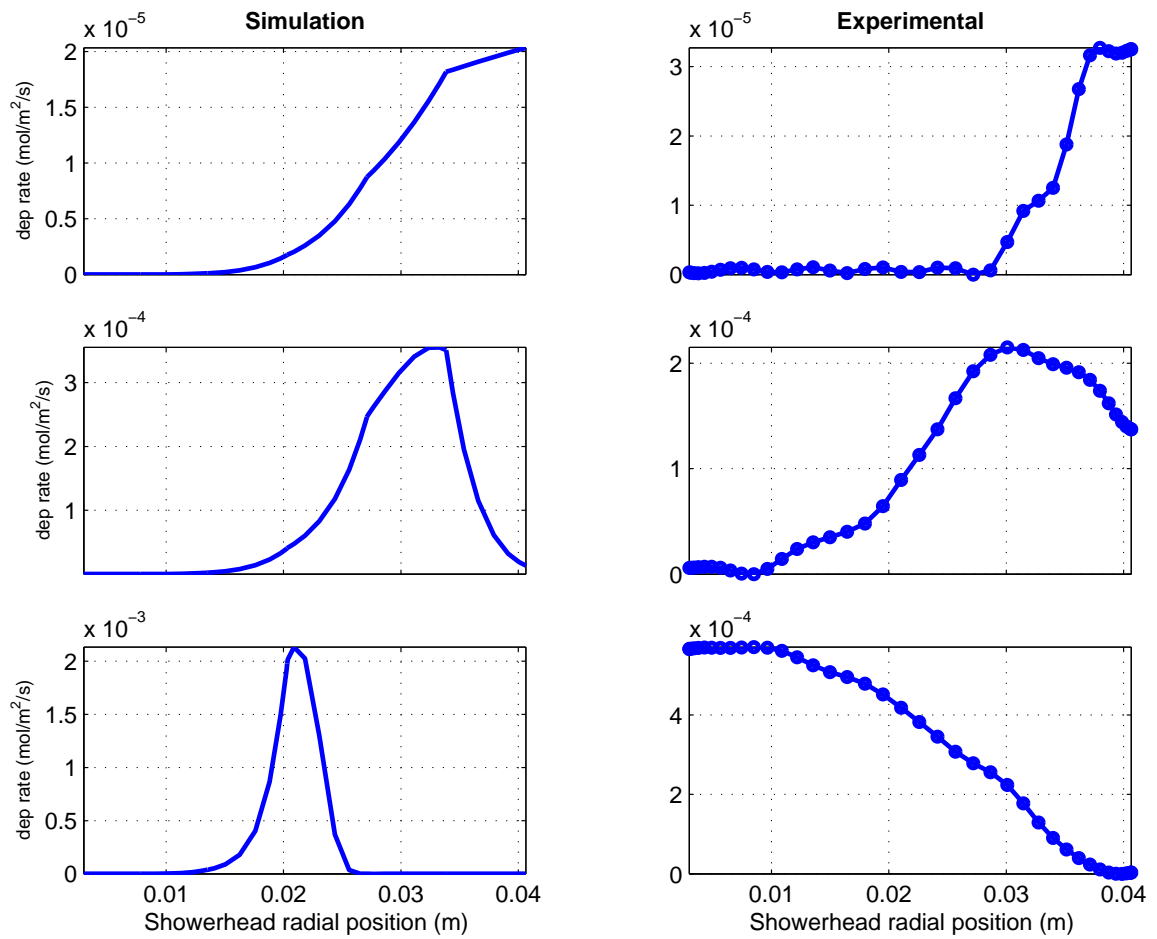


Figure 4.9: Quantitative comparison between model predictions and showerhead deposition experiments: total Ga-containing species deposition.

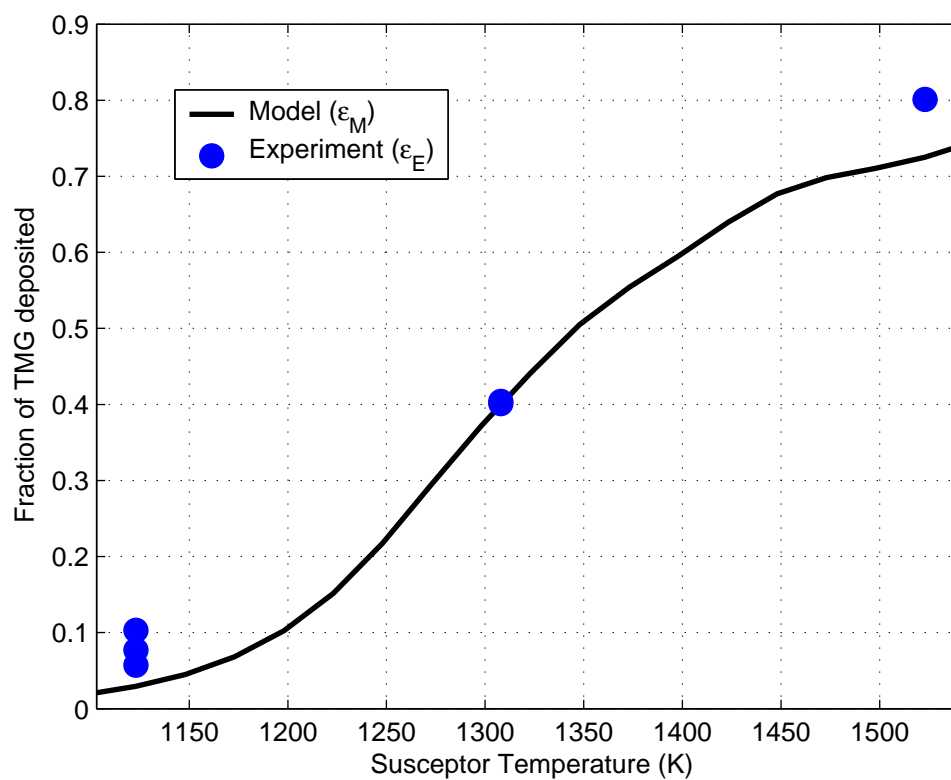
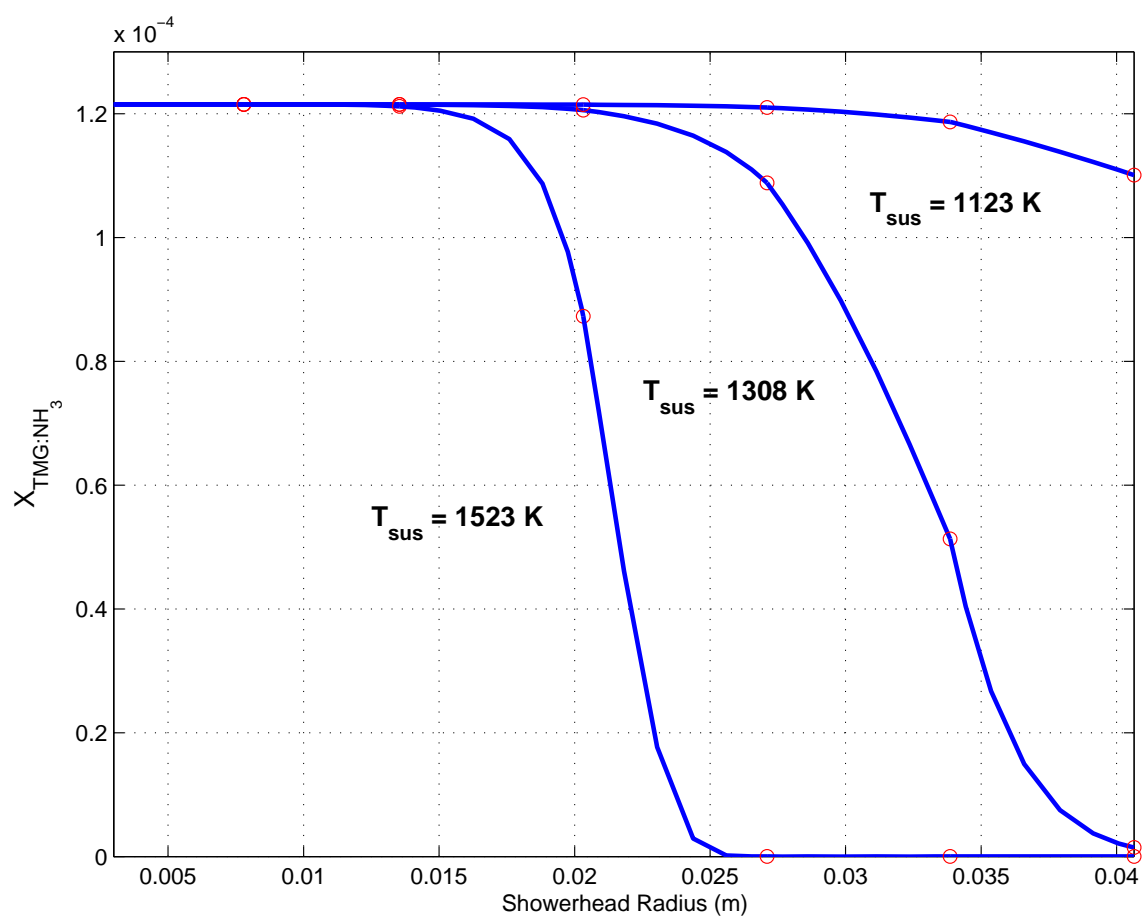


Figure 4.10: Spatial distribution of adduct molecule for three susceptor temperatures. Showerhead hole rings are marked by the red circles



Chapter 5

A NEW CRITERION FOR UNIFORMITY CONTROL

5.1 Uniformity Modes

Recently, an approach to film uniformity control in planetary reactor systems was proposed in [14] based purely on the geometry of radial flow reactors with the mode of wafer rotation. In this approach, a sequence of stalled-wafer (non-rotating) deposition profiles are identified that, when rotated, produce perfectly uniform films. Then, a deposition profile, produced either by simulation or by an actual CVD process is projected onto this sequence of uniformity-producing profiles to compute the "Nearest Uniformity Producing Profile" (NUPP), which under rotation would produce a uniform film. Thus, it becomes clear that one would want to drive the current profile to the "nearest" optimal profile, NUPP, giving an unambiguous optimization criterion. Most importantly, the NUPP provides the process engineer with physical insight on how reactor operating conditions should be modified to drive the current profile towards the NUPP to improve uniformity. This technique is extremely powerful because it can be applied to not only film thickness but any distributed film quality for either process development or in a run-to-run control system.

For any reactor configuration, we define reactor $\Omega(x, y)$ and wafer $\omega(r, \theta)$ physical domains (Figure 5.1). Film growth takes place in Ω ; a film property $\Delta(x, y)$ we

wish to make spatially uniform is defined in at least a portion of this domain. Given the complete basis function sequences $\{\phi_i(x)\}_{i=1}^{\infty}$ and $\{\psi_j(y)\}_{j=1}^{\infty}$, we can represent this film property by

$$\begin{aligned}\Delta(x, y) &= \sum_{i,j=1}^{\infty} a_{i,j} \phi_i(x) \psi_j(y) \\ &\approx \sum_{i,j=1}^{I,J} a_{i,j} \phi_i(x) \psi_j(y)\end{aligned}$$

where the finite truncation numbers I, J can be used because of diffusion and other physical phenomena that limit the maximum length scale that must be resolved by the basis function expansion; for this work we find $I = 10$ and $J = 1$ are sufficient to resolve the wafer deposition profiles.

Defining \mathcal{P} as the operator that projects Δ onto ω :

$$\begin{aligned}\delta(r, \theta) &= \mathcal{P}\Delta(x, y) \\ &= \sum_{i,j=1}^{I,J} a_{i,j} \mathcal{P}\phi_i(x) \psi_j(y) \\ &= \sum_{i,j=1}^{I,J} a_{i,j} p_{i,j}(r, \theta)\end{aligned}$$

Representative $p_{i,j}$ are shown in Figure 5.2.

Defining \mathcal{R} as the operator that determines the rotationally-averaged δ profiles:

$$\begin{aligned}\bar{\delta}(r) &= \mathcal{R}\delta(r, \theta) \\ &= \sum_{i,j=1}^{I,J} a_{i,j} \mathcal{R}p_{i,j}(r, \theta) \\ &= \sum_{i,j=1}^{I,J} a_{i,j} \alpha_{i,j}(r)\end{aligned}$$

Now, we classify the $p_{i,j}$ according to the $\alpha_{i,j}$ each produces:

- **Uniform** $\alpha_{i,j}$ These include the set $\{p^0\}_{n=1}^{n_0}$ is defined as all $p_{i,j}$ corresponding to trivial (zero value) $\alpha_{i,j}$, and the set $\{\bar{p}\}_{n=1}^{\bar{n}}$ is defined as all $p_{i,j}$ corresponding to uniform and nonzero $\alpha_{i,j}$. Even if trivial, these modes will be included as part of the uniformity producing subspace.
- **Nonuniform** $\alpha_{i,j}$ The set $\{\hat{p}\}_{n=1}^{\hat{n}}$ is defined as all $p_{i,j}$ corresponding to nonuniform and nonzero $\alpha_{i,j}$. This is the subspace that contains all nonuniformity producing profiles and some uniformity producing profiles, requiring further analysis to separate the two. The rotationally averaged modes corresponding to \hat{p} are $\hat{\alpha}$.

5.1.1 Uniformity Producing Profiles in $span\{\hat{p}\}$

We define the sequence of functions α^V as

$$\alpha^V = span\{\hat{\alpha}\}$$

and compute the set of α^V using the singular value decomposition procedure; the orthogonalization process removes redundant $\hat{\alpha}$; the process can be written in matrix form

$$\alpha^V = \mathbf{V}\hat{\alpha}$$

where \mathbf{V} are the right singular vectors from the SVD.

Our goal at this point is to determine the subspace of $span\{\hat{\alpha}\}$ corresponding to perfectly uniform profiles; one approach is to use the following algorithm:

1. Set $n_{st} = 1$

2. Compute α^V corresponding to $\{\hat{\alpha}_n\}_{n_{st}}^{\hat{n}}$ where \hat{n} is the total number of functions in $\hat{\alpha}$
3. Determine the coefficients \mathbf{b} by projecting the α^V onto a perfectly uniform rotationally averaged profile with numerical value 1:

$$\epsilon_{nst} = \min_{\mathbf{b}} \left\| \sum_j b_j \alpha_j^V - 1 \right\|$$

4. For ϵ_{nst} smaller than a tolerance given by physical grounds related to the specific uniformity control problem, using the computed \mathbf{b} , we reconstruct the stalled wafer profiles that give uniform films under rotation using

$$\mathbf{b}^T \alpha^V = \mathbf{b}^T \mathbf{V} \alpha$$

Replacing each α in the equation above with its corresponding \hat{p} gives the uniformity producing mode $\hat{\beta}_{nst}$:

$$\hat{\beta}_{nst} = \mathbf{b}^T \mathbf{V} \hat{p}$$

5. Set $n_{st} = n_{st} + 1$ and return to Step 2.

When we can no longer find uniformity producing modes that satisfy the error tolerance set for ϵ , we orthogonalize and normalize the $p^0 \cup \bar{p} \cup \hat{\beta}$ modes to produce the basis

$$\{\beta_n\}_{n=0}^N$$

spanning $p^0 \cup \bar{p} \cup \hat{\beta}$ and defining all uniformity producing wafer profiles in that subspace. Representative β_n modes are shown in Figure 5.3. Note that when generating the sequence $\hat{\beta}_n$, we remove the α_m , $m = 1, 2, \dots$ in turn, not the α_m^V .

5.1.2 Defining the Nearest Uniformity Producing Profile (NUPP)

Because all linear combinations of the final set of β_n modes are guaranteed to generate flat profiles, we can use these β_n to generate a useful basis onto which a deposition profile can be projected to immediately determine whether the particular profile will generate uniform films under rotation and, if it does not, predict the shape of the “nearest” profile that does. Likewise, we can use these modes as a part of an efficient means of optimizing the deposition process for uniformity. Defining the inner product of two functions,

$$\langle f, g \rangle = \int_0^{2\pi} \int_0^{r_w} (f(r, \theta)g(r, \theta))\rho(r, \theta)r \, dr \, d\theta$$

the NUPP is simply computed using the projection operation:

$$\text{NUPP:} \quad N_u(r, \theta) = \sum_{n=0}^N \beta_n(r, \theta) \langle \delta, \beta_n \rangle$$

In the definition of the inner product, $\rho = 1$ when the $\langle f, g \rangle$ notation is used, and is a specified function when $\langle f, g \rangle_\rho$ is used. A measure of distance between the current deposition profile and its NUPP can be minimized as part of a simulation-based process recipe development procedure or in a run-to-run control system; for example, one definition of the distance to the NUPP is to define the residual of the projection of a film property profile $\delta(r, \theta)$ onto the β_n modes:

$$S(r, \theta) = \delta(r, \theta) - N_u(r, \theta) \tag{5.1}$$

and so the distance to the NUPP can be computed using the weighted inner product $d = \langle S, S \rangle_\rho$ where the weight function ρ can be used to focus uniformity control on

regions of the wafer relevant to where devices are to be constructed (e.g., the central region of the wafer).

Figure 5.1: Quadrature grids over the deposition (larger/blue; $\Omega(x, y)$) and wafer domains (smaller/red; $\omega(r, \theta)$).

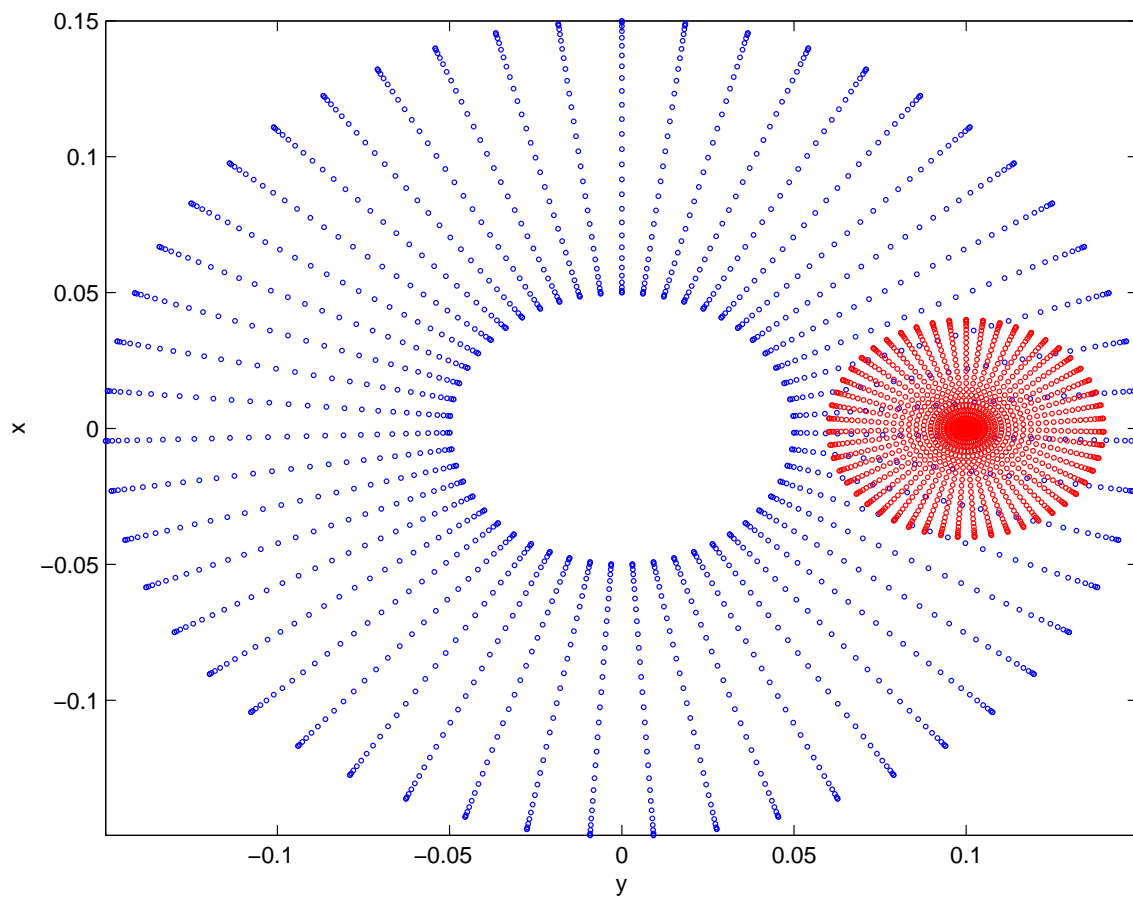


Figure 5.2: Projection of a complete set of basis function over the deposition domain onto the wafer domain $(p_{i,j})$.

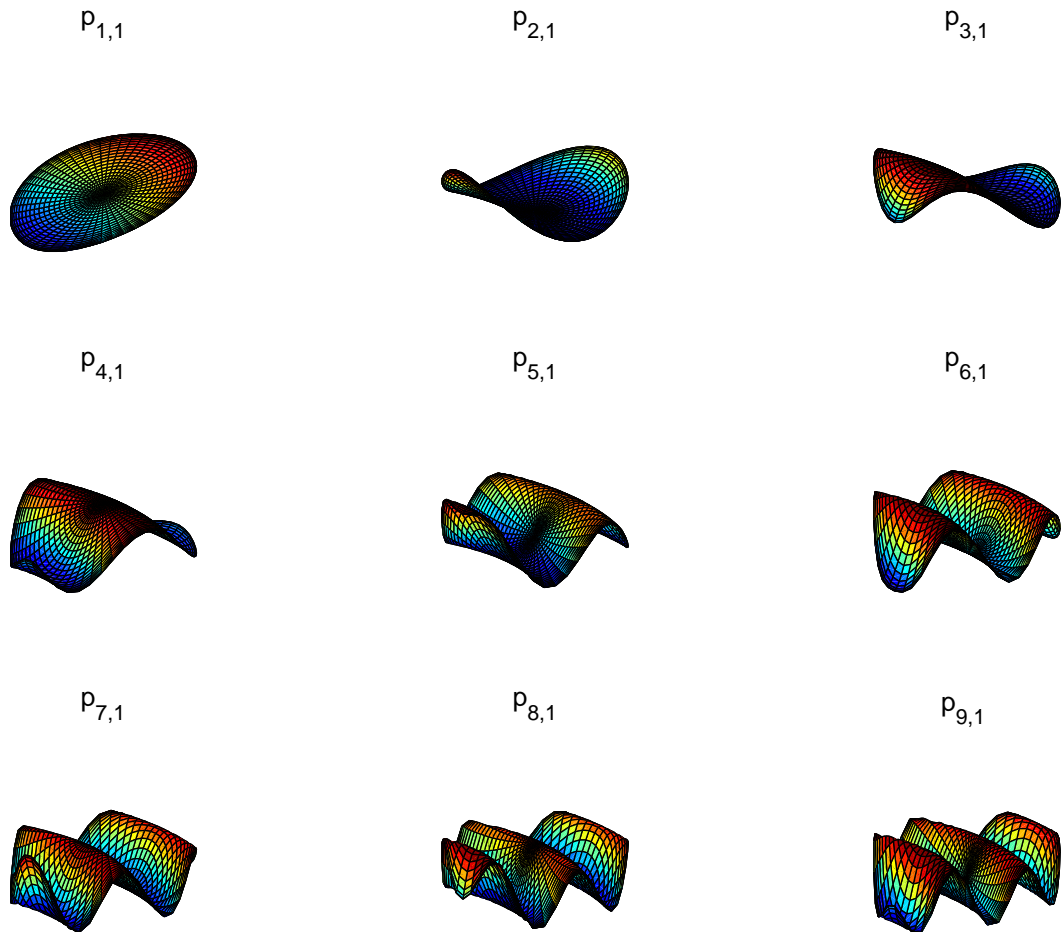
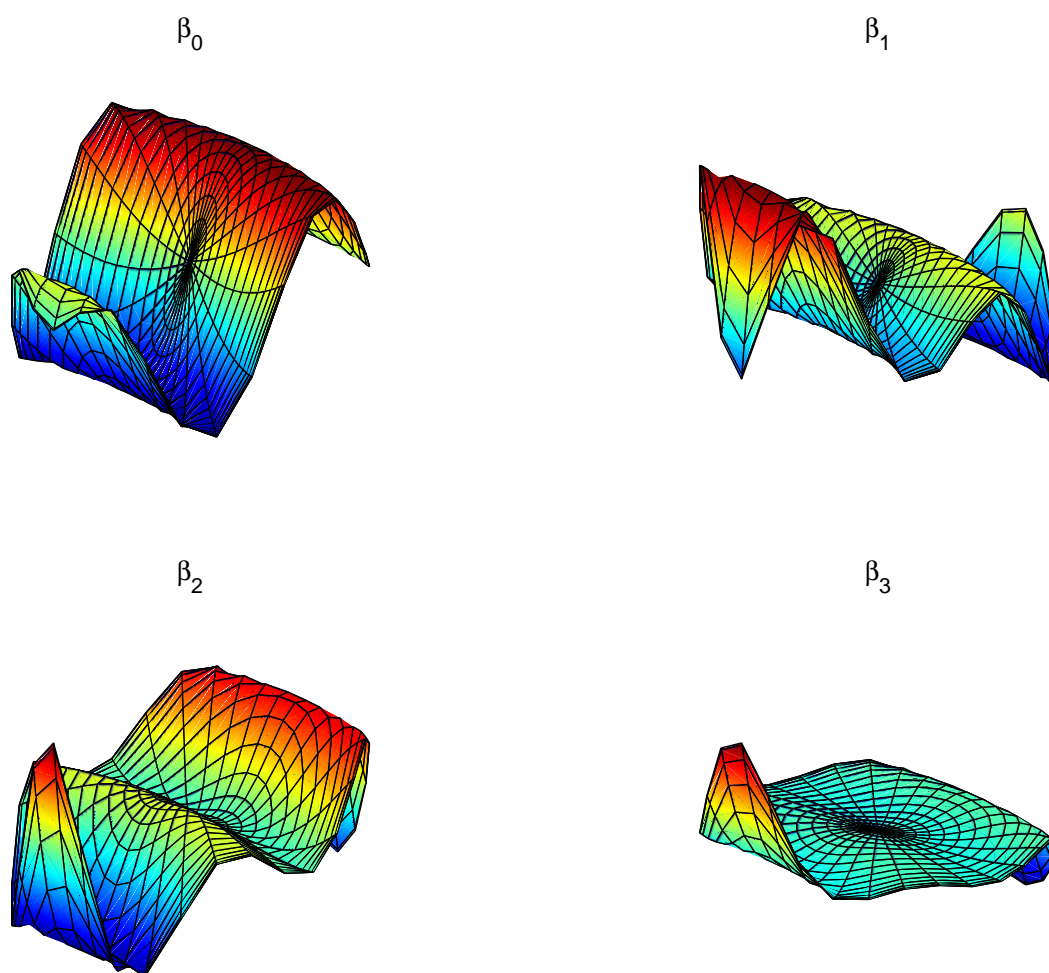


Figure 5.3: First four β_n modes spanning the space of all deposition profiles that produce perfectly uniform films under rotation for Δ .



Chapter 6

APPLICATION OF "NUPP" FOR FILM UNIFORMITY OPTIMIZATION IN A PLANETARY GaN CVD REACTOR SYSTEM

6.1 Planetary GaN CVD Reactor Model Development

The design of efficient CVD reactors requires a complete knowledge of the chemical kinetics that take place during the process. The choice of reactor operating conditions and physical designs have a significant influence on the selectivity among different reaction pathways, as is the case in GaN where two competing reaction pathways exist. Some studies have focused on careful design of gas delivery systems for GaN reactors in order to suppress or avoid the adduct formation pathway [5, 6]. In this section, we use the planetary radial-flow CVD reactor system to make the connection between reactor design and chemical kinetics as concrete as possible.

A vertical cross-sectional view of a radial-flow planetary reactor system along with its physical domain, $R_0 \leq R \leq R_{sus}$, is shown in Figure 6.1. The precursors and carrier gas species are injected into the center of the reactor through a 2-flow gas inlet design and flow outwards over wafers arranged in circular patterns over the susceptor. The 2-flow gas inlet design allows group III compounds to be introduced separately from group V compounds. In these reactors, the wafers are placed on

rotating satellites which in turn rotate around the central axis of the susceptor plate. The radial flow geometry combined with the substrate planetary motion mechanism is commonly employed to produce uniform deposition profiles on the wafers [54]. It should be noted that reactors of this type can be run with both rotating and stalled (non-rotating) wafers.

A detailed two-dimensional transport and reaction-kinetic model is developed for this reactor system. The goal here is to show a direct connection between reactor geometry, deposition kinetics, and operating parameters. This transport and reaction-kinetic model is based on fundamental equations accounting for momentum, heat, and mass-transfer within a compressible gas with temperature-dependent physical properties. Because the mixture of reactants and products in the carrier gas (H_2) is dilute, it is valid to neglect the heat of reaction along with any expansion or contraction of the mixture due to chemical reactions. Moreover, the precursor species and all products formed from subsequent reactions between the precursors exist in low concentration relative to the carrier gas. Therefore, multicomponent diffusion need not be considered and binary diffusion coefficients of the reactants and products in the carrier gas (H_2) are utilized. The continuity equation, equation of motion, equation of energy, and mass balances of each chemical species for temperature-dependent density (ρ), viscosity (μ), heat capacity (C_p), and thermal conductivity (k) are expressed as the following

Mass Continuity:

$$\nabla \cdot (\rho v) = 0 \tag{6.1}$$

Momentum Balance:

$$\rho \frac{Dv}{Dt} = -\nabla P - \nabla \cdot \tau + \rho g \quad (6.2)$$

subject to boundary conditions

$$\begin{aligned} v_R &= v_0 & P &= P_T & \text{at} & R = R_0 \\ \frac{dv_R}{dR} &= 0 & \frac{dP}{dR} &= 0 & \text{at} & R = R_{sus} \\ v_R &= 0 & \frac{dP}{dZ} &= 0 & \text{at} & Z = 0 \\ v_R &= 0 & \frac{dP}{dZ} &= 0 & \text{at} & Z = L \end{aligned}$$

Energy Balance:

$$\rho C_p (v \cdot \nabla T) = \nabla \cdot (k \nabla T) \quad (6.3)$$

subject to boundary conditions

$$\begin{aligned} v_R \rho C_p (T_0 - T) &= -k \frac{dT}{dR} & \text{at} & R = R_0 \\ \frac{dT}{dR} &= 0 & \text{at} & R = R_{sus} \\ T &= T_S & \text{at} & Z = 0 \\ \frac{dT}{dZ} &= 0 & \text{at} & Z = L \end{aligned}$$

Mass Balances:

$$\nabla \cdot (cx_i v) = \nabla \cdot [cD_i(\nabla x_i)] - R_i^G \quad (6.4)$$

subject to boundary conditions

$$\begin{aligned} x_i c v_R &= x_i^0 c v_R - c D_i \frac{dx_i}{dR} & \text{at} & R = R_0 \\ \frac{dx_i}{dR} &= 0 & \text{at} & R = R_{sus} \\ c D_i \frac{dx_i}{dZ} &= R_i^S & \text{at} & Z = 0 \\ -c D_i \frac{dx_i}{dZ} &= R_i^S & \text{at} & Z = L \end{aligned}$$

The term $(\frac{Dv}{Dt})$ in equation 6.2 represents the substantial time derivative.

In addition, the components of the viscous stress tensor (τ) in equation 6.2 for Newtonian fluids in cylindrical coordinates are:

$$\tau_{R R} = -\mu[2\frac{\partial v_R}{\partial R} - \frac{2}{3}(\nabla \cdot v)]$$

$$\tau_{\theta\theta} = -\mu[2\frac{v_R}{R} - \frac{2}{3}(\nabla \cdot v)]$$

$$\tau_{R Z} = -\mu[\frac{\partial v_R}{\partial Z}]$$

These equations in conjunction with their appropriate boundary conditions are used to compute the velocity (v), pressure (P), temperature (T), and species mole fraction (x_i) distributions for this system. The computational domain is shown in Figure 6.2. The computational domain extends from $R_0 \leq R \leq R_{sus}$ and $0 \leq Z \leq L$; where R_0 denotes the radius of the central feed tube and L is the spacing between the wafer top surface and the reactor roof which is assumed to be perfectly insulating. The notation used in (6.1-6.4) is the following: inlet gas velocity (v_0); total reactor pressure (P_T); inlet gas temperature (T_0); susceptor temperature (T_S); inlet mole fraction of species i (x_i^0); total concentration of the gas ($c = P_T/R_{gas}/T$ for an ideal gas where R_{gas} corresponds to the ideal gas constant); binary diffusion coefficients of species i (D_i); rate of generation of species i per unit volume due to gas phase reactions (R_i^G); and the rate of generation of species i per unit area due to surface phase reactions (R_i^S).

The system of non-linear partial differential equations, written in two coordinates (R and Z), were discretized by collocation and subsequently solved by implementing the Newton-Raphson method as described in chapter 2. The flow and heat transfer equations were solved first to compute the gas temperature and velocity distributions. The mass transfer and kinetic problem was subsequently solved on the same grid to compute the species distribution.

A representative set of operating parameters used to deposit gallium nitride for this reactor geometry is taken from Beccard et al. [55]. In their planetary reactor system, they reported the following operating conditions: pressure 37.5 torr, susceptor temperature (T_S) 1373 K, and a total flow 6.5 slm. Based on these parameters and assuming that the total flowrate of 6.5 slm is split equally between the top and bottom inlets, $T_0 = 300K$ and $L = 1.5cm$ [54], an initial value for $v_0 = 3.85m/s$ is computed.

There are two essential questions in the analysis of this system: 1) which chemical reactions should be considered for this reactor geometry and, 2) what Ga-containing species are present above the wafer location? For this system, the answer to these questions depends on two issues: the entrance mixing effect between the precursors and the temperature distribution of the gas. It is completely valid to assume that the 2-flow gas inlet design minimizes precursor interaction until shortly before the wafer location [55]. Therefore, the extent of TMG thermal decomposition (lower route) is computed for $R_0 \leq R \leq R_{sus}$ where $R_0 = 0.01m$, susceptor radius $R_{sus} = 0.2m$, satellite wafer centerline radius $R_s = 0.1m$ and wafer radius $r_w = 0.04m$. The sum of the fluxes of monomethylgallium (MMG) and elemental gallium

(Ga) are assumed to govern the growth rate and, accordingly, their surface reaction chemistry is also included in the computation.

Representative simulation results describing gas temperature and velocity distributions are shown in Figure 6.3. The results indicate rapid gas heating inside the reactor system. The increase in gas velocity observed shortly after the inlet is related to the rapid expansion of the gas due to density decrease associated with gas heating. The species mole fraction distributions of each chemical species are shown in Figure 6.4. The profiles are normalized with respect to the inlet TMG mole fraction. This was done because the precursor is fed into the reactor with the carrier gas, H_2 , which plays little or no role in gas-phase or surface-phase reactions. Therefore, the only chemical species that are of interest are TMG and its sub-alkyls. It is evident from the results that TMG is rapidly consumed well before the wafer location and that the only species present over the wafer are DMG, MMG, and Ga. This is directly related to the rapid gas heating inside the reactor which encourages the dissociation of the first methyl group from TMG. Because no TMG is present over the wafer, the adduct pathway (upper route) is suppressed as NH_3 begins mixing with the organometallic stream shortly before the wafer location. This is a perfect example of how reactor geometry influences deposition kinetics. The geometry of the planetary radial-flow reactor completely avoids the adduct route and drives the lower route, while at the same time, providing adequate mixing over the growth region.

In addition to the detailed 2D model, a simplified, but physically valid, one-dimensional model is developed for this reactor system. This simple 1D model will

serve as a convenient and computationally cost effective test bed for performing sensitivity analysis of reactor parameters to be carried out in this thesis. The equation of continuity for the total gas molar flow rate is used to obtain the gas velocity

$$\frac{d}{dR}(v\rho R) = 0 \quad \text{or} \quad v = \frac{v_0 R_0 T}{T_0 R} \quad (6.5)$$

where the assumption of the ideal gas law is used to determine an explicit relationship between gas temperature (T), radial position (R) and gas velocity (v). The energy balance equation in cylindrical coordinates is obtained by assuming (C_p) and (k) of the carrier gas are independent of temperature; the parameter values are evaluated using the average of the inlet temperature (T_0) and susceptor temperature (T_S):

$$C_p \frac{1}{R} \frac{d}{dR}(R\rho v T) = \frac{k}{R} \frac{d}{dR}(R \frac{dT}{dR}) + \frac{2k}{L^2}(T_S - T) \quad (6.6)$$

with boundary conditions

$$T = T_0 \quad \text{at} \quad R = R_0 \quad (6.7)$$

$$\frac{dT}{dR} = 0 \quad \text{at} \quad R = R_{sus} \quad (6.8)$$

Integrating this expression gives the steady-state temperature distribution of the gas inside the reactor. Finally, a material balance is written for each chemical species

$$\frac{1}{R} \frac{d}{dR}(cx_i v R) = R_i^G + \frac{2R_i^S}{L/2} \quad (6.9)$$

The quantity $2R_i^S$ assumes that deposition occurs on both the susceptor and reactor roof. The quantity $L/2$ represents the distance that Ga-containing precursors must travel in order to adsorb onto either the susceptor or reactor roof after the divider (refer to Figure 6.1). This is valid assuming both gaseous feed streams are set

to the same volumetric flowrate and spread evenly after the divider to fill half of the vertical volume. Initial conditions for each chemical species material balance equation is equal to known mole fractions at the inlet, $x_i(R = R_0) = x_i^0$. In addition, interaction between Ga-containing species and NH_3 molecules is neglected as Ga-containing species pass through the NH_3 phase and travel towards the wafer front.

The results describing gas temperature and mole fraction profiles computed from the 1D model are shown in Figures 6.5 and 6.6 respectively. The results indicate rapid gas heating inside the reactor system which compares well to the temperature profile calculated using the detailed 2D model. The results for mole fraction profiles also match well with the 2D model. The precursor, TMG, is rapidly consumed well before the wafer location and the only species present over the wafer are DMG, MMG, and Ga. Based on these results, we conclude that the 1D model can be used for the optimization studies discussed in the following section. It is important to mention that the detailed model could just as easily been used in the optimization studies to follow, but it is not essential in this case. Instead, the optimization will be performed with the 1D model, and the detailed 2D solution will be used after optimization for verification purposes.

6.2 Uniformity Optimization

The deposition rate profile is a function of the gas phase mole fraction of MMG and Ga and is given by

$$\Delta(R) = R_{MMG}^S \cdot x_{MMG} + R_{Ga}^S \cdot x_{Ga} \quad (6.10)$$

For the planetary reactor deposition system simulation under consideration, the “nearest” deposition rate profile f that generates a uniform film upon rotation is shown in Figure 6.7 for $T_S = 1373K$ and Total Flowrate = $6.5slm$. This optimal profile f , henceforth referred to as the NUPP (Nearest Uniformity Producing Profile), is computed as the projection of the deposition profile $\Delta(R)$ onto the β_n :

$$f = \sum_{n=1}^N \beta_n \int_0^{r_w} \Delta(R) \beta_n r dr$$

When f and Δ intersect at the wafer center $R = R_s$ ($R_s = 0.1$ in this diagram), $C_d = 0$ and we are guaranteed of uniformity in the center region of the wafer. These observations lead to an unambiguous design criterion of $C_d = 0$ for improved wafer uniformity in the central region of the wafer - in many cases, the region where uniformity is most desired.

From Figure 6.7, it is obvious that this criterion is not met, seeing as, δ_{bar} , which is the profile that results from rotation of the current $\Delta(R)$, is not uniform. However, the results immediately indicate that uniformity can be achieved if we could somehow shift the current deposition rate profile upward and to the right (northeast direction), so that the C_d value is minimized. Physical intuition based on knowledge of gallium nitride growth chemistry suggests decreasing the susceptor

temperature as a potential means to improving uniformity relative to the original set of operating conditions.

It is apparent from the chemistry, that a decrease in susceptor temperature will reduce the rates of the decomposition reactions, which in turn, should spread the peak of $\Delta(R)$ and push it toward the northeast direction. At the same time, lowering the susceptor temperature also will decrease the deposition rate. A minimization procedure was implemented to find the optimal susceptor temperature that minimizes C_d , guaranteeing a uniform deposition rate profile in the neighborhood of the wafer center. A plot of C_d versus T_S is shown in Figure 6.8. For this reactor system, we find the optimal susceptor temperature to be $T_S = 1312$ K. This analysis also reveals that the C_d value approaches zero at very low susceptor temperatures. This is expected because minimal decomposition of the precursor occurs in this regime causing $\Delta(R)$ to be nearly zero. Figure 6.9 clearly shows the improvement is uniformity in the center region of the wafer using the optimal susceptor temperature.

However, it is also obvious from Figure 6.9 that some degree of nonuniformity still exists towards the outer portion of the wafer. This occurs because $\Delta(R)$ and f do not completely overlap at the two ends of the wafer location. These results imply that modifying the susceptor temperature alone cannot be used to achieve uniform films over the entire wafer surface for this reactor system for a fixed set of other operating conditions. As a result, an analysis of the combined effect of susceptor temperature and total feed flowrate is performed. A measure of the nonuniformity

is defined as

$$\chi = \sqrt{\int_0^{r_w} (\delta_{bar} - f_{bar})^2 r dr}. \quad (6.11)$$

The total flowrate is decreased from 6.5 slm to 3.5 slm by increments of 1 slm and the computation of C_d with respect to susceptor temperature is performed in each case to find the optimal values of the parameters. A plot of χ as a function of total flowrate is shown in Figure 6.10. The value of χ is calculated at the optimal susceptor temperature. The results illustrate that low flowrates lead to a reduction in nonuniformity. A plot of C_d versus T_S for the case when the total flowrate is 3.5 slm is shown in Figure 6.11. Under these conditions, the optimal susceptor temperature occurs at $T_S = 1200$ K and the results for the rotated profiles are shown in Figure 6.12. These results immediately convey the improvement in uniformity towards the outer portion of the wafer. The reason for this improvement is attributable to the lower total flowrate's effect of increasing reactor residence times, pushing the peak of the deposition rate profile ($\Delta(R)$) closer to the nearest uniformity producing profile (f).

The optimization studies up to this point were performed using the simple 1D model. In order to validate the accuracy of these results, detailed simulations were carried out for three sets of operating conditions i) $T_S = 1373K$, Total Flowrate = 6.5slm; ii) $T_S = 1312K$, Total Flowrate = 6.5slm; and iii) $T_S = 1200K$, Total Flowrate = 3.5slm. Film thickness profiles along the susceptor are shown in Figure 6.13 for these three cases. The results immediately highlight similar trends when compared to the deposition profiles in Figures 6.7, 6.9, and 6.12. The rotated

optimal profiles generated from the detailed simulation are given in Figure 6.14 and clearly illustrate the improvement in uniformity.

Figure 6.1: A vertical cross-sectional view of gallium nitride radial-flow planetary reactor with a 2-flow gas inlet design (top); and the physical domain (bottom).

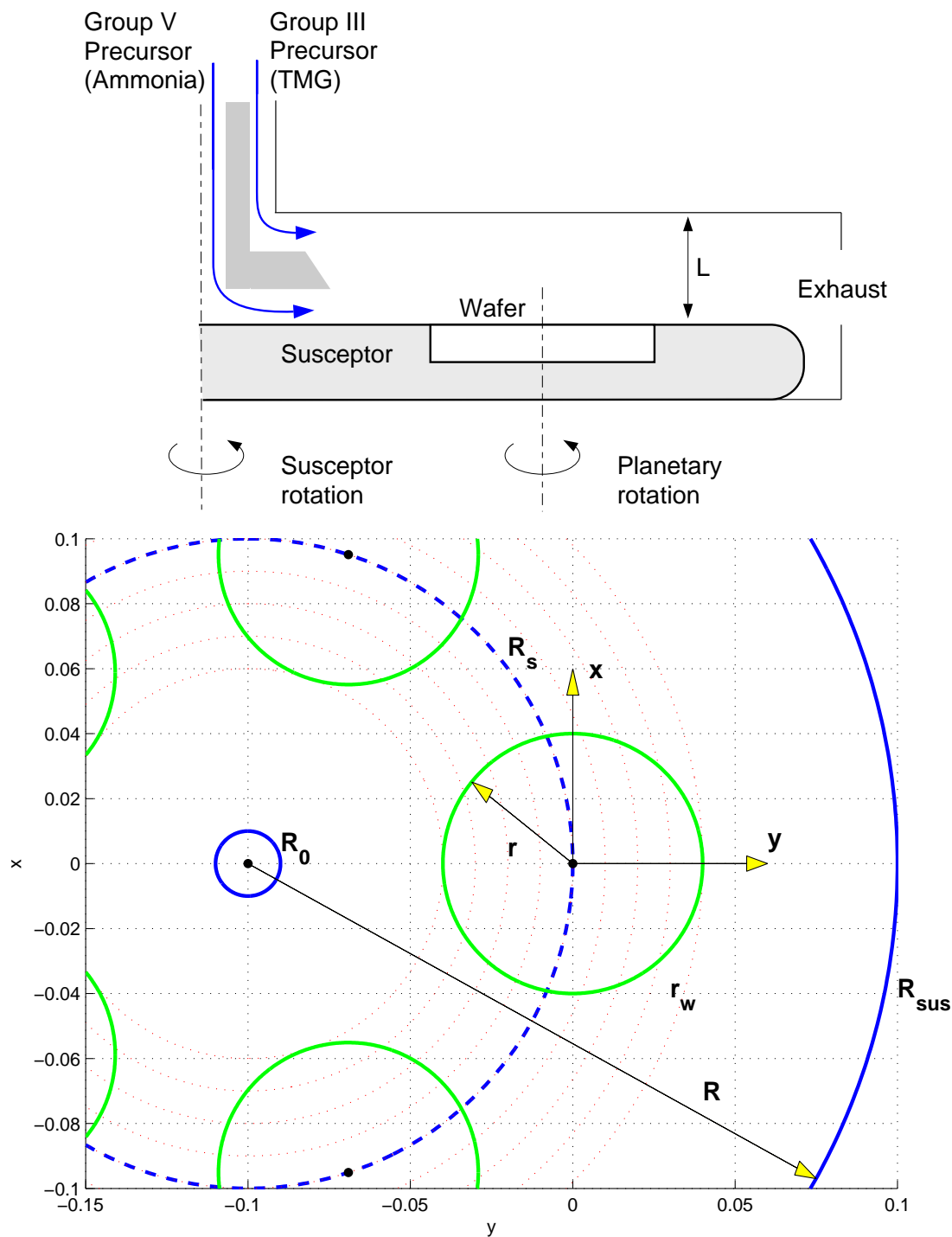


Figure 6.2: Computational grid used for 2D simulation for a gallium nitride radial-flow planetary reactor.

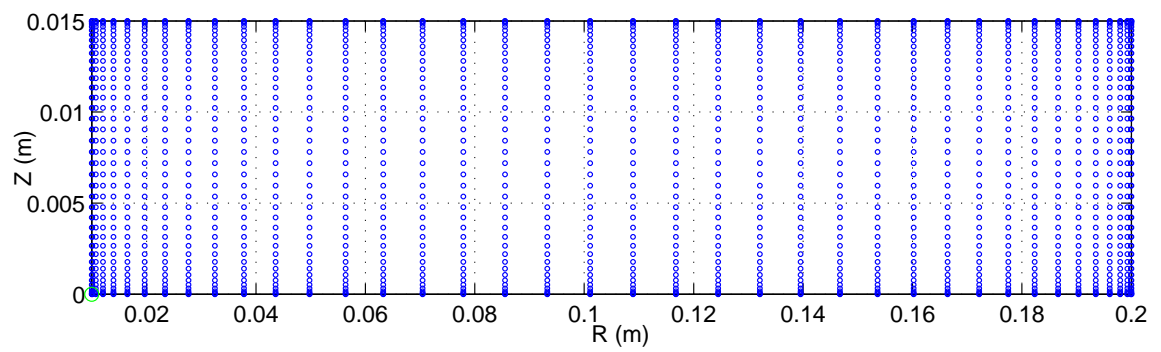


Figure 6.3: 2-dimensional simulation results for gas temperature and velocity.

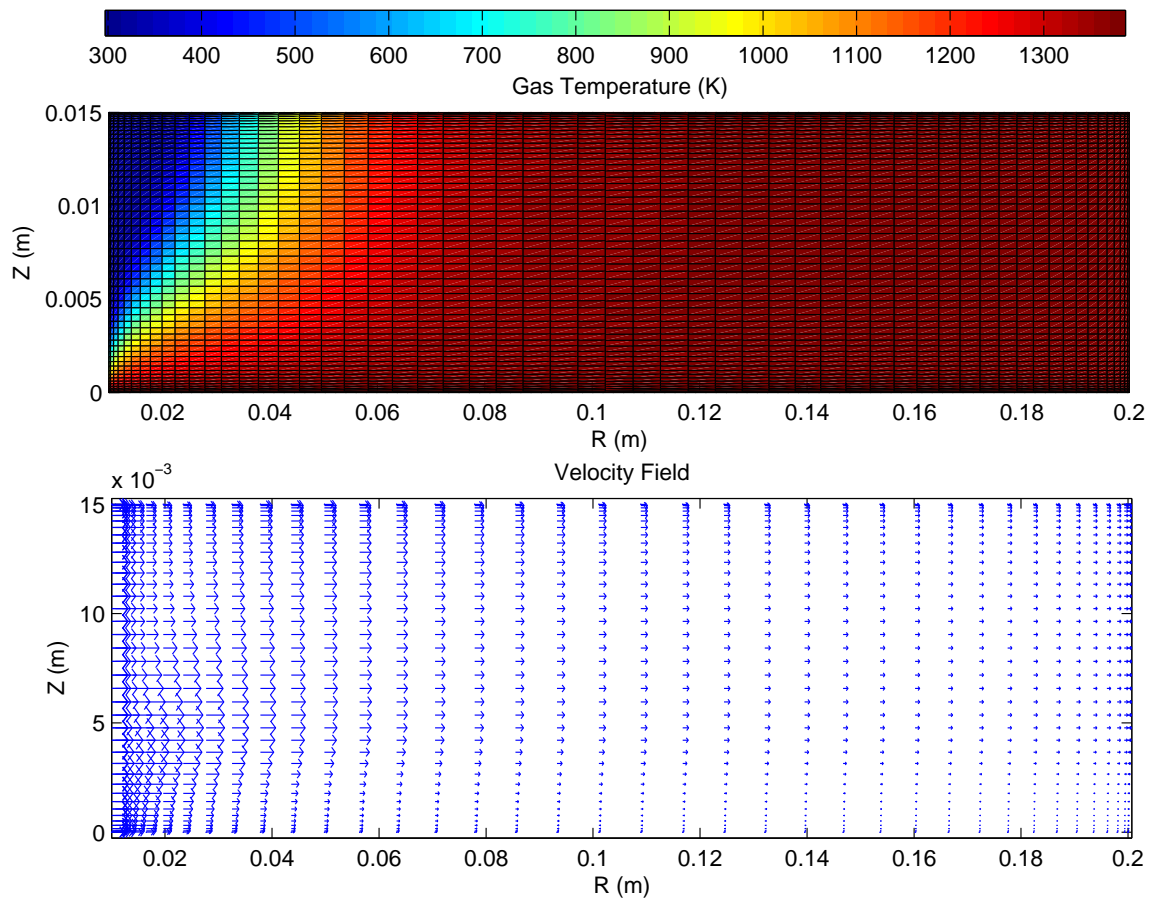


Figure 6.4: 2-dimensional simulation results for individual chemical species.

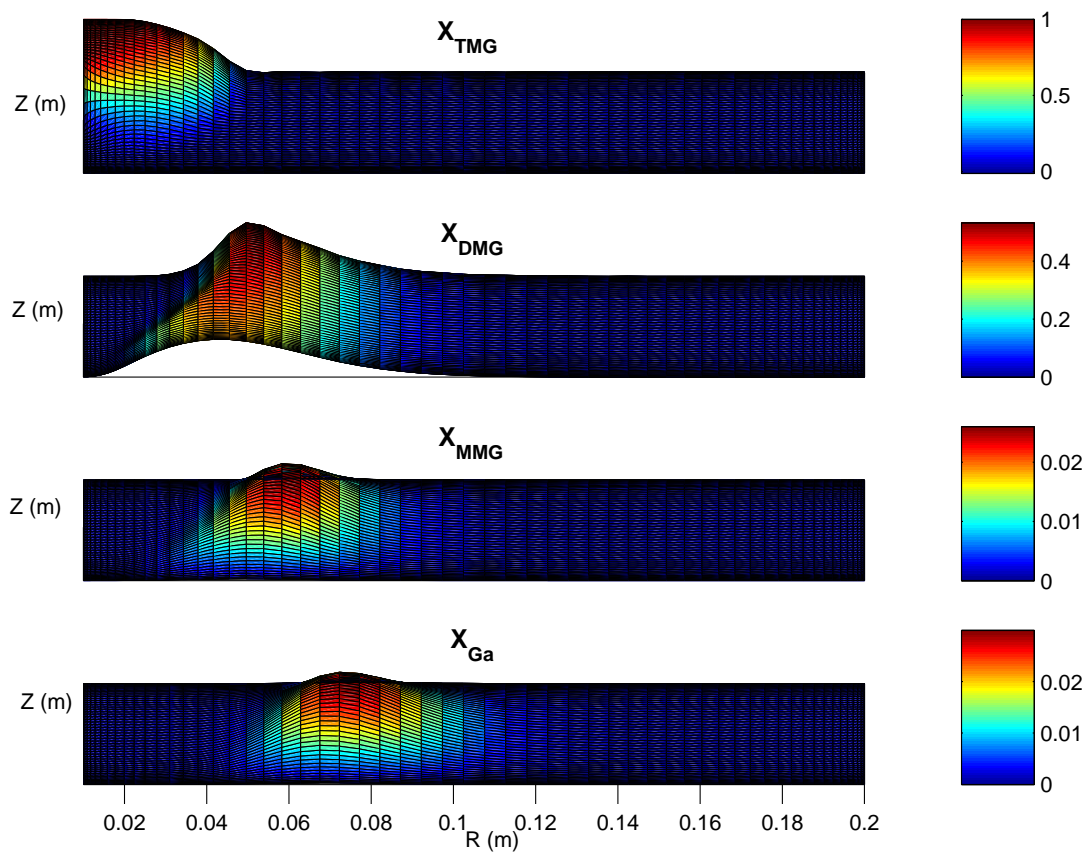


Figure 6.5: Simulation results for gas temperature distribution inside radial-flow planetary reactor: $T_S = 1373$ K; $T_0 = 300$ K. Location of wafer: $0.06m \leq R \leq 0.14m$.

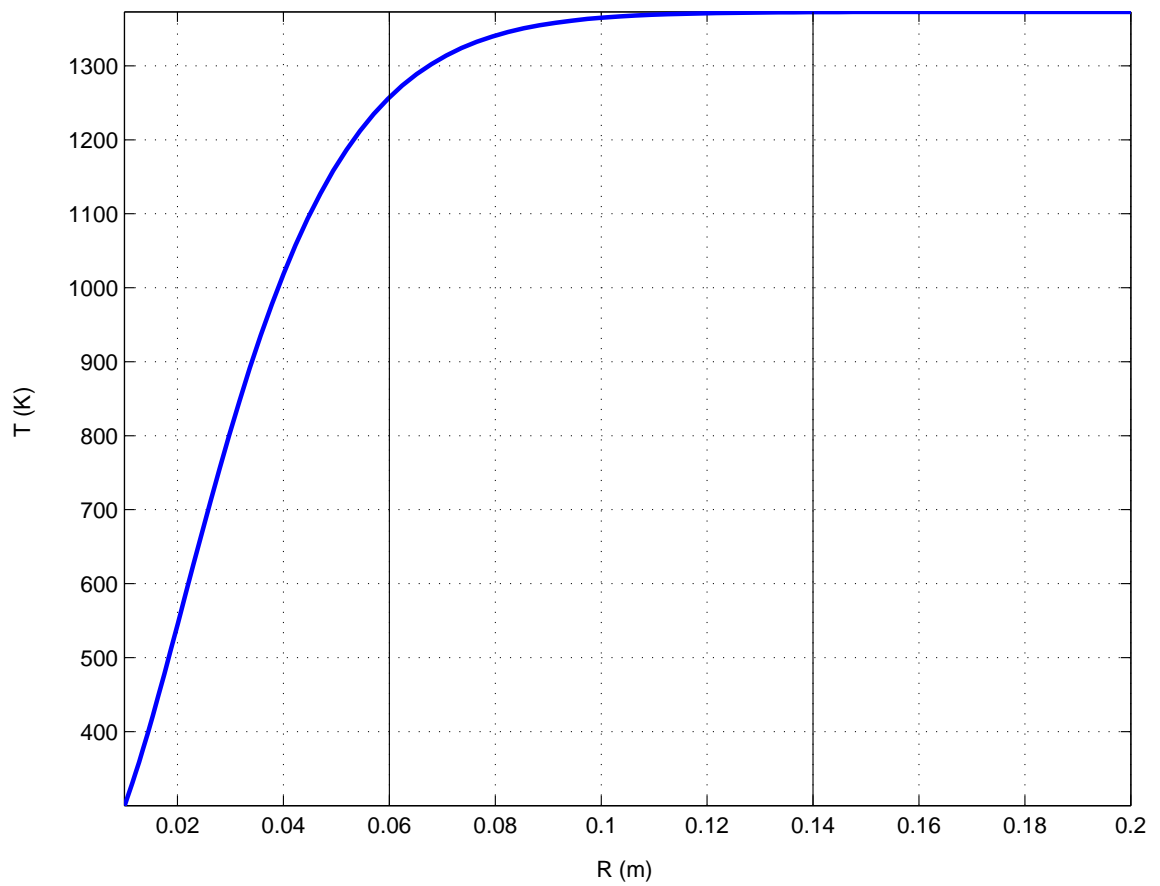


Figure 6.6: Simulation results for individual chemical species (normalized): $T_S = 1373$ K; $x_{TMG}^0 = 1.0$; Location of wafer: $0.06m \leq R \leq 0.14m$.

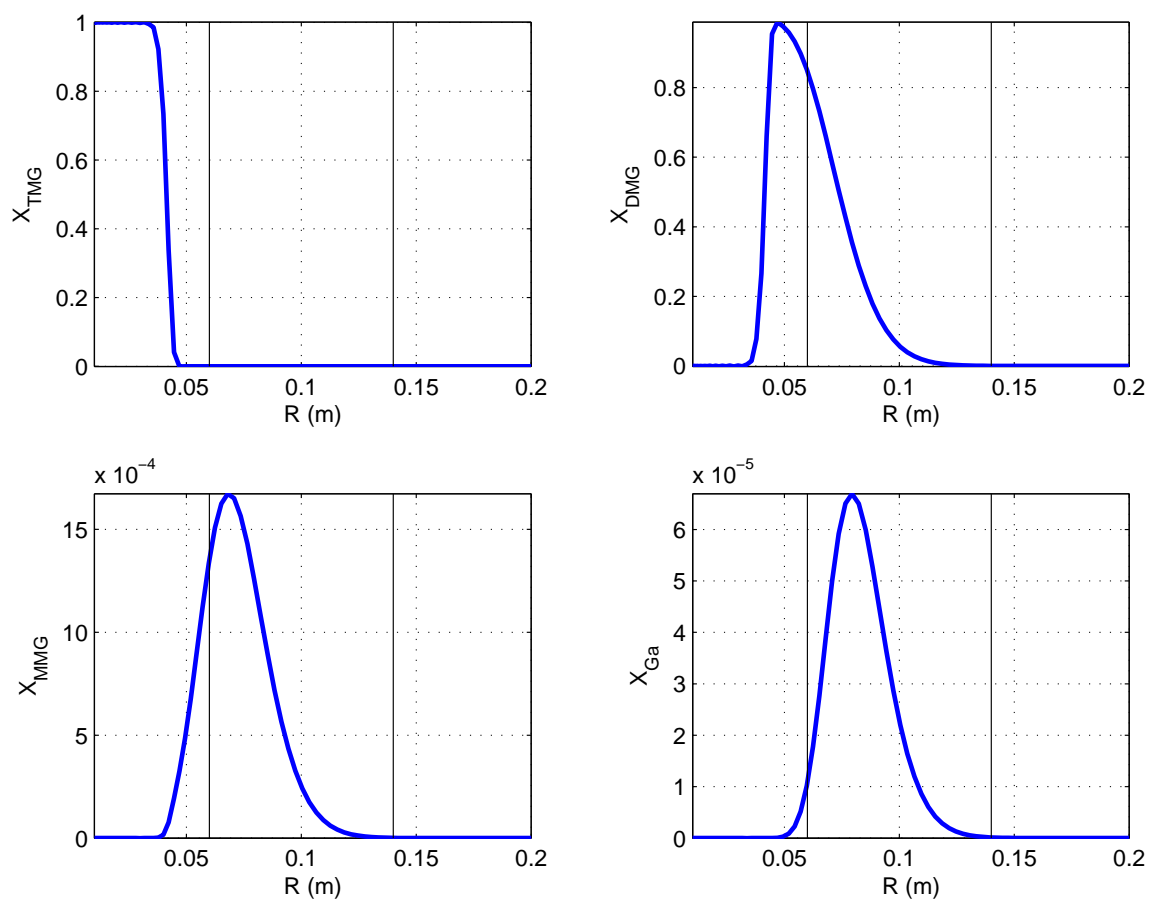


Figure 6.7: Wafer deposition profile Δ , the resulting profile upon rotation $\bar{\delta}$ and the nearest uniformity generating profile f and its profile upon rotation \bar{f} for $T_S = 1373$ K and total flowrate = 6.5 slm. Wafers are located in non-shaded region.

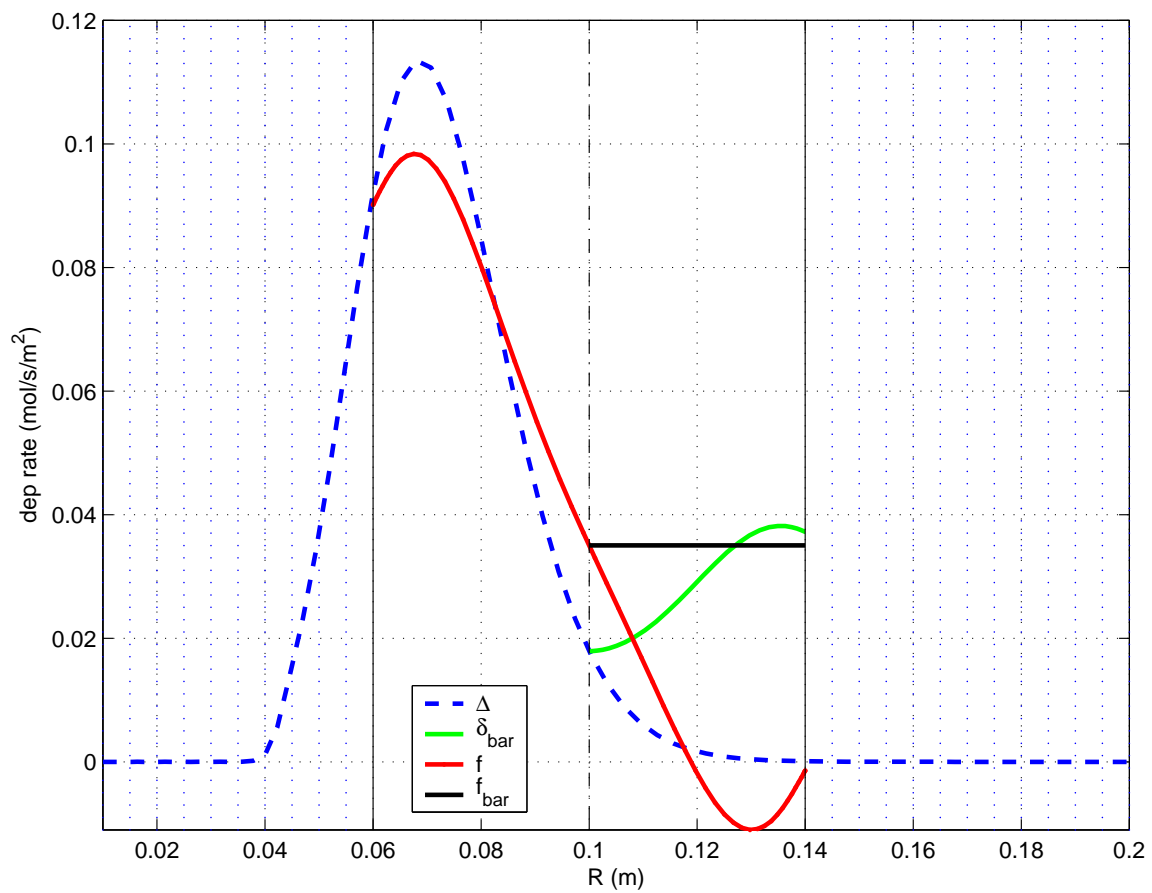


Figure 6.8: Uniformity criterion C_d value as a function of susceptor temperature (total flowrate = 6.5 slm).

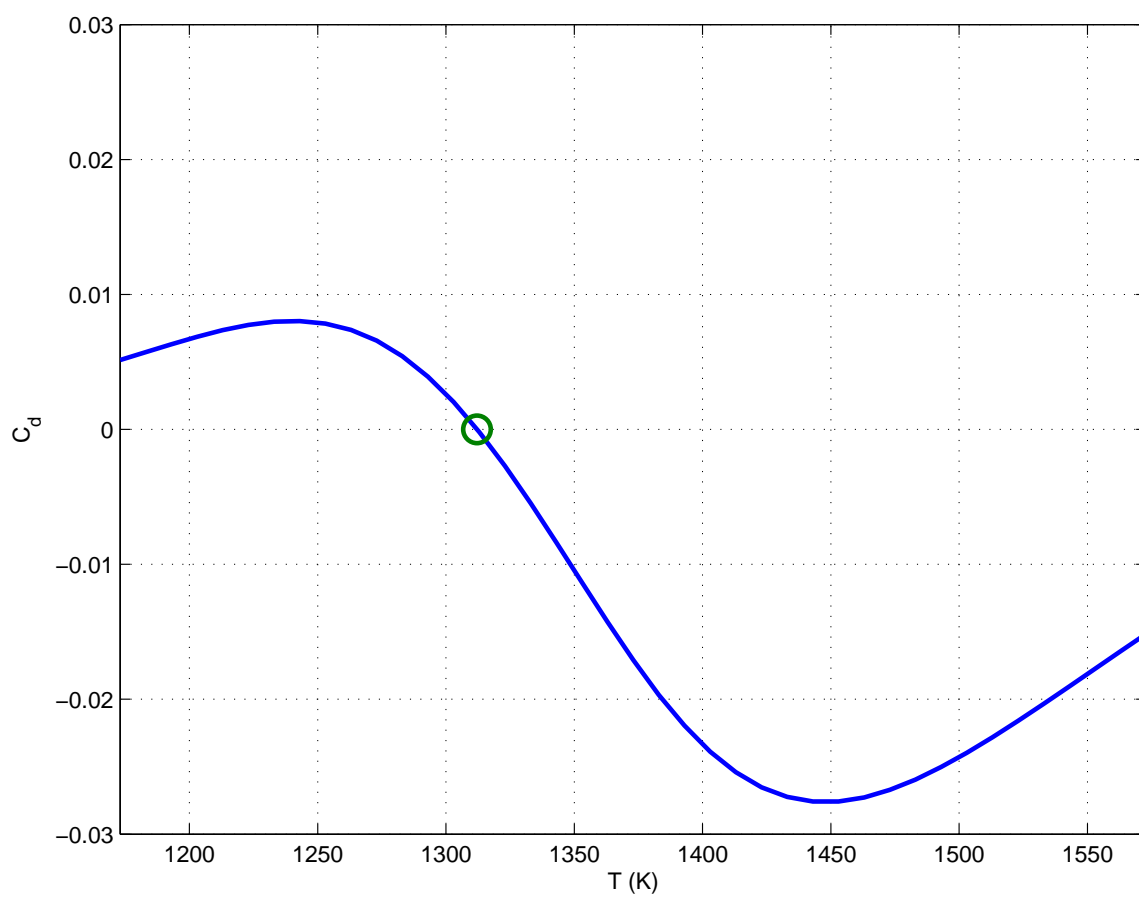


Figure 6.9: Results for optimal susceptor temperature of $T_S = 1312$ K (total flowrate = 6.5 slm).

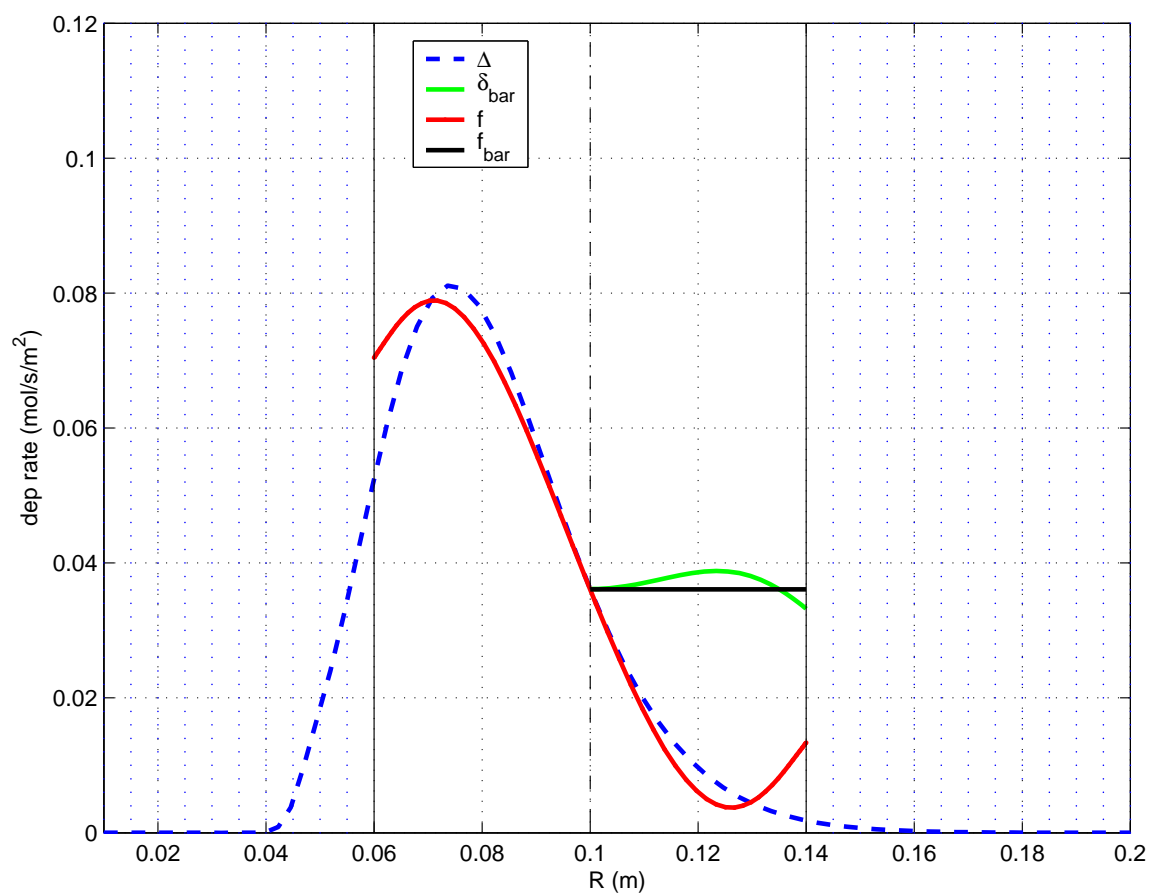


Figure 6.10: Measure of nonuniformity, χ , at the $C_d = 0$ condition as a function of total flowrate.

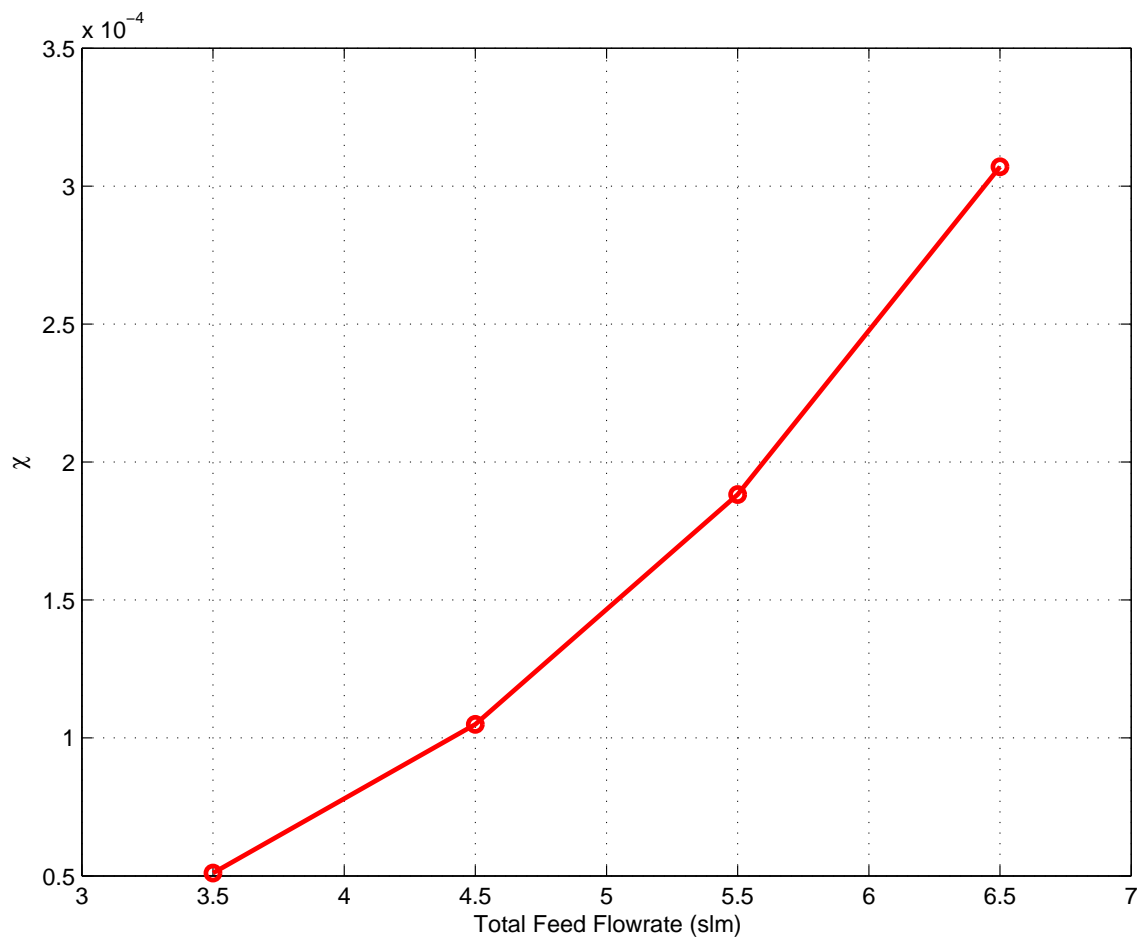


Figure 6.11: Uniformity criterion C_d value as a function of susceptor temperature (total flowrate = 3.5 slm).

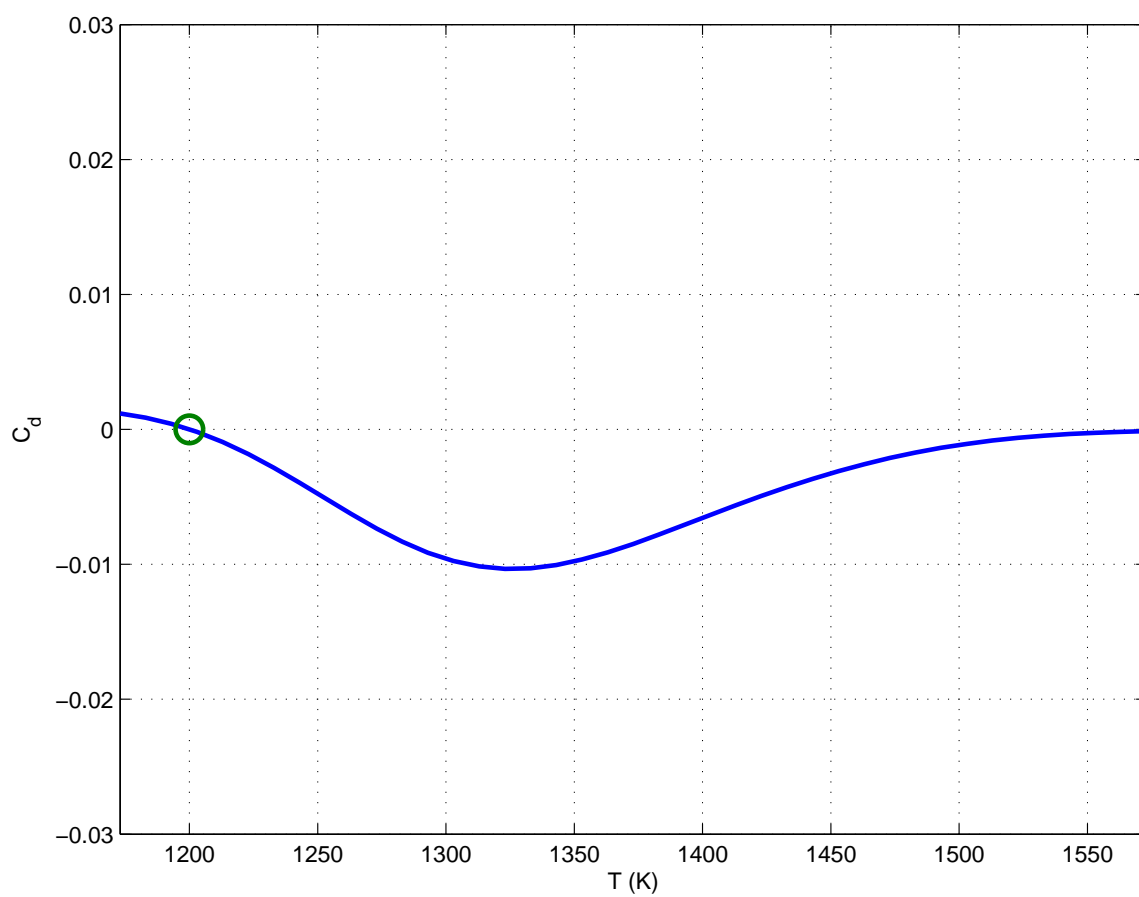


Figure 6.12: Results for optimal susceptor temperature of $T_S = 1200$ K (total flowrate = 3.5 slm).

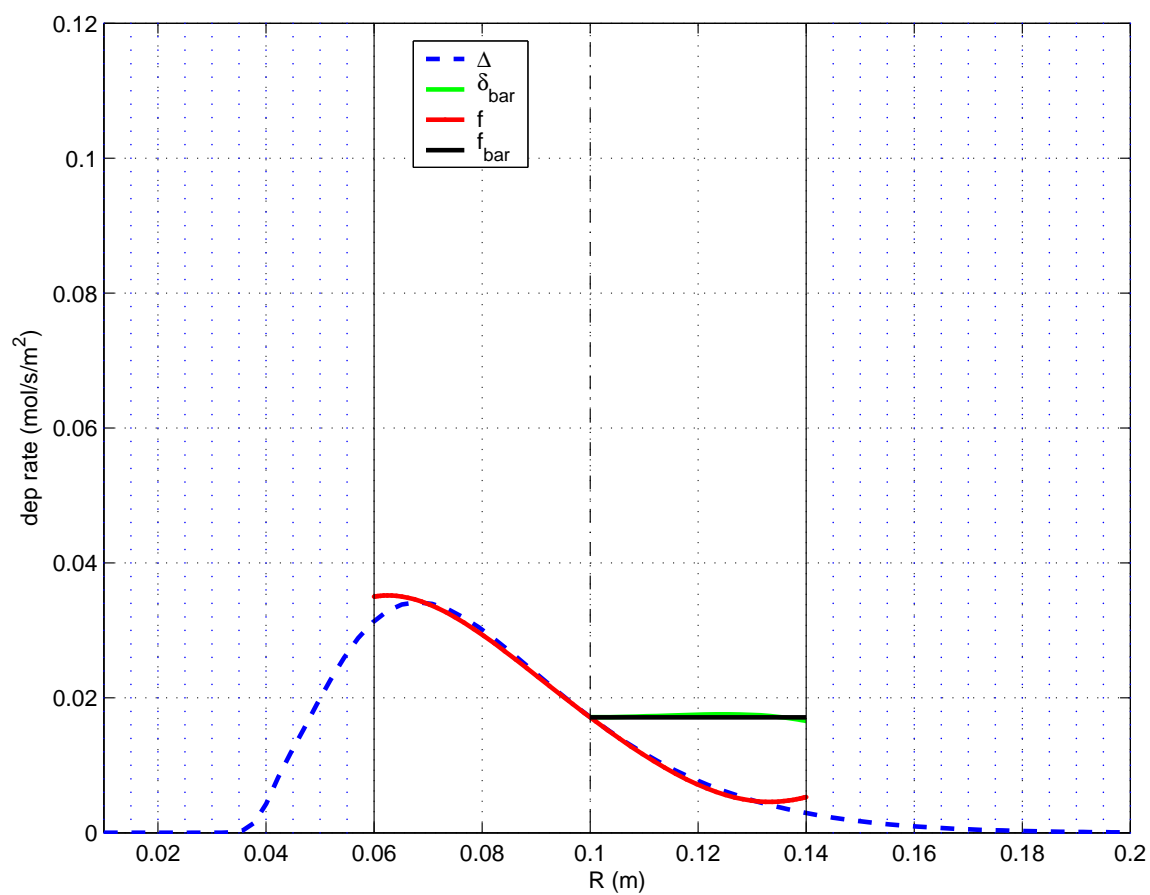


Figure 6.13: Wafer deposition profiles for three sets of operating conditions computed by the detailed 2D transport and reaction-kinetic model.

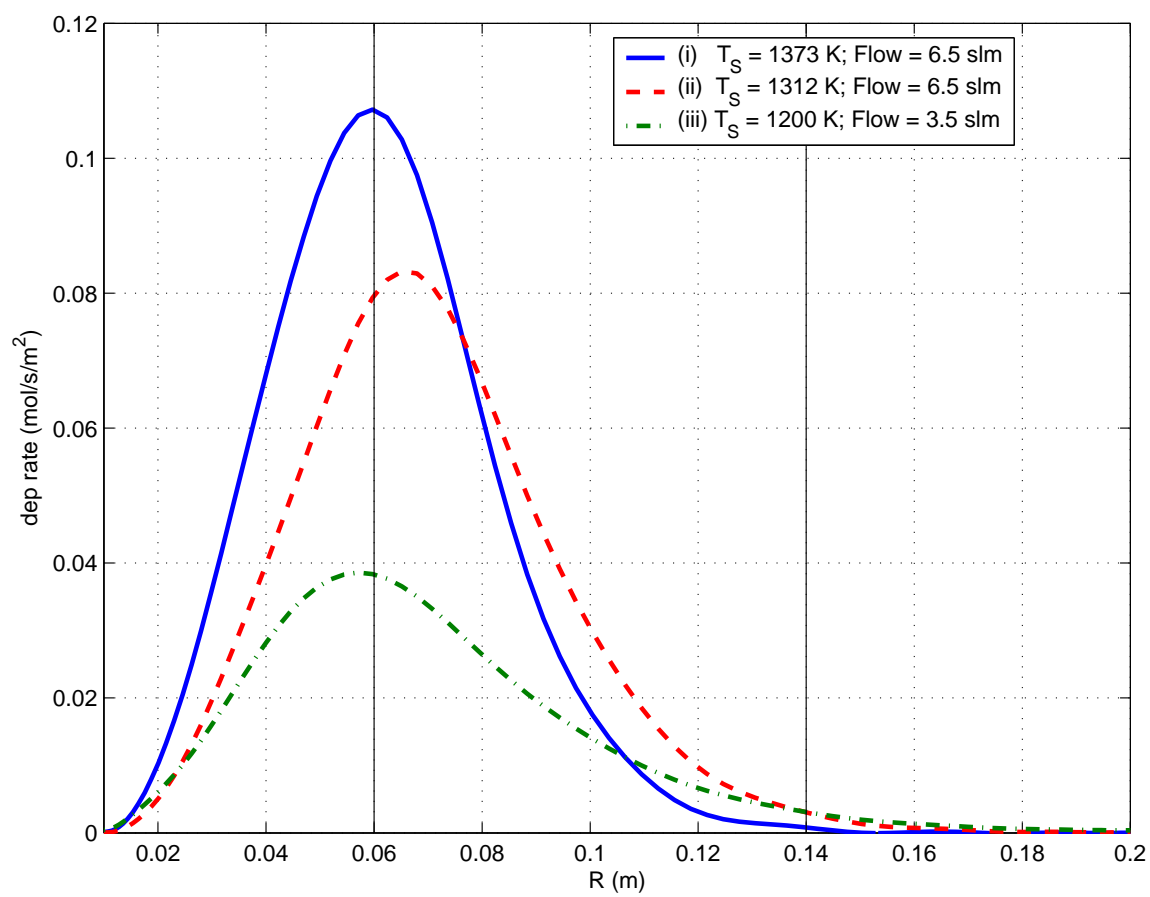
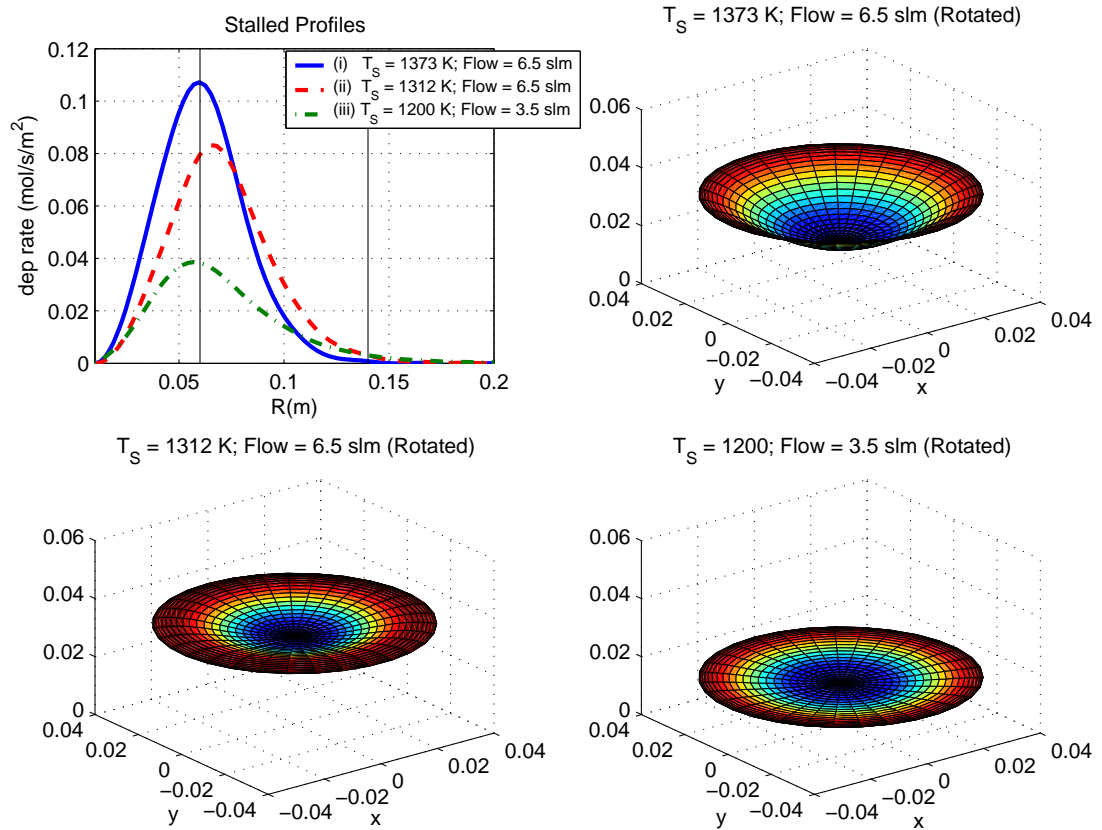


Figure 6.14: Rotated full wafer plots for three sets of operating conditions.



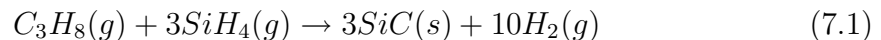
Chapter 7

IMPLEMENTATION OF "NUPP" FOR FILM UNIFORMITY CONTROL IN A PLANETARY SiC CVD REACTOR SYSTEM

In recent years, improvements in the growth of SiC by CVD have been studied by both experimental and computational methods. Common precursors used to grow SiC are silane (SiH_4) and propane (C_3H_8), where hydrogen is the carrier gas. Physically based models that take into account heat, momentum, and mass transfer effects within CVD reactors have been detailed in several papers [56, 57, 58]. Such models are routinely used to optimize the design and operating parameters to produce films of SiC with a spatially uniform thickness.

7.1 Planetary SiC CVD Reactor Model Development

A vertical cross-sectional view of a radial-flow planetary reactor system along with its physical domain, $R_0 \leq R \leq R_{sus}$, is shown in Figure 7.1. The precursors, SiH_4 (silane) and C_3H_8 (propane), and carrier gas species, H_2 , are injected into the center of the reactor through a 2-flow gas inlet design and flow outwards over wafers arranged in circular patterns over the susceptor leading to SiC growth:



In these reactors, the wafers are placed on rotating satellites which in turn rotate around the central axis of the susceptor plate; in this reactor system, susceptor and satellite rotation rate is sufficiently low as to not disturb gas flow over the susceptor and wafers. The radial flow geometry combined with the substrate planetary motion mechanism is commonly employed to produce uniform deposition profiles on the wafers [54, 55]. It should be noted that reactors of this type can be run with both rotating and stalled (non-rotating) wafers.

A detailed two-dimensional transport and reaction-kinetic model is developed in this thesis for a SiC reactor system similar in form to the one developed in chapter 6 for gallium nitride. This transport and reaction-kinetic model is based on fundamental equations accounting for momentum, heat, and mass-transfer within a compressible gas with temperature-dependent physical properties. Because the mixture of reactants and products in the carrier gas (H_2) is dilute, it is valid to neglect the heat of reaction along with any expansion or contraction of the mixture due to chemical reactions. Moreover, the precursor species and all products formed from subsequent reactions between the precursors exist in low concentration relative to the carrier gas. Therefore, multicomponent diffusion need not be considered and binary diffusion coefficients of the reactants and products in the carrier gas (H_2) are utilized. The continuity equation, equation of motion, equation of energy, and mass balances of each chemical species for temperature-dependent density (ρ), viscosity (μ), heat capacity (C_p), and thermal conductivity (k) are expressed as the following

Mass Continuity:

$$\nabla \cdot (\rho v) = 0 \tag{7.2}$$

Momentum Balance:

$$\rho \frac{Dv}{Dt} = -\nabla P - \nabla \cdot \tau + \rho g \quad (7.3)$$

subject to boundary conditions

$$\begin{aligned} v_R &= v_0 & P &= P_T & \text{at} & R = R_0 \\ \frac{1}{R} \frac{\partial}{\partial R} (\rho R v_R) &= 0 & \frac{\partial P}{\partial R} &= 0 & \text{at} & R = R_{sus} \\ v_R &= 0 & \frac{\partial P}{\partial Z} &= 0 & \text{at} & Z = 0 \\ v_R &= 0 & \frac{\partial P}{\partial Z} &= 0 & \text{at} & Z = L \end{aligned}$$

Energy Balance:

$$\rho C_p (v \cdot \nabla T) = \nabla \cdot (k \nabla T) \quad (7.4)$$

subject to boundary conditions

$$\begin{aligned} v_R \rho C_p (T_0 - T) &= -k \frac{\partial T}{\partial R} & \text{at} & R = R_0 \\ \frac{\partial T}{\partial R} &= 0 & \text{at} & R = R_{sus} \\ T &= T_S & \text{at} & Z = 0 \\ \frac{\partial T}{\partial Z} &= 0 & \text{at} & Z = L \end{aligned}$$

Mass Balances:

$$\nabla \cdot (c x_i v) = \nabla \cdot [c D_i (\nabla x_i)] - R_i^G \quad (7.5)$$

subject to boundary conditions

$$\begin{aligned} x_i c v_R &= x_i^0 c v_R - c D_i \frac{\partial x_i}{\partial R} & \text{at} & R = R_0 \\ \frac{\partial x_i}{\partial R} &= 0 & \text{at} & R = R_{sus} \\ c D_i \frac{\partial x_i}{\partial Z} &= R_i^S & \text{at} & Z = 0 \\ -c D_i \frac{\partial x_i}{\partial Z} &= R_i^S & \text{at} & Z = L \end{aligned}$$

The term $(\frac{Dv}{Dt})$ in equation 7.3 represents the substantial time derivative.

In addition, the components of the viscous stress tensor (τ) in equation 7.3 for Newtonian fluids in cylindrical coordinates are:

$$\tau_{R R} = -\mu[2\frac{\partial v_R}{\partial R} - \frac{2}{3}(\nabla \cdot v)]$$

$$\tau_{\theta\theta} = -\mu[2\frac{v_R}{R} - \frac{2}{3}(\nabla \cdot v)]$$

$$\tau_{R Z} = -\mu[\frac{\partial v_R}{\partial Z}]$$

These equations in conjunction with their appropriate boundary conditions are used to compute the velocity (v), pressure (P), temperature (T), and species mole fraction (x_i) distributions for this system. The computational domain is shown in Figure 7.2. The computational domain extends from $R_0 \leq R \leq R_{sus}$ and $0 \leq Z \leq L$; where R_0 denotes the radius of the central feed tube and L is the spacing between the wafer top surface and the reactor roof which is assumed to be perfectly insulating. The notation used in (7.2-7.5) is the following: inlet gas velocity (v_0); total reactor pressure (P_T); inlet gas temperature (T_0); susceptor temperature (T_S); inlet mole fraction of species i (x_i^0); total concentration of the gas ($c = P_T/R_{gas}/T$ for an ideal gas where R_{gas} corresponds to the ideal gas constant); binary diffusion coefficients of species i (D_i); rate of generation of species i per unit volume due to gas phase reactions (R_i^G); and the rate of generation of species i per unit area due to surface phase reactions (R_i^S).

The system of non-linear partial differential equations, written in two coordinates (R and Z), were discretized by collocation and subsequently solved by implementing the Newton-Raphson method as described in chapter 2. The flow and heat transfer equations were solved first to compute the gas temperature and velocity distributions. The mass transfer and kinetic problem was subsequently solved on the same grid to compute the species distribution.

Representative simulation results describing gas temperature and velocity distributions are shown in Figure 7.3. The results indicate rapid gas heating inside the reactor system. The increase in gas velocity observed shortly after the inlet is related to the rapid expansion of the gas due to density decrease associated with gas heating.

A reaction mechanism describing gas-phase decomposition of SiH_4 and C_3H_8 is used for the reaction-kinetic model developed in this thesis. Rate parameters for both silane and propane decomposition are taken from [58] and given in Table 7.1. SiC is formed on the surface by equal amounts of silicon and carbon atoms. Therefore, the growth rate is computed by examining the individual deposition rates of silicon and carbon. In order to maintain a stoichiometric deposition on the growing surface, the smaller of the two deposition rates is used. This technique is commonly employed by other research groups [56] as well as the simulations performed in this thesis. The products generated from the breakdown of silane and propane govern the growth rate, and accordingly, the film growth rate is determined by the flux of these species at the growth surface. The flux of these species to the surface is derived from the kinetic theory of gases and governed by the Hertz-

Knudsen equation [40]:

$$F_i = \frac{P}{(2\pi M_i R_{gas} T)^{0.5}} \cdot x_i \quad (7.6)$$

Here F_i represents the flux of species i (mol/area/time), P the total pressure, M_i is the molecular weight of species i , R_{gas} is the ideal gas constant, T is the temperature, and x_i corresponds to the mole fraction of species i in the gas phase above the surface. Sticking probabilities for the reacting species are taken from [56] and given in Table 7.2.

Representative simulation results for species mole fraction distributions from silane decomposition are shown in Figure 7.4. These profiles correspond to thermal decomposition of silane into SiH_2 and Si . This SiC model was tested against experimental data taken from multiple stalled wafer runs and the results were in good agreement (Figure 7.5). It is evident from the results that an increase in flowrate reduces the growth rate near the wafer leading edge and raises the growth rate towards the wafer trailing edge. This is directly related to the decomposition chemistry taking place combined with a reduction in reactor residence times. Moreover, Figure 7.5 shows that the crossing point where the growth rate profiles intersect is seen in model predictions and observed experimentally. Finally, it should be noted that no adjustable parameters have been included in this model.

7.2 Run-to-run Film Uniformity Control

The reactor system illustrated in Figure 7.1 can process 5 wafers in a single deposition run; to implement a run-to-run control algorithm based on minimizing

(5.1), the reactor system would be operated with 4 of the 5 production wafers undergoing rotation and a single sacrificial stalled wafer. After each deposition run, the stalled wafer desired film property would be measured and projected onto the β_n modes to obtain the NUPP and (5.1). The reactor deposition model then would be used to determine a search direction based on minimizing the uniformity criteria, and the reactor operating conditions would be adjusted accordingly. A stalled wafer is processed again only when the controlled film property falls out of specification or a major process change is implemented (e.g., process recipe adjustment or physical reactor modifications).

7.2.1 An industrial application

A commercial, multi-wafer planetary reactor system is used for SiC CVD by the Northrop Grumman Corporation. Film growth rates have been observed to be highly sensitive to changing operating conditions. This is not surprising given the order-of-magnitude difference in measured growth rate across the stalled wafer under normal operating conditions. In this section, capabilities of a NUPP-based run-to-run control strategy to improve film uniformity across the wafer is evaluated for this system.

The growth rate for SiC is represented by $\Delta(R)$. Based on the good agreement between model and experiments shown earlier (Figure 7.5), the feasibility of a NUPP-based run-to-run control strategy was evaluated for this system. Results from an experiment with operating conditions corresponding to a susceptor temper-

ature 1600 °C, pressure = 125 mbar, Flowrate = 35 slm, SiH₄ = 170 sccm, and C₃H₈ = 70 sccm are shown in Figure 7.6. This figure shows an across wafer slice of measured deposition thickness along a chord from the wafer leading edge to the trailing edge. The growth rate, $\Delta(R)$, was then projected onto the β_n modes to compute the NUPP. From Figure 7.6, it is apparent that $\Delta(R)_{rotated}$, which is the profile that results from rotation of the current $\Delta(R)$, is not uniform. From a physical standpoint, intuition suggests increasing the flowrate as a potential means to improving uniformity relative to the original set of operating conditions; the physical reasoning is described below. Thus, the detailed 2D reactor deposition model developed in this thesis was used to minimize a uniformity criterion, U_{CR} , with respect to flowrate, keeping all other operating conditions constant, where U_{CR} is defined as

$$U_{CR} = \frac{\langle S, S \rangle}{\langle N_u, N_u \rangle} \quad (7.7)$$

This criterion is similar to (5.1), but now incorporates the mean thickness in the denominator so both uniformity and film deposition rate are factored into the objective function. The prediction from the model suggested that an improvement in uniformity is possible at higher flowrates. Similar trends are observed from two additional experimental runs shown in Figure 7.7. It is evident from Figure 7.7 that uniformity has greatly improved in these experimental runs. The reason for this improvement is attributable to the higher total flowrate's effect of reducing reactor residence times, pushing the peak of the deposition rate profile ($\Delta(R)$) closer to the nearest uniformity producing profile (N_u). Quantitative results of the uniformity criterion, U_{CR} , are tabulated in Table 7.3 and plotted in Figure 7.8 to show the im-

provement in uniformity that can be obtained through this NUPP-based run-to-run control strategy and furthermore, show that the improvement does not come at the expense of decreased film thickness.

Table 7.1: Representative gas-phase reaction scheme for decomposition of SiH_4 and C_3H_8 . Rate coefficients are in the form $k = aT^b \exp(-c/T)$.

| <i>Rxn. No</i> | <i>Reactions</i> | <i>a</i> | <i>b</i> | <i>c</i> | <i>units</i> |
|----------------|---|------------------------|----------|----------------------|---|
| G1 | $\text{SiH}_4 \rightarrow \text{SiH}_2 + \text{H}_2$ | 6.671×10^{29} | -4.795 | 3.188×10^4 | s^{-1} |
| G2 | $\text{SiH}_2 \rightarrow \text{Si} + \text{H}_2$ | 1.060×10^{14} | -0.880 | 2.261×10^4 | s^{-1} |
| G3 | $\text{SiH}_2 + \text{H}_2 \rightarrow \text{SiH}_4$ | 2.868×10^{22} | -4.203 | 6.279×10^3 | $\text{m}^3 \text{kmol}^{-1} \text{s}^{-1}$ |
| G4 | $\text{Si} + \text{H}_2 \rightarrow \text{SiH}_2$ | 1.045×10^7 | -0.388 | -2.391×10^3 | $\text{m}^3 \text{kmol}^{-1} \text{s}^{-1}$ |
| G5 | $\text{C}_3\text{H}_8 \rightarrow \text{C}_2\text{H}_5 + \text{CH}_3$ | 1.698×10^{16} | 0.000 | 4.263×10^4 | s^{-1} |

Table 7.2: Sticking probabilities of the reacting species included in the silicon carbide surface model.

| <i>Species</i> | <i>Sticking Probability</i> |
|-------------------------------|-----------------------------|
| Si | 1.0 |
| SiH ₂ | 0.7 |
| C ₂ H ₅ | 0.03 |
| CH ₃ | 0.01 |

Table 7.3: Uniformity criterion for run-to-run control in SiC reactor.

| <i>Run no.</i> | <i>Flowrate (slm)</i> | U_{CR} | Mean Thickness ($\mu\text{m/hr}$) |
|----------------|-----------------------|----------|-------------------------------------|
| 1 | 35 | 0.0183 | 2.2614 |
| 2 | 40 | 0.0147 | 2.3576 |
| 3 | 50 | 0.0015 | 2.8056 |

Figure 7.1: A vertical cross-sectional view of silicon carbide radial-flow planetary reactor with a 2-flow gas inlet design (top); and the physical domain (bottom).

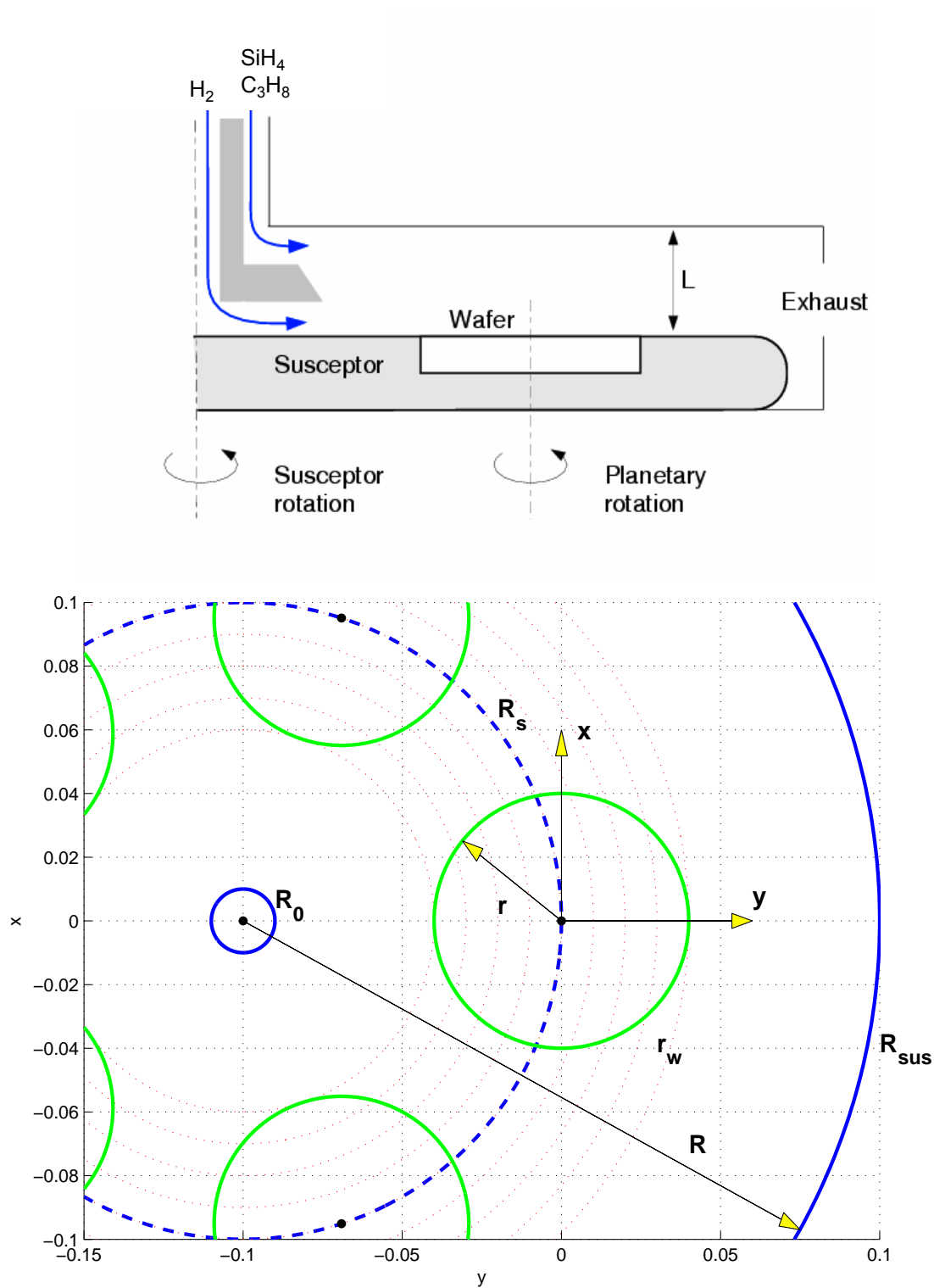


Figure 7.2: Computational grid used for 2D simulation for a silicon carbide radial-flow planetary reactor.

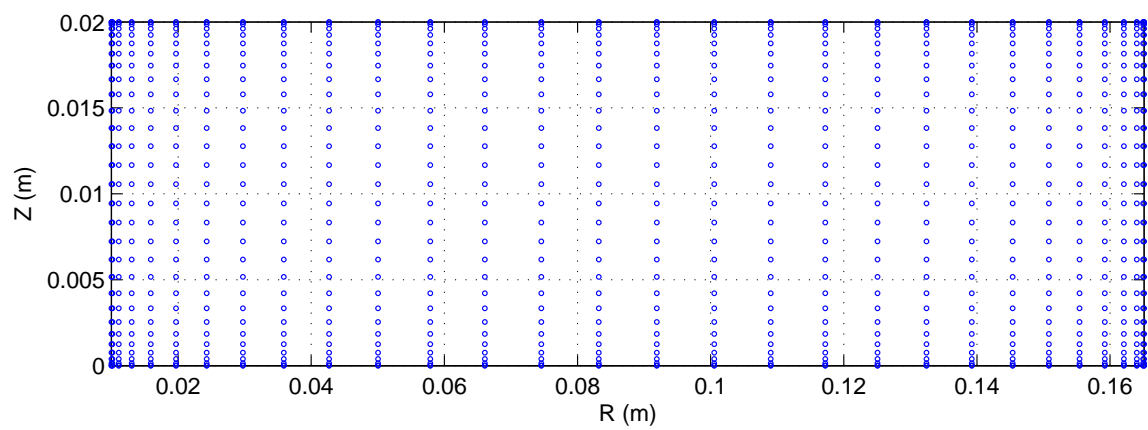


Figure 7.3: 2-dimensional simulation results for gas temperature and velocity.

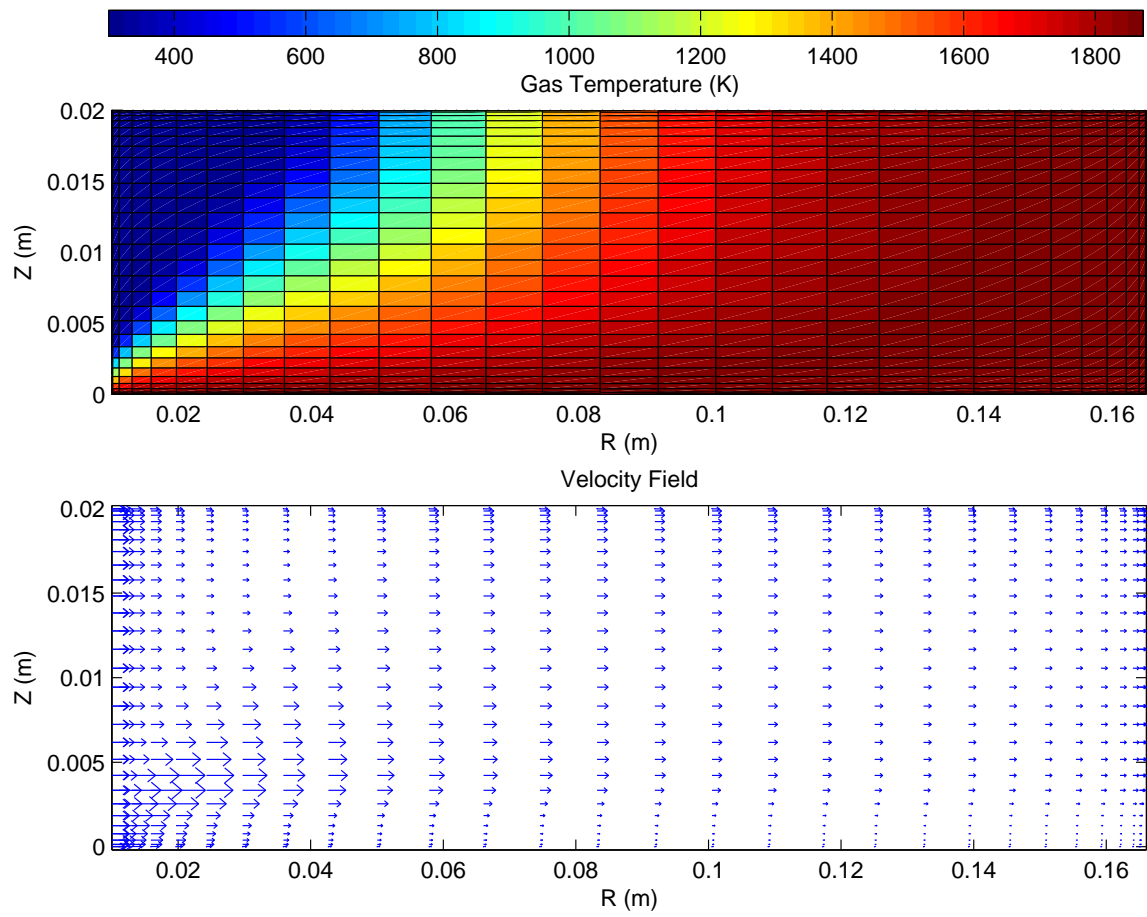


Figure 7.4: 2-dimensional simulation results for individual chemical species.

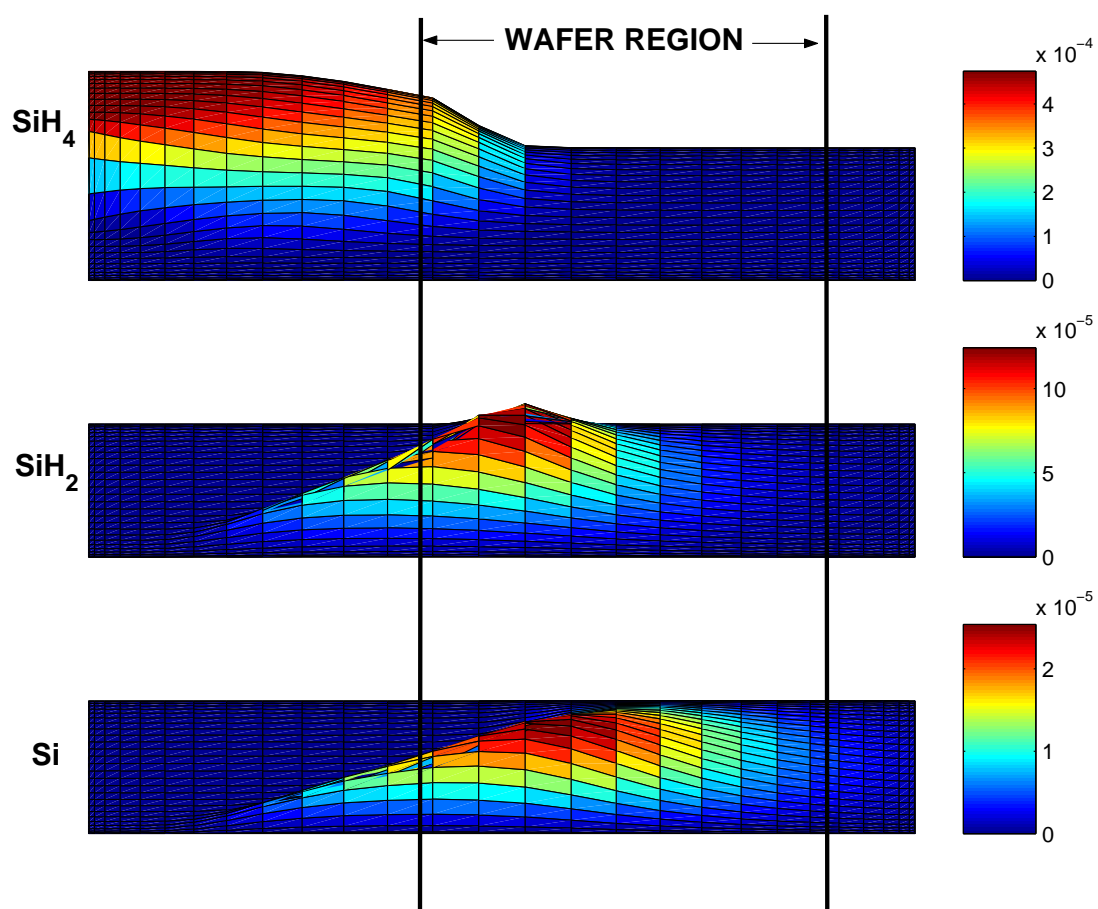


Figure 7.5: Comparison of growth rate for simulation and experiments where the only operating parameter changing is flowrate.

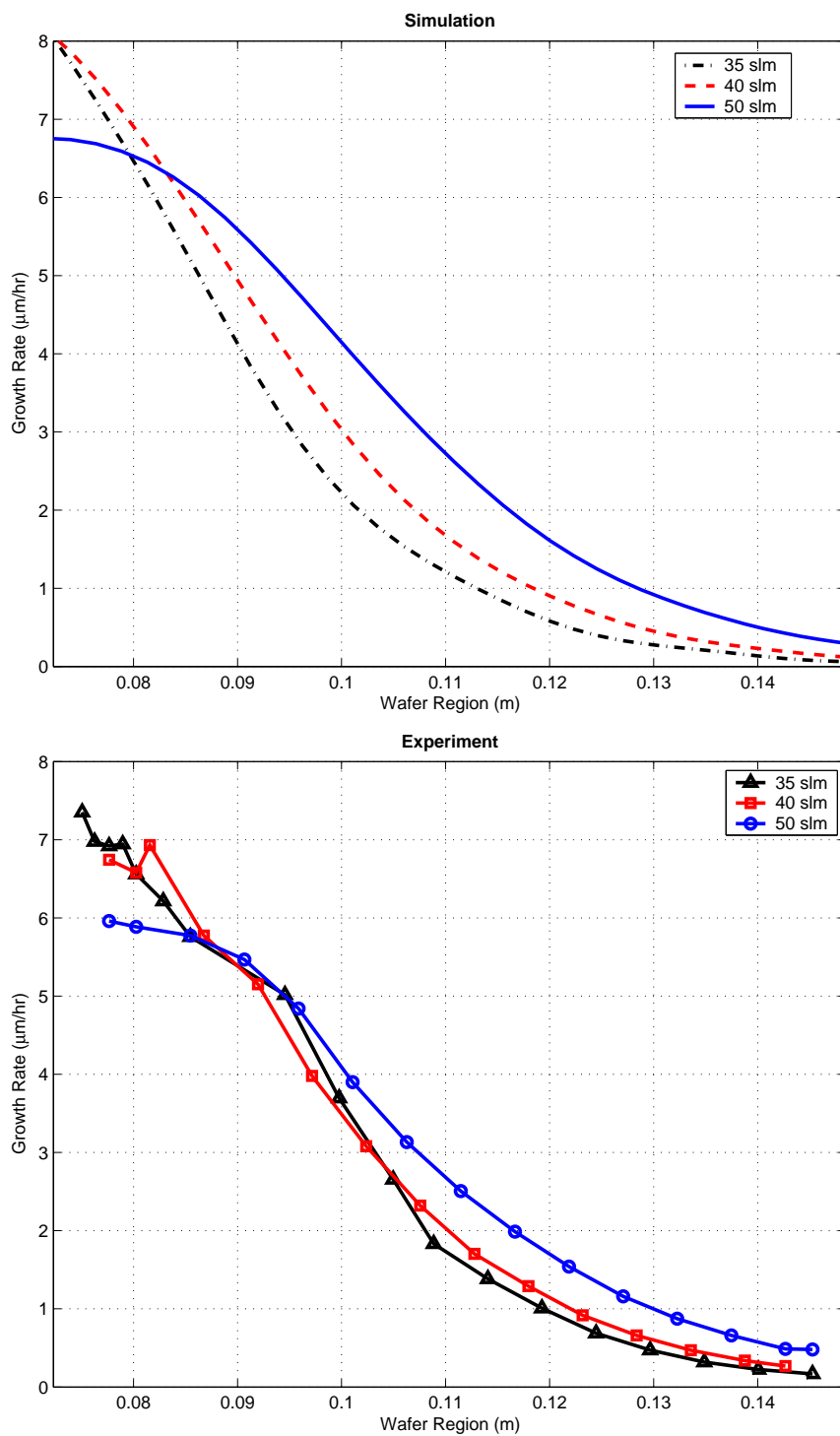


Figure 7.6: Calculation of the NUPP from a stalled wafer experiment for SiC CVD:
 Flowrate = 35 slm; susceptor temperature = 1600 °C; Pressure = 125 mbar; SiH₄
 = 170 sccm; C₃H₈ = 70 sccm.

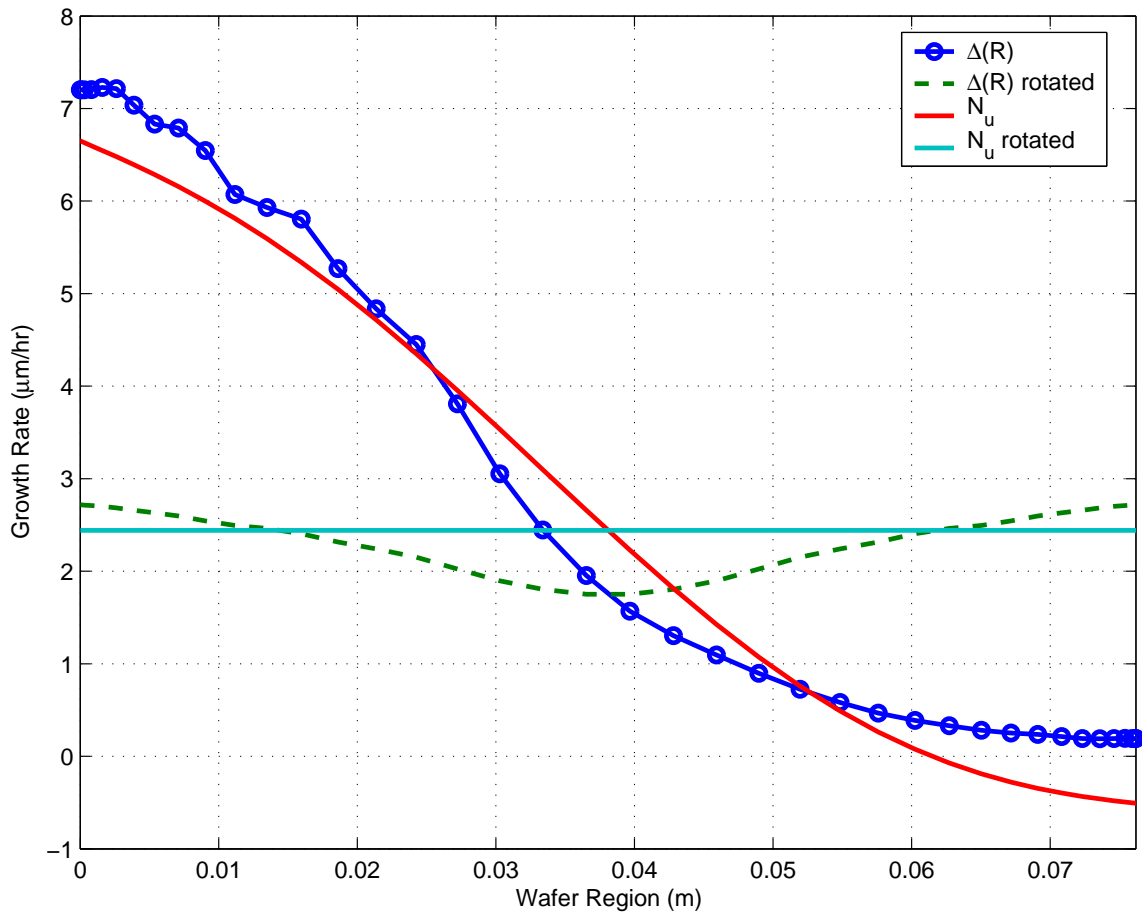


Figure 7.7: Calculation of the NUPP from stalled wafer experiments for SiC CVD: Flowrate = 40 slm (top); Flowrate = 50 slm (bottom). All other operating conditions remain constant: susceptor temperature = 1600 °C; Pressure = 125 mbar; SiH₄ = 170 sccm; C₃H₈ = 70 sccm.

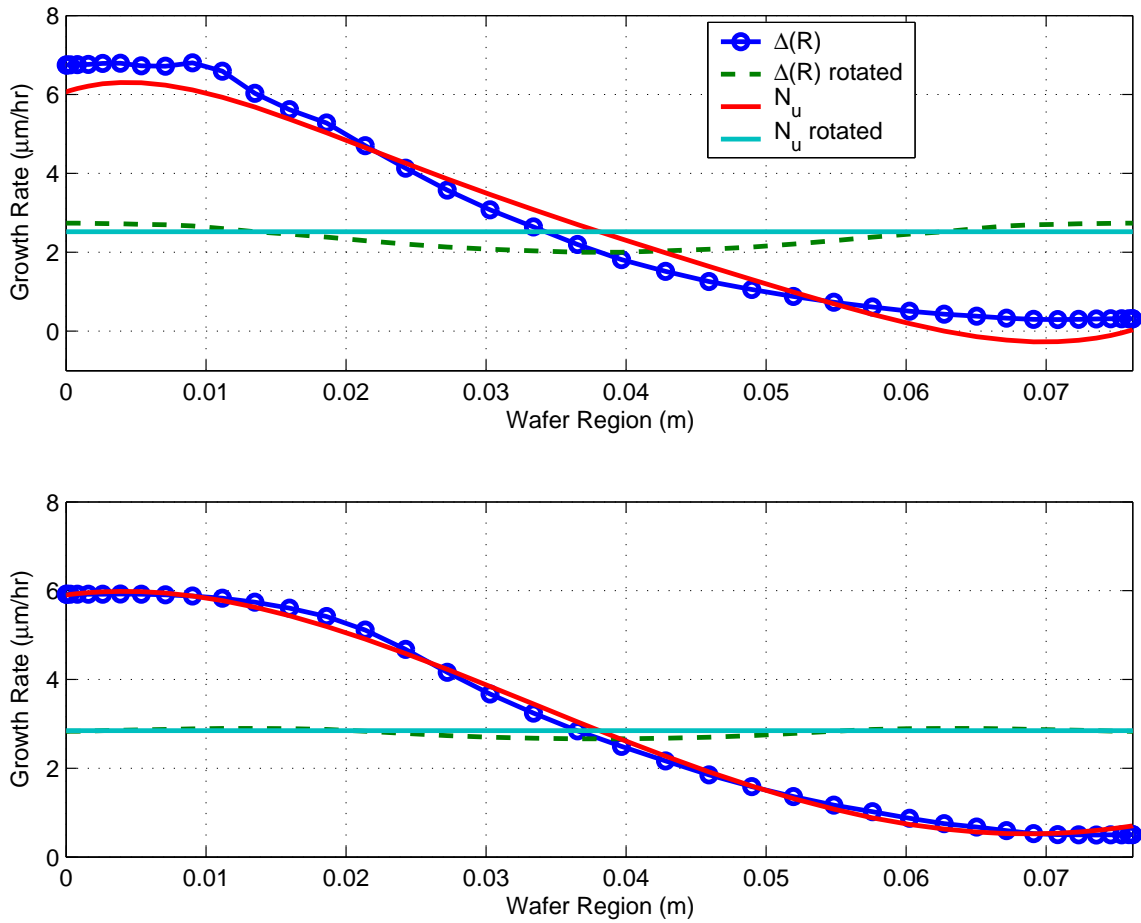
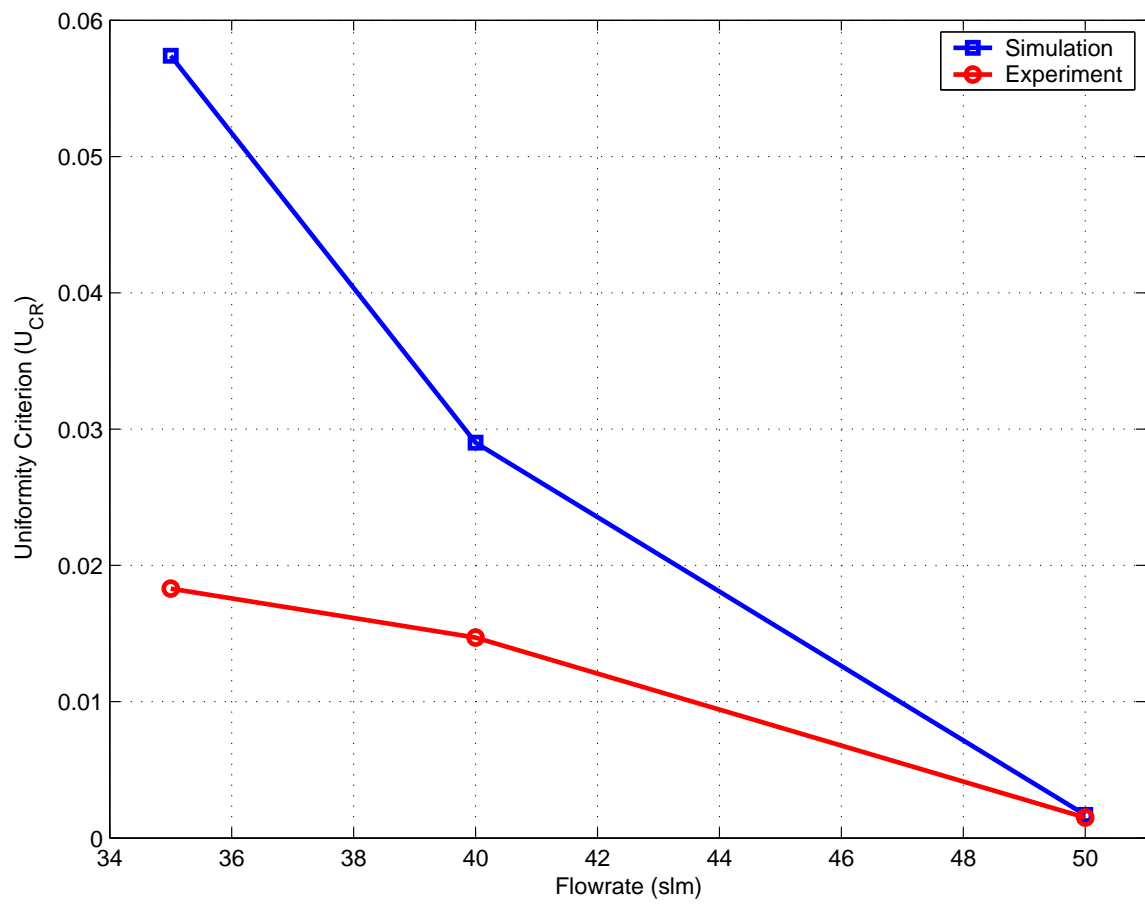


Figure 7.8: Uniformity criterion (U_{CR}) as a function of flowrate from model and experiment.



Chapter 8

CONCLUSIONS

8.1 Validating Gallium Nitride Growth Chemistry

Gallium nitride growth chemistry can be characterized as having two competing reaction pathways. The intricate adduct formation pathway produces high molecular weight adduct species which are believed to ultimately breakdown into large amounts of GaN and methane molecules. On the other hand, the thermal decomposition pathway of TMG is relatively well known with products being low molecular weight sub-alkyls. Nonetheless, a clear consensus on all aspects of the gallium nitride growth chemistry is still under debate. The extent to which these pathways occur is a function of reactor geometry, operating conditions, and the degree of precursor mixing as determined by the design of gas delivery systems. Different types of reactor designs have been proposed in the literature, exist as commercial systems, or are in use in research laboratories, that range from complete precursor mixing to those where minimal precursor mixing occurs.

A transport-reaction model was developed for a planetary radial-flow GaN CVD reactor system to make the connection between reactor design and chemical kinetics as concrete as possible. It was clearly shown for the planetary radial-flow reactor, that the combination of reactor geometry and the minimal amount of precursor mixing promoted the TMG thermal decomposition pathway over the adduct

formation pathway for growth of gallium nitride. By pre-heating the organometallic precursor, the decomposition chemistry of TMG was initiated. Consequently, TMG was completely depleted before NH_3 comes into the picture, which in turn shut off the adduct formation route.

Moreover, a detailed deposition chemistry model was developed and applied to an industrial GaN MOVPE reactor showerhead system. A physically based model describing heat transfer and gas transport through the showerhead was previously developed and used in conjunction with this deposition model to study the interplay between the transport of reactants, adduct formation chemistry, and deposition kinetics within a MOVPE reactor showerhead system. The model predictions are in good agreement with experimental data with minimal parameter fitting with respect to the thermal model. No adjustable parameters were used in the kinetic model. Spatial distributions of deposition patterns predicted from the model are reproduced by experiments. Furthermore, quantitative validation of the model to showerhead weight experiments also demonstrates good agreement. This study has provided further insight into the physical and chemical mechanisms underlying gallium nitride epitaxial film growth

8.2 Application of Novel Geometrically Based Uniformity Criterion

A new approach to uniformity control was applied to a gallium nitride radial-flow chemical vapor deposition system with planetary wafer rotation. This approach

provides a process engineer with physical insight on what design parameter(s) should be adjusted to improve uniformity. The results showed that by modifying the susceptor temperature, uniform films of gallium nitride can be produced upon rotation in the planetary radial-flow reactor system.

A new approach for run-to-run uniformity control was applied to a SiC radial-flow chemical vapor deposition system with planetary wafer rotation. The results showed that by modifying the flowrate, uniform films of SiC can be produced upon rotation in the planetary radial-flow deposition system. Furthermore, one can envision applying this technique under a real-time run-to-run control setting, assuming the technology becomes available to obtain real-time, full wafer images of instantaneous deposition profiles.

Chapter 9

FUTURE WORK

9.1 Gallium Nitride Research

The Northrop Grumman Corporation has purchased a multiwafer state-of-the-art MOCVD reactor system for gallium nitride epitaxial growth. This reactor system has a completely different physical design than any of the reactors discussed in this dissertation. As a preliminary effort, I have developed a detailed 2D transport-reaction model for film thickness that takes into account complex gallium nitride reaction kinetics. The first task may involve comparing modeling and experimental measurements to further understand the interplay between reactor geometry and deposition kinetics. This may improve GaN reactor deposition uniformity, reduce run-to-run variability and increase reactor efficiency.

The second task is to investigate wafer edge effects within the system. One problem that is observed for this system is that the deposition significantly increases towards the wafer edge. Initial modeling taking into account several heat transfer terms shows that the wafer temperature is slightly higher at this location. Is this responsible for the increase in deposition seen experimental? Does this imply a reaction rate limited deposition rate? Answers to these questions may be possible through more detailed modeling of the heat transfer.

9.2 Silicon Carbide Research

The reactor system illustrated in Figure 7.1 can process 5 wafers in a single deposition run; to implement a run-to-run control algorithm based on minimizing the uniformity criterion, the reactor system would be operated with 4 of the 5 production wafers undergoing rotating and a single sacrificial stalled wafer. After each deposition run, the stalled wafer deposition profile would be measured and projected onto the β_n modes to obtain the NUPP and U_{CR} . The reactor deposition model then would be used to determine a search direction based on minimizing the uniformity criteria, and the reactor operating conditions would be adjusted accordingly.

In order to carry out this investigation, an accurate model of silicon carbide growth is needed. The model can be in the form of a physical model based on fundamental physics as discussed in this thesis or can be an empirical model based on growth rate data from various stalled wafer runs. Work is underway to develop an empirical model that will be used to minimize the uniformity criterion. One can also envision using both physical and empirical models to determine the optimal search direction.

In addition to film uniformity, the Northrop Grumman Corporation has an interest in achieving better nitrogen concentration uniformity across the wafer. This would require modifying the uniformity criterion to include both film uniformity and nitrogen concentration uniformity terms. Currently, a good understanding of the physics involved during nitrogen incorporation is absent. Thus, an empirical model

similar in form to SiC growth is needed.

We believe this additional work would further validate the "Nearest Uniformity Producing Profile" methodology and help the Northrop Grumman Corporation become the leader in SiC and GaN device electronic manufacturing.

BIBLIOGRAPHY

- [1] M. Behet, R. Hovel, A. Kohl, A. Mesquida, Kusters, B. Optiz, K. Heime, "MOVPE growth of III-V compounds for optoelectronic and electronic applications," *Microelectronics Journal* **27** (1996) 297.
- [2] Z.Z. Bandic, E.C. Piquette, P.M. Bridger, R.A. Beach, T.F. Kuech, T.C. McGill, "Nitride based high power devices: Design and fabrication issues," *Solid State Electronics* **42** (1998) 2289.
- [3] A.A. Burk Jr., M.J. O'Loughlin, R.R. Siergiej, A.K. Agarwal, S. Sriram, R.C. Clarke, M.F. MacMillan, V. Balakrishna, C.D. Brandt, "SiC and GaN wide bandgap semiconductor materials and devices," *Solid State Electronics* **43** (1999) 1459.
- [4] H.G. Henry, G. Augustine, G.C. DeSalvo, R.C. Brooks, R.R. Barron, J.D. Oliver, A.W. Morse, B.W. Veasel, P.M. Esker, R.C. Clarke, "S-band operation of SiC power MESFET with 20 W (4.4 W/mm) output power and 60% PAE," *IEEE Trans. Electronic Devices* **51** (2004) 839.
- [5] C. Theodoropoulos, T.J. Mountziaris, H.K. Moffat, J. Han, "Design of gas inlets for the growth of gallium nitride by metalorganic vapor phase epitaxy," *J. Cryst. Growth* **217** (2001) 65.
- [6] R.P. Pawlowski, C. Theodoropoulos, A.G. Salinger, T.J. Mountziaris, H.K. Moffat, J.N. Shadid, E.J. Thrush, "Fundamental models of the metalorganic vapor-phase epitaxy of gallium nitride and their use in reactor design," *J. Cryst. Growth* **221** (2000) 622.
- [7] S.A. Safvi, J.M. Redwing, M.A. Tischler, T.F. Kuech, "GaN growth by metalorganic vapor phase epitaxy. A comparison of modeling and experimental measurements," *J. Electrochem. Soc.* **144** (1997) 1789.
- [8] T.G. Mihopoulos, "Reaction and transport processes in OMCVD : selective and group III-nitride growth," Ph.D. Thesis, Chemical Engineering Department, Massachusetts Institute of Technology, (1999).
- [9] T.G. Mihopoulos, V. Gupta, K.F. Jensen, "Reaction-transport model for Al-GaN MOVPE growth," *J. Cryst. Growth* **195** (1998) 733.
- [10] C.H. Chen, H. Liu, D. Streigerwald, W. Imler, C.P. Kuo, M.G. Craford, "Parasitic reactions between alkyls and ammonia in OMVPE," *Mater. Res. Soc. Proc.* **395** (1996) 103.

- [11] O. Briot, S. Clur, R.L Aulombard, "Competitive adsorption effects in the metalorganic vapor phase epitaxy of GaN," *Apply. Phys. Lett.* **71** (1997) 1990.
- [12] J. Sun, J.M. Redwing, T.F. Kuech, "Transport and reaction behaviors of precursors during metalorganic vapor phase epitaxy of gallium nitride," *Phys. Stat. Sol. (a)* **176** (1999) 693.
- [13] J. Sun, J.M. Redwing, T.F. Kuech, "Model development of GaN MOVPE growth chemistry for reactor design," *J. Electronic Materials* **29** (2000) 2.
- [14] R.A., Adomaitis, "Identification of a deposition rate profile subspace corresponding to spatially-uniform films in planetary CVD reactors: a new criterion for uniformity control," *Computers and Chemical Engineering* **29** (2005) 829.
- [15] R.A., Adomaitis, "Objects for MWR," *Computers and Chemical Engineering* **26** (2002) 981.
- [16] H. Simka, B.G. Willis, I. Lengyel, and K.F. Jensen, "Computational chemistry predictions of reaction processes in organometallic vapor phase epitaxy," *Prog. Crystal Growth and Charact.* **35** (1998) 117.
- [17] D. Sengupta, "Does the ring compound $[(\text{CH}_3)_2\text{GaNH}_2]_3$ form during MOVPE of gallium nitride? Investigation via density functional and reaction rate theories," *J. Phys. Chem. B* **107** (2003) 291.
- [18] M.J. Almond, C.E. Jenkins, D.A. Rice, and K. Hagen, "Organometallic precursors to the formation of GaN by MOCVD: structural characterization of $\text{Me}_3\text{Ga}:\text{NH}_3$ by gas electron diffraction," *J. Organomet. Chem.* **439** (1992) 251.
- [19] D. Mazzaresse, A. Tripathi, W.C. Conner, K.A. Jones, L. Calderon, and W. Eckart, "In situ FTIR and surface analysis of the reaction of trimethylgallium and ammonia," *J. Electron. Mater.* **18** (1989) 369.
- [20] D.W. Kisker and T.F. Kuech, The principles and practice of organometallic vapor phase epitaxy in: D.T.J. Hurle (Ed.), *Handbook of Crystal Growth*, Vol. 3, Elsevier Science, Amsterdam, 1993 (Chapter 3).
- [21] A. Zaouk, E. Salvetat, J. Sakaya, F. Maury, and G. Constant, "Various chemical mechanisms for the crystal growth of IIIIV semiconductors using coordination compounds as starting material in the MOCVD process," *J. Cryst. Growth* **55** (1981) 135.

- [22] D.F. Davidson, K. Khose-Hoeinghaus, A.Y. Chang, and R.K. Hanson, "Pyrolysis mechanism for ammonia," *Int. J. Chem. Kinet.* **22** (1990) 513.
- [23] B. Beaumont, P. Gilbert, and J.P. Faurie, "Nitrogen precursors in metallorganic vapor phase epitaxy of (Al,Ga)N," *J. Cryst. Growth* **156** (1995) 140.
- [24] W.D. Monnery, K.A. Hawboldt, A.E. Pollock, and W.Y. Svrcek, "Ammonia pyrolysis and oxidation in the claus furnace," *Ind. Eng. Chem. Res.* **40** (2001) 144.
- [25] V.S. Ban, "Mass spectrometric studies of vapor-phase crystal growth of GaN," *J. Electrochem. Soc.* **119** (1972) 761.
- [26] S.S. Liu and D.A. Stevenson, "Growth kinetics and catalytic effects in the vapor phase epitaxy of gallium nitride," *J. Electrochem. Soc.* **125** (1978) 1161.
- [27] C.M. Chiang, S.M. Gates, A. Bensaoula, and J.A. Schultz, "Hydrogen desorption and ammonia adsorption on polycrystalline GaN surfaces," *Chem. Phys. Lett.* **246** (1995) 275.
- [28] J. Lui, D. Zhi, J.M. Redwing, M.A. Tischler, and T.F. Kuech, "GaN films studied by near-field scanning optical microscopy, atomic force microscopy and high resolution X-ray diffraction," *J. Cryst. Growth* **170** (1997) 357.
- [29] D.A. Neumayer and J.G. Ekerdt, "Growth of Group III Nitrides. A Review of Precursors and Techniques," *Chem. Mater.* **8** (1996) 9.
- [30] C. Blaauw, "Preparation and characterization of plasma-deposited silicon nitride," *J. Electrochem. Soc.* **131** (1984) 1114.
- [31] E.J. Cukauskas, W.L. Carter, and S.B. Qadri, "Superconducting and structure properties of niobium nitride prepared by rf magnetron sputtering," *J. Appl. Phys.* **57** (1985) 2538.
- [32] M.G. Jacko and S.J.W. Price, "The pyrolysis of trimethyl gallium," *Canadian Journal of Chemistry* **41** (1962) 1560.
- [33] S.P. DenBaars B.Y. Maa, P.D. Dapkus, A.D. Danner and H.C. Lee, "Homogeneous and heterogeneous thermal decomposition rates of trimethylgallium and arsine and their relevance to the growth of GaAs by MOCVD," *J. Cryst. Growth* **77** (1986) 188.

- [34] A. Thon and T.F. Kuech, "High temperature adduct formation of trimethylgallium and ammonia," *Appl. Phys. Lett* **69** (1996) 55.
- [35] C.A. Larsen, N.I. Buchan, S.H. Li, and G.B. Stringfellow, "Decomposition mechanisms of trimethylgallium," *J. Cryst. Growth* **102** (1990) 103.
- [36] M. Masi, H. Simka, K.F. Jensen, and T.F. Kuech, "Simulation of carbon doping of GaAs during MOVPE," *J. Cryst. Growth* **124** (1992) 483.
- [37] T.J. Mountziaris, S. Kalyanasundaram and N.K. Ingle, "Reaction-transport model of GaAs growth by metalorganic chemical vapor deposition using trimethyl-gallium and tertiary-butyl-arsine," *J. Cryst. Growth* **131** (1993) 283.
- [38] A. Hirako, M. Yoshitani, M. Nishibayashi, Y. Nishikawa, and K. Ohkawa, "GaN-MOVPE growth and its microscopic chemistry of gaseous phase by computational thermodynamic analysis," *J. Cryst. Growth* **237** (2002) 931.
- [39] J.B. Williams, *The Lewis acid-base concepts: an Overview*, Wiley, New York, 1980.
- [40] P.W. Atkins, *Physical Chemistry 7th Ed.*, W.H. Freeman, New York, 2002.
- [41] R.C. Reid, J.M. Prausnitz, and B.E. Poling, *The Properties of Gas and Liquid*, McGraw Hill, New York, 1987.
- [42] R.M. Watwe, J.A. Dumesic, and T.F. Kuech, "Gas-phase chemistry of metalorganic and nitrogen-bearing compounds," *J. Cryst. Growth* **221** (2000) 751.
- [43] A. Tachibana, O. Makino, S. Tanimura, H. Tokunaga, N. Akutsu, and K. Matsumoto, "Quantum chemical studies of gas phase reactions between TMA, TMG, TMI and NH₃," *Phys. Stat. Sol. (a)* **176** (1999) 699.
- [44] A. Pelekh and R.W. Carr, "Gas-phase reaction of trimethylgallium and ammonia: Experimental determination of the equilibrium constant and ab initio calculations," *J. Phys. Chem A* **105** (2001) 4697.
- [45] A. Leib, M.T. Emerson, and J.P. Oliver, "Prediction of stabilities of trialkylgallium addition compounds," *Inorg. Chem.* **4** (1965) 1825.
- [46] B.S. Sywe, J.R. Schlup, and J.H. Edgar, "Fourier transform infrared spectroscopic study of predeposition reactions in metallorganic chemical vapor deposition of gallium nitride," *Chem. Mater.* **3** (1991) 737.

- [47] M.J. Almond, M.G.B. Drew, C.E. Jenkins, and D.A. Rice, "Organometallic precursors for the formation of GaN by metal-organic chemical vapor deposition: A study of $[(\text{CH}_3)_2\text{GaNH}_2]_3$," *J. Chem. Soc. Dalton. Trans.* (1992) 5.
- [48] G.E. Coates, "Trimethylgallium. Part I. The relative stabilities of its coordination compounds with the methyl derivatives of groups VB and VIB, and the thermal decomposition of some trimethylgallium-amine complexes," *J. Chem. Soc.* (1951) 2003.
- [49] U. Bergmann, V. Reimer, and B. Atakan, "An experimental study of the reactions of trimethylgallium with ammonia and water over a wide temperature range," *Phys. Chem. Chem. Phys* **1** (1999) 5593.
- [50] D.B. Hash, T. Mihopoulos, T. R. Govindan, and M. Meyyappan, "Characterization of showerhead performance at low pressure," *J. Vac. Sci. Technol. B* **18** (2000) 2808.
- [51] B.D. Hoffman, R. A. Adomaitis, M. E. Aumer, D. Thomson, and D. Parlow, "Simulator development and validation for optimized GaN MOVPE reactor showerhead design," *revisions submitted to IEEE* (2006).
- [52] A. Acrivos, B. D. Babcock, and R. L. Pigford, "Flow distributions in manifolds," *Chem. Engng Sci.* **10** (1959) 112.
- [53] The Mathworks, Inc., (<http://www.mathworks.com>).
- [54] P.M. Frijlink, "New versatile, large size MOVPE reactor," *J. Crystal Growth* **93** (1988) 207.
- [55] R. Beccard, D. Schmitz, E.G. Woelk, G. Strauch, Y. Makarov, M. Heuken, M. Deschler, and H. Juergensen, "High temperature CVD systems to grow GaN or SiC based structures," *J. Mat. Sci. and Eng.* **B61-62** (1999) 314.
- [56] O. Danielsson, A. Henry, and E. Janzen, "Growth rate predictions of chemical vapor deposited silicon carbide epitaxial layers," *J. Cryst. Growth* **243** (2002) 170.
- [57] W. Ji, P.M. Lofgren, C. Hallin, C.Y. Gu, and G.Zhou, "Computational modeling of SiC epitaxial growth in a hot wall reactor," *J. Cryst. Growth* **220** (2000) 560.
- [58] A.N. Vorob'ev, S.Yu. Karpov, M.V. Bogdanov, A.E. Komissarov, O.V. Bord, A.I. Zhmakin, and Yu.N. Markarov, "Numerical study of SiC CVD in a vertical cold-wall reactor," *Computational Materials Science* **24** (2002) 520.